ION IMPLANTATION DAMAGE IN CdS USING TEM AND RBS/CHANNELING

BY

© NALIN RASIKLAL PARIKH

A Thesis

Submitted to the School of Graduate Studies

in Partial Fulfilment of the Requiremens

for the Degree

Doctor of Philosophy

McMaster University

July 1985

ION IMPLANTATION DAMAGE IN CdS USING TEM AND RBS/CHANNELING

DOCTOR OF PHILOSOPHY (1985) McMASTER UNIVERSITY

Metallurgy and Materials Science Hamilton, Ontario.

TITLE: ION IMPLANTATION DAMAGE IN CdS USING TEM AND RBS/CHANNELING

AUTHOR: Nalin Rasiklal Parikh, B.Sc. (Gujarat University, India)

M.Sc. (Gujarat University, India)

M.Eng. (McMaster University)

SUPERVISOR: Dr. D.A. Thompson

NUMBER OF PAGES: XVIII, 192

ABSTRACT

Lattice disorder produced by heavy ion implantation of cadmium sulphide crystals at 50 K and 300 K has been investigated using Transmission Electron Microscopy (TEM) and Rutherford Backscattering (RBS)/-Channeling techniques.

TEM observations of Bi^+, Ar^+ and Ne^+ implanted samples showed that two types of dislocation loops were produced, type I with a Burgers vector $\bar{b} = 1/2 \langle 0001 \rangle$ and type II with a Burgers vector $\bar{b} = 1/3 \langle 11\bar{2}0 \rangle$. Type II loops were nearly twice as large in size and two to three times greater in number density than type I loops. The large loops of type II were predominantly vacancy loops. Both types of loops lie predominantly in the $\{1\bar{1}00\}$ and $\{11\bar{2}0\}$ prism planes. The loop size and number density increased with increasing energy deposited into elastic collisions. For increasing ion dose the loop size increased while the number density decreased.

In-situ measurements of the lattice disorder have been made using the RBS/channeling technique with 0.6 MeV to 2.8 MeV He^+ channeled along the a- and c-axes of the CdS crystals. The amount of disorder was measured in terms of the areal density of cadmium scattering centers (N_D), and the minimum dechanneling yield (χ_{min}). Measured N_D values were found to be two orders of magnitude lower than theoretical predic-

tion and the χ_{min} values were about an order of magnitude higher than those calculated assuming randomly displaced scattering centers. The disorder was greater measured along the c-axis than along the a-axis. It was also greater at 300 K than at 50 K. These observations suggest that the lattice distortion is greater in the direction perpendicular to the c-axis. It was also found that N_D increased with increasing E_o, while χ_{min} values were energy independent over the energy range investigated. These results and the rapid increase in N_D values observed when the crystal is tilted slightly away from the channeling direction ('Off-Axis' measurements) are consistent with the presence of dislocation loops as observed by the TEM.

ACKNOWLEDGEMENTS

I wish to thank my supervisor, Dr. D.A. Thompson, for his continuous support and guidance during the course of this research. I also wish to thank Dr. J.A. Davies for his constructive criticisms and for the many productive discussions. There were many scientists who contributed a great deal towards this work, among them Dr. R. Burkova, Dr. V.S. Raghunathan and Dr. G.J.C. Carpenter. I greatly appreciate their enthusiasm and encouragement.

I also would like to thank Dr. G.R. Piercy, Dr. G. Singh, Dr. Kirkaldy, and Dr. G.R. Purdy for the helpful discussions. To my colleague Doris Stevanovic a special thanks for her superb help in editing and proof-reading the many drafts of this thesis and also for helping to keep the experimental facilities running smoothly. My apologies, to my other colleagues, in particular Rick Macaulay-Newcombe, Ahmed Ibrahim and Usman Akano for continuing my experiments into their scheduled experimental time without their prior permission and I would also like to thank them for their helpful discussions. My many thanks to the Tandem Laboratory staff, in particular Mr. J. Stark, Mr. W. Williams, Mr. A. Woolvett and Mrs. S. Wannamaker for their help during my stay at McMaster.

I am indebted to the Canadian International Development Agency and Brazilian Ministry of Industry and Commerce for supporting my study at McMaster.

Finally, I would like to thank my wife, Anju, for her patience and excellent support throughout this work and also for sharing the burden of typing this thesis.

TABLE OF CONTENTS

Figure captions

Table captions

CHAPTER 1

INTRODUCTION

The technological importance of elemental semiconductors has long been established. Currently, compound semiconductors, particularly II-VI and III-V compounds, are becoming increasingly important because of their electronic properties.

Cadmium sulphide is a direct band-gap (2.42 eV), II-VI compound semiconductor [Neuberger (1969)]. This material is suitable for the fabrication of p-n junction electro-optic devices such as light emitting diodes (LED) and solar cells. CdS is normally either n-type or insulating and attempts to convert it to p-type by conventional diffusion techniques have failed. This failure is ascribed to its tendency toward self-compensation [Mandel (1964), Kroger (1965)] resulting from surface dissociation at temperatures required for the diffusion of dopants. Therefore, ion implantation which can be used to dope semiconductors at low temperatures offers a promising alternative. In addition, ion implantation provides precise control of the total amount and concentration profile of the implanted dopants. However, a serious disadvantage of this technique is the accompanying lattice disorder which results as the energetic ion dissipates its kinetic

energy upon penetrating the target.

This thesis is concerned with the characterization of the lattice damage produced in CdS crystals due to implantation with various ions. Two independent analysis techniques were employed; namely, Transmission Electron Microscopy (TEM) and Rutherford Backscattering (RBS)/Channeling. Attempts will be made to correlate the RBS/channeling results with the defect structures observed in the electron microscope.

In chapter 2, the crystal structure and physical properties of CdS are presented, followed by a review of previous studies of ion implantation effects in single crystals. This is followed in chapter 3 by a brief theoretical background on atomic collisions in solids along with the nature of defects produced by ion implantation in metals and semiconductors.

The damage analysis techniques used in the present study are discussed in chapter 4. This discussion is divided into two sections: the operation of the transmission electron microscope along with the theories of image contrast and characterization of defects relevant to this study, and the theoretical aspects of the RBS/channeling technique and the methods of damage determination. The accelerator facilities for RBS/channeling analysis and ion implantation are described in chapter 5. Sample preparation procedures and alignment of the single crystals for channeling studies are discussed. Important experimental parameters are also presented.

In chapter 6, the experimental results of implantation damage characterized by TEM and RBS/channeling are presented. This chapter is divided into three sections: TEM observations of lattice disorder and characterization of the defects produced; the damage as measured using the RBS/channeling technique; and finally a correlation of the results obtained by both techniques.

A summary of conclusions relating to the implantation damage produced in CdS is reported in chapter 7.

CHAPTER 2

LITERATURE SURVEY

In this chapter an introduction to the crystal structure and properties of CdS are presented, followed by a review of previous studies of ion implantation in CdS.

2.1 Crystal Structure, Atomic Bonding and Properties of CdS

CdS normally crystallizes in the hexagonal wurtzite structure. Fig. 2.1 shows a schematic of the atomic arrangement of Cd and S atoms in the wurtzite structure with the major planes and axes labelled in Miller indices. The hexagonal structure is defined in terms of the lattice parameters a and c, which are reported [Devlin (1960)] to be 0.4137 nm and 0.6716 nm respectively. There are two molecules in the hexagonal unit cell with two Cd atoms at 0,0,0; $a_1/3$, $2a_2/3$, $c/2$ and two S atoms at 0,0,u; $a_1/3, 2a_2/3, (c+u)/2$ where $u = 3c/8$ and a_1 and a_2 are unit vectors along the a_1 and a_2 directions of the crystal as shown in Fig. 2.1(b). Each Cd atom is bonded to four S atoms, approximately at the corners of a tetrahedron. The wurtzite structure does not have a center of symmetry and there is a polar axis parallel to [0001]. Consequently wurtzite crystals are piezoelectric and also pyroelectric [Azaroff and Brophy (1963)]. CdS like other II-VI compounds has partly

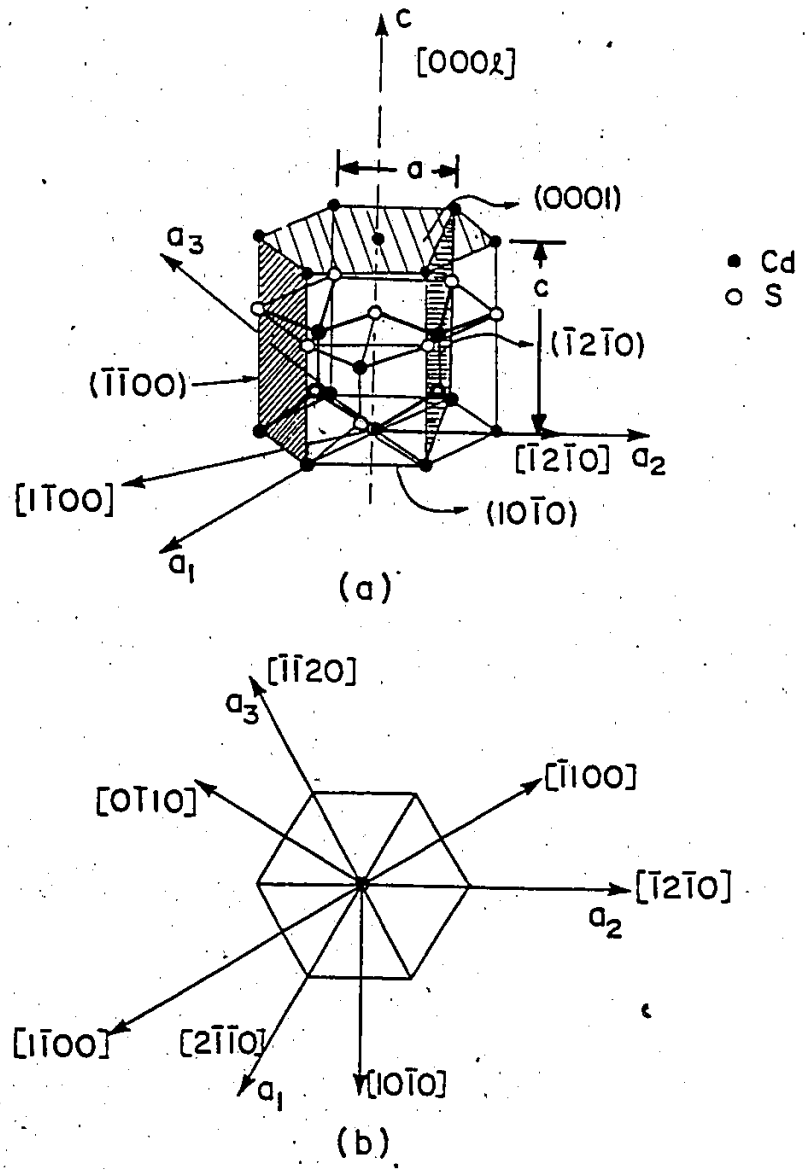

Fig. 2.1 a) The structure of a CdS crystal (wurtzite) showing indices of planes and directions; b) basal plane projection

covalent and partly ionic bonding which arises as follows. A cadmium atom has $5s^2$ electrons while a sulphur atom has $3s^2 3p^4$ bonding electrons in its outer shell because of its high ionization potential. Cadmium shares its two electrons with sulphur. However, sulphur has a higher electronegativity compared to cadmium hence the $5s^2$ electron cloud of cadmium is shifted toward the sulphur atom giving rise to ionic nature of bonding. A more detailed study of atomic bonding in II-VI compounds is given by Neuberger [1969].

The type of conductivity, whether electron (n-type) or hole (p-type) of II-VI compound materials, is in general, associated with the departure from stoichiometry as opposed to III-V group materials in which the conductivity is controlled by the type of impurity present. CdS as grown always exhibits n-type conductivity which is associated with a sulphur vacancy arising from a sulphur deficiency in the compound. If such crystals are annealed in a sulphur atmosphere or if the crystals are grown in an excess sulphur vapour pressure, then the resulting crystals will be insulating.

2.2 Ion Implantation in CdS

Early attempts to form a p-n junction in CdS by ion implantation were reported by Anderson et al. [1968], Chernow et al. [1968], Pollard and Hartke [1969], Hou and Marley [1970] and Shiraki et al. [1972]. Anderson et al. [1968], Hou and Marley [1970] investigated phosphorous implantation at energies of 50 keV, 0.3, 0.5, and 1.0 MeV at 300 K for a

total dose of $1x10^{15}$ ions.cm^{-2}. The authors succeeded in converting the implanted layer to p-type after annealing at around 720 K. Pollard and Hartke implanted 400 keV arsenic and phosphorus ($5x10^{14}$ ions.cm^{-2}) at 670-770 K. They also succeeded in forming a p-type layer. Chernow et al. implanted high doses of 25 keV Bi^+ (up to $1.6x10^{16}$ ions.cm^{-2}) and formed a p-type layer without any annealing treatment. Shiraki et al. [1972] formed p-type layers by implantation with 200 keV nitrogen ions for doses of 10^{15} ions.cm^{-2} to 10^{17} ions.cm^{-2} at room temperature. These samples were coated with 200 nm of SiO_2 for subsequent annealing in a controlled inert gas atmosphere at 670 K. The same authors characterized the p-n junction produced using I-V and C-V measurements. In further work the same authors [Shiraki et al. 1973] investigated electroluminescent and photoluminescent properties and found red luminescent bands at 725 nm and 900nm. The same red bands were observed in neon implanted specimen suggested that lattice defects present in the CdS are responsible for the observed behaviour and not the implanted species. Electron Paramagnetic Resonance (EPR) investigation by the same authors confirmed the existence of sulphur and cadmium vacancy clusters. Other investigations of the various emission properties of ion-implanted CdS and other II-VI compounds have been reported by Gibbons et al. (1965), Tell et al. (1970), Barnes et al. (1972), Norris (1973), Walsh (1977), and Bryant et al. (1973, 1982).

2.3. Ion Implantation Damage Studies of CdS Crystals

As seen above the properties of implanted materials are

strongly dependent upon both the chemical nature of the implanted ions and the lattice defects produced by these ions. Therefore, it is important to determine the type and concentration of the defects produced.

Ion implantation damage can be investigated by various techniques. These techniques may be broadly divided into two groups, direct or indirect. Techniques such as transmission electron microscopy (TEM), Rutherford backscattering/channeling are generally direct techniques allowing a quantitative measure of the defect concentrations to be obtained. Indirect techniques involve studying physical properties such as resistivity, luminescence, mechanical hardness, EPR etc. by which the defect level is obtained from the change in the measured parameter.

In the present study, RBS/channeling and TEM were selected to study implantation damage in CdS because of the direct and quantitative assessment offered by these techniques. Studies of ion implantation damage in CdS using the RBS/channeling technique have been carried out by Armitage [1970], Williams et al. [1971], Miller et al. [1972], Hutchby et al. [1972], Grigor'ev et al. [1974, 1985] and Baxter [1977]. The general conclusion of these studies was that the implantation damage increases to saturation with implantation dose and that heavier ion damage showed a tendency to saturate at lower doses for increasing ion mass and decreasing ion energy. The dose required for damage saturation is two orders of magnitude greater than the dose required to amorphize

elemental and III-V group semiconductors [Walker et al. 1978]. The saturation damage did not result in amorphization as in Si, Ge and III-V semiconductors except in the case of 40 keV fluorine ($1x10^{17}$ ions.cm^{-2}) and chlorine ($8x10^{16}$ ions. cm^{-2}) implants [Hutchby et al. (1972)]. These implant doses of Cl and F are very high which may have formed a chemical compound with host atoms.

Lattice disorder in ion implanted CdS has been investigated by Williams et al. [1971], Olley et al. [1970] and Govind et al. [1971] using the TEM technique. Williams et al. studied lattice disorder in CdS produced by 100 keV zinc implantation for low doses ($5x10^{13}$ ions. cm^{-2}) and found that small vacancy or interstitial clusters of 1 to 3 nm in diameter were formed. On annealing at ≈ 670 K, these clusters rearranged to form small dislocation loops. Govind et al. analysed samples implanted with 25 keV bismuth and observed "black-spots" of ≈ 10 nm in diameter. However, the nature of the "black-spots" was not determined.

Yoshiie et al. [1980, 1981, 1983] have studied electron damage of II-VI compounds in a high voltage electron microscope. The authors observed dislocation loops in CdS crystals after electron irradiation at energies >300 keV, at temperatures below ≈ 670 K. It was concluded that these loops were of interstitial type, either with the Burgers vector $\vec{b}$ = 1/3 $\langle 2\bar{1}\bar{1}0 \rangle$ on $\{\bar{1}2\bar{1}0\}$ planes, or with $\vec{b}$ = 1/2 [0001] on the (0001) plane.

Most of the previous investigations of lattice disorder in cadmium sulphide were concerned with quantifying the damage using RBS/channeling, TEM, and optical emission properties. In this study, a detailed evaluation of the lattice disorder in CdS implanted with various ions, Ne^+, Ar^+, Kr^+, and Bi^+ is undertaken, with analysis being carried out using both TEM and RBS/channeling. The nature and quantity of the defects are established and the interaction of channeled ions with the defects is discussed.

CHAPTER 3

THEORY

3.1 ATOMIC COLLISIONS IN SOLIDS

3.1.1 Introduction

In this section, the theoretical aspects of atomic collisions in solids and the resulting lattice disorder are described.

When an energetic ion strikes a target, it generates several recoiling atoms by a series of elastic collisions. It also loses energy by interacting with the target electrons (inelastic collisions). If the recoil atom is sufficiently energetic to be permanently displaced from its lattice site i.e. energy received > E_d (the threshold displacement energy), at least one interstitial-vacancy pair is formed. In many cases, the primary recoil will be energetic enough to distribute its energy in a cascade of atomic collisions (collision cascade), ejecting secondary atoms from their lattice sites. The following discussion of atomic collisions in solids shall be restricted to ion energies typical to the ion implantation process, i.e. energies from a few keV to several hundred keV. In this energy regime the collision between an incident ion and atoms of a target is simplified by the following assumptions:

i) The collision is binary, i.e. the incident keV ion interacts with one stationary lattice atom at a time, hence the mean free path (m.f.p.) between collisions is very much greater than the mean interatomic distance.

ii) The energy losses due to elastic and inelastic interactions are independent.

iii) The collision can be described classically and non-relativistically [Mott and Massey (1965)]. This is valid for particles with wavelength, λ such that,

$$\lambda = h\,(2\,M_1 E)^{-1/2} \gg p \qquad (3.1)$$

where h is Planck's constant

M_1 and E are atomic mass and energy of the incident ion respectively

p is the distance of closest approach or the impact parameter.

Fig. 3.1 illustrates a typical two body scattering process between an ion and a target atom in both the laboratory coordinate system (lab. c.s.) and the center of mass co-ordinate system (c.m.c.s). In the c.m.c.s., the incident ion is elastically deflected through an angle Θ_c, transferring kinetic energy T to the struck atom. The scattering angle θ and the recoiling atom energy, T, are given by [Goldstein (1958)] as

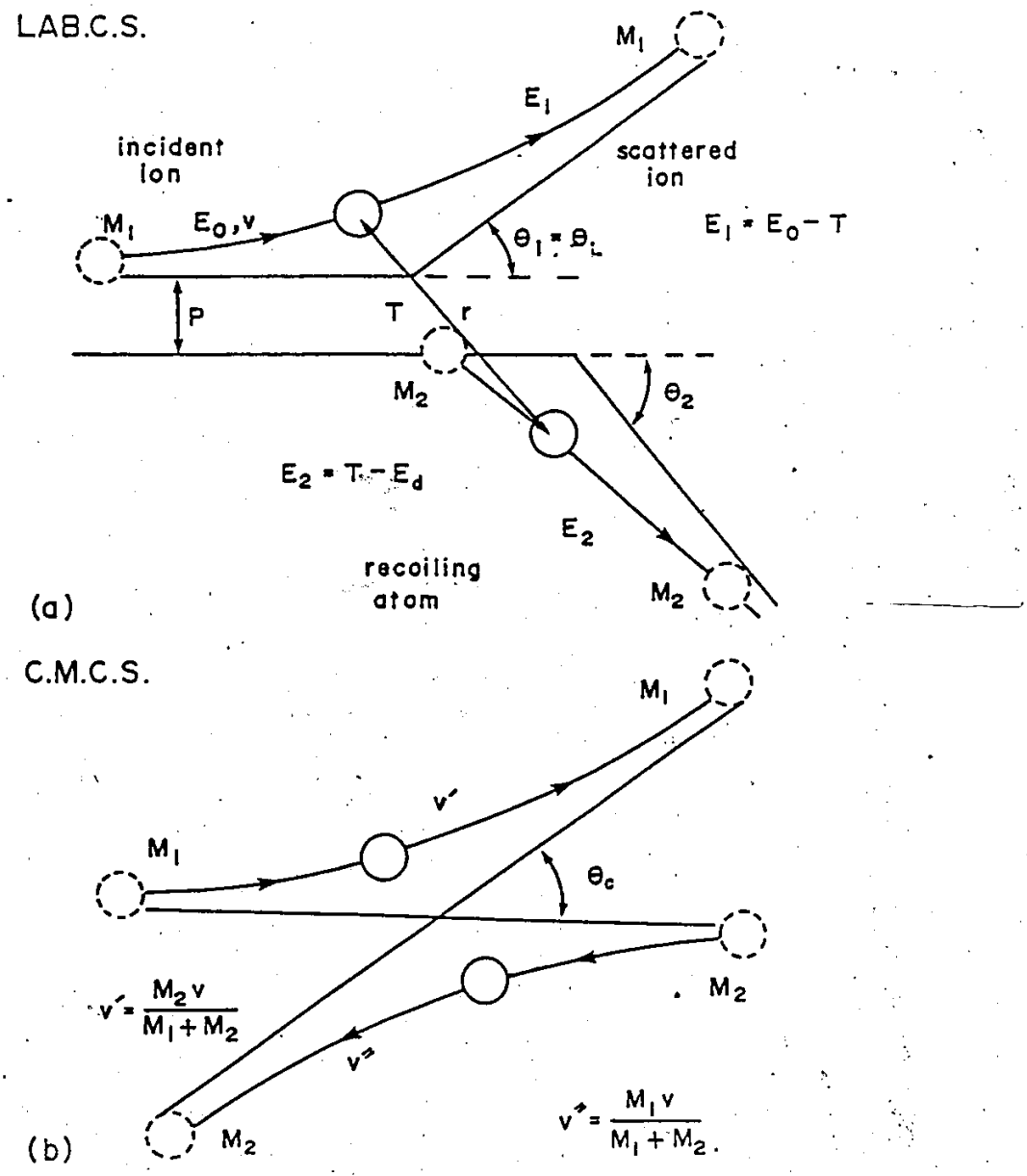

Fig. 3.1 a) A binary collision in the Laboratory Coordinate System

b) A binary collision in the Center of Mass Coordinate System

$$\Theta_c = \pi - 2p \int_0^{u_o} \frac{du}{\left[1 - v(u)/E' - p^2u^2\right]^{1/2}} \qquad (3.2)$$

where $E' = M_2E/(M_1+M_2)$

$u = 1/r$ where r the distance between the colliding atoms

$u_o = 1/p$

$V(u)$ is the interaction potential

M_2 is atomic mass of target atom;

and $$T = T_m \sin^2(\theta/2) \qquad (3.3)$$

where $T_m = \gamma E = 4M_1M_2E/(M_1 + M_2)^2$.

For head on collisions $T = T_m$, and the maximum energy transfer to the recoiling atom will occur.

3.1.2. The Interatomic Potential

The type of interatomic potential depends very much upon the distance of closest approach between the ion and target atom. The general form of the interatomic potential is shown in Fig. 3.2. It is attractive at large distances and strongly repulsive at short distances. The intermediate region corresponds to the equilibrium interatomic

separation, d. The attractive part of the potential arises, almost entirely from Coulombic forces for ionic solids, while for covalent solids it is a result of the electron exchange interaction. In the repulsive regime, the potential is due to electrostatic repulsion of the positively charged nuclei screened by their surrounding electrons.

The magnitude of the repulsion depends on the ability of the orbital electrons to screen the nuclear charge. For very close approach, the screening effect is neglected and the interaction is simply Coulombic of the form:

$$V(r) = Z_1 Z_2 e^2 / r \qquad (3.4)$$

where Z_1 and Z_2 are atomic numbers of incident ion and the target atom respectively

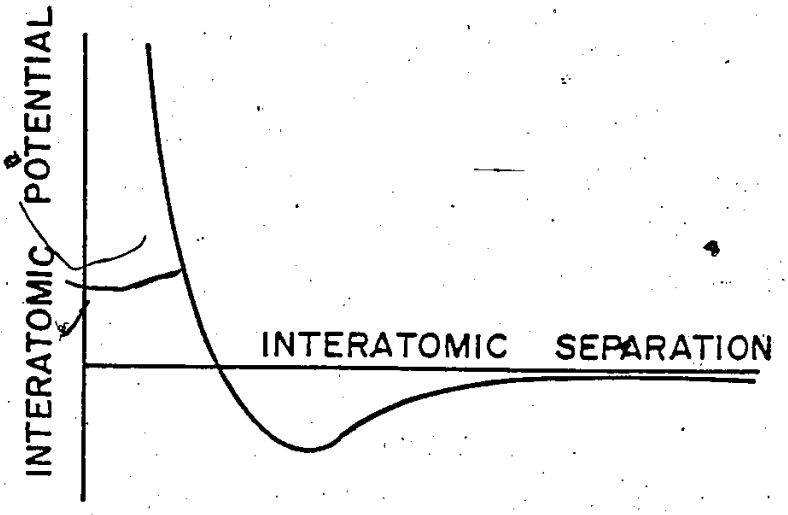

Fig. 3.2 General form of the interatomic potential in terms of interatomic distance

For keV ion-atom scattering, a wide range of impact parameters is possible. Therefore, a number of approximate potentials, to treat each particular range for r, were proposed.

i) For $r \leq d$, the Born-Mayer [1922] potential is relatively successful;

$$V(r) = A \exp(-r/B), \qquad (3.5)$$

where A & B are constants derivable from the elastic moduli.

This potential is, however, too weak for small values of r.

ii) For $r \ll d$, the screened potential due to Bohr [1948], is more appropriate,

$$V(r) = [Z_1 Z_2 e^2/r] \exp(-r/a) \qquad (3.6)$$

where a is the Thomas-Fermi screening distance given by Lindhard et al. (1968)

$$a = a_o(Z_1^{2/3} + Z_2^{2/3})^{-1/2}, \qquad (3.7)$$

where $a_o = \hbar^2/me^2$ is the Bohr radius,

iii) The interatomic potential for the intermediate region of separation which is appropriate to the ion implantation work is obtained from the Thomas-Fermi statistical model of the atom and is given by:

$$V(r) = \{Z_1 Z_2 e^2/r\} \quad \phi_{TF}(Z_1, Z_2, r, a) \qquad (3.8)$$

ϕ_{TF} is called the Thomas-Fermi screening function which has been calculated numerically [Firsov (1958)] and tabulated by Gombas (1956). ϕ_{TF} tends to unity as $r \to 0$ (Coulombic scattering), and to zero as $r \to \infty$. Lindhard [1965] has proposed a simplified form for the Thomas-Fermi screening, function which is given as

$$\phi_{T.F.}(r/a) \simeq \frac{r/a}{[(r/a)^2 + C^2]^{1/2}} \qquad (3.9)$$

where C is an adjustable parameter

A relationship between these various potential functions as calculated by Gibson et al. (1960) for two copper atoms, as a function of their separation, is shown in Fig. 3.3. It is seen from the figure that the Bohr potential drops much faster than the Born-Mayer potential as r increases. It becomes zero at a distance of = 0.3 units of the lattice constant, while the Born-Mayer potential has a some finite value at very small values of r. A more detailed treatment of interatomic potentials is dealt with by Torrens [1972] and by Carter and Colligan [1968].

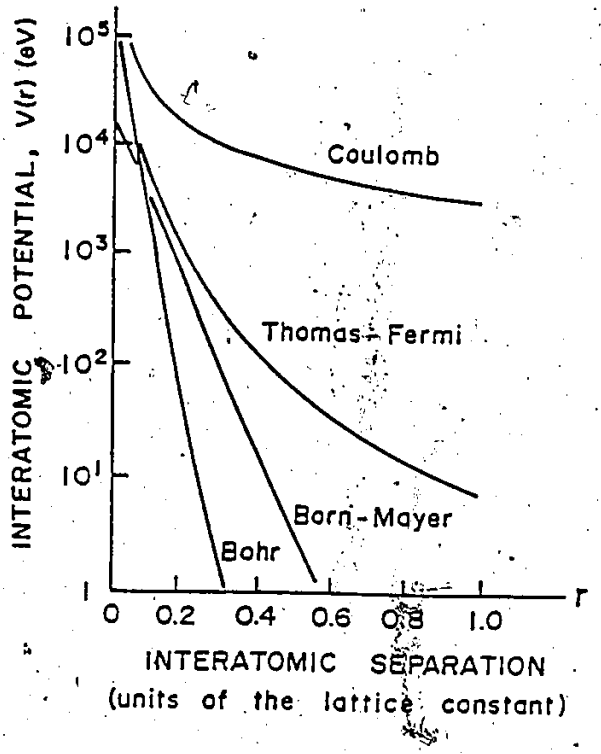

Fig. 3.3 Various proposed interatomic potentials between two copper atoms

3.1.3. Energy Loss Processes

There are two major energy loss processes that an incident ion undergoes when penetrating through a target material. One is referred to as nuclear energy loss, in which elastic interactions occur between the incident ion and the screened nuclear charge of the target atoms. The other energy loss process is referred to as electronic energy loss, in which an interaction take place between the incident ion and the

target electrons. Although the two energy loss processes are correlated, Lindhard [1954] has suggested that they can be treated separately. Hence, the total energy loss per unit length, $-dE/dx$, where x is the distance measured along the direction of incidence of the ion, is given by the sum of the nuclear and electronic energy losses, i.e.,

$$dE/dx = (dE/dx)_n + (dE/dx)_e \qquad (3.10)$$

where $(dE/dx)_n$ is the nuclear energy loss and,
$(dE/dx)_e$ is the electronic energy loss.

Hence, the total incident energy, E, can be written as the sum of the total nuclear energy deposited, $\nu(E)$, and the total electronic energy deposited, $\eta(E)$, i.e.,

$$E = \nu(E) + \eta(E) \qquad (3.11)$$

Lindhard, Scharff and Schiøtt (L.S.S.) [1968] have developed a comprehensive unified theory for atomic stopping in terms of a dimensionless energy ε, where

$$\varepsilon = aM_2E/Z_1Z_2e^2(M_1 + M_2) \qquad (3.12)$$

which leads to an universal nuclear stopping curve as shown in Fig. 3.4. Since electronic stopping is a function of the velocity of the incident ion, a universal curve does not exist.

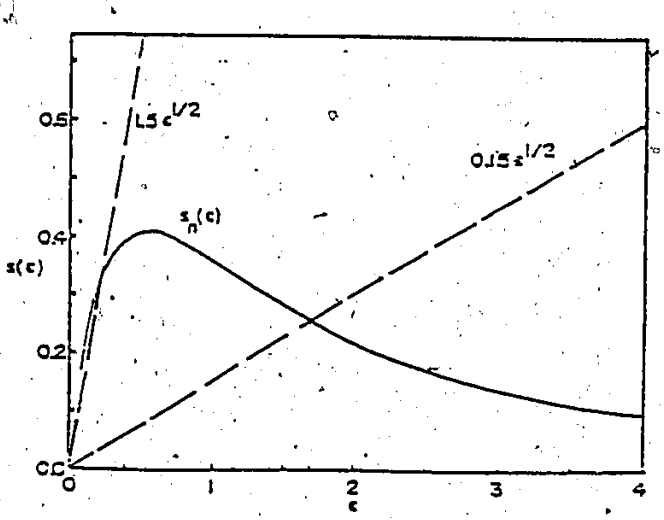

Fig. 3.4 Nuclear and electronic stopping powers in terms of the dimensionless energy parameter ε. Electronic stopping power is given for k = 0.15 and 1.5 (dashed line).

As the ion penetrates the target it continues to lose energy until it comes to rest. Assuming a random array of atoms in the solid and the statistically random nature of the collisions, different ions will have a different number and sequence of collision events before they come to rest. Hence, there will be a distribution of stopping distances (ranges) which is usually assumed to have a Gaussian shape. This has lead to the definition of mean ion range $\bar{R}$, the projection of this range into the incident direction is called the projected range $\bar{R}_p$ and their standard deviations are known as the straggling ΔR and ΔR_p.

3.1.4. Number of Displaced Atoms and Damage Distribution of Defects

In ion implantation studies, in addition to the location and range distributation of the implanted atoms, one would generally like to determine the following:

i) the concentration of defects produced,

ii) the spatial distribution of the these defects,

iii) the type of defects produced.

Collision theory can give information on items (i) and (ii) while item (iii) is difficult to predict theoretically since the final stable defect configuration depends upon a number of factors such as crystal structure, the mobility of the defects at the implantation temperature, the interaction of the defects with impurities and other crystal defects etc. The spatial distribution of defects is given in terms of the spatial distribution of the incident ion energy dissipated in elastic collisions, since inelastic collisions do not in general contribute to atomic displacements. The spatial distribution of the range and energy deposited in atomic collisions is described by an integrodifferential equation given by Lindhard et al. [1963] for $Z_1 = Z_2$:

$$F(\bar{r}, E) = N\delta r \int d\sigma_{n,e} \left[F(\bar{r}-\delta\bar{r}, E- T_n- \sum_i T_{ei}) + F(\bar{r}-\delta\bar{r}, T_n- U) + \sum_i F_e(\bar{r}- \delta\bar{r}, T_{ei}-U_i)\right] + (1- N\delta r \int d\sigma_{n,e})\, F(\bar{r}- \delta\bar{r}, E) \tag{3.14}$$

where $F(\bar{r},E)$ is a spatial distribution function for a particle at position $\bar{r}$

$N\delta r d\sigma_{n,e}$ is the probability that the particular collision occurs in δr,

T_n is the energy transferred to the recoiling atom,

T_{ei} is the energy transferred to the i^{th} electron,

E_d is the displacement energy for the target atom,

U_i is the ionization energy of the i^{th} electron, and

F_e is the spatial distribution function for the electrons.

This equation is a linear Boltzmann transport equation for which assumptions considered in Sec. 3.1.2 are valid. An exact solution of the above equation is impossible unless further simplifying approximations are made. It is therefore necessary to find the spatial distribution moments and reconstruct the distribution from them. To determine the moments of the deposited energy distribution both sides of equation (3.14) are multiplied by r^n, and then integrated by parts. This results in a recursive expression for each spatial moment [Winterbon et al. (1970)] defined as

$$\langle r^n \rangle = \int r^n F(\bar{r},E) d^3r. \qquad (3.14)$$

The Edgeworth expansion, a weighted Gaussian distribution is commonly used for ion deposited energy and ion range distributions, because of its simplicity, and because ion energy and range distributions are often close to being Gaussian in shape. For ions incident normal to the target surface, the longitudinal distribution expressed in

terms of an Edgeworth expansion, would be:

$$F(z,E) = (\tilde{g}/\sqrt{(2\pi\mu_2)})\ \exp(-\zeta^2/2)\ f(\zeta) \qquad (3.15)$$

where $f(\zeta) = 1 + \frac{\mu_3}{6\mu_2^{3/2}}(3\zeta - \zeta^3) + \frac{1}{24}\left(\frac{\mu_4}{\mu_2^2} - 3\right).(3 - 6\zeta^2 + \zeta^4)$

$$-\left(\frac{\mu_3^2}{72\ \mu_2^3}\right).(15 - 45\zeta^2 + 15\zeta^4 - \zeta^6)\ , \quad \text{and}$$

$$\zeta = \frac{z - \langle z\rangle}{\mu_2^{1/2}},$$

where $\mu_n = \langle (z - \langle z\rangle)^n \rangle$

$\tilde{g} = 1$ for the range distribution of the ions

$= \nu(E)$ for the damage distribution

$= n(E)$ for the ionization.

Two important parameters for damage determination are the first two moments of the spatial distrbution of energy deposited into nuclear collisions; the mean damage depth R_p^D, and the damage straggling or standard deviation of the damage distribution, ΔR_p^D.

A simple model to determine the number of displaced atoms which results from a collision cascade was proposed by Kinchin and Pease [1955]. This model treats the collision as a two body event and assumes that the struck atom will be displaced permanently only when it receives an energy greater than or equal to E_d. According to this model the

number of displaced atoms, N_{KP}, is

$$N_{KP} = E/2E_d \,. \qquad (3.16)$$

This model has been modified by Sigmund [1969] using a power law approximation to the Thomas-Fermi screened Coulomb potential and corrected to account for replacement collisions and for energy deposited in electronic processes, both of which result in a reduction in the number of displaced atoms. The modified Kinchin- Pease formula for the number of displaced atoms is given by,

$$N_D = 0.42\ \nu(E)/E_d. \qquad (3.17)$$

This equation states that N_D varies linearly with the elastically deposited energy. This linear relation breaks down as the energetic incident ion mass and the target mass increase, since a region of higher density of recoil atoms is created. At some point, the mean free path between collisions becomes comparable to the mean interatomic distance and hence the basic assumption of binary collisions cannot be applied. Brinkman [1955] proposed that when such a condition arises, an energetic ion creates a violently disturbed region cosisting of a vacancy rich central core surrounded by a high density of interstitials. Depending upon the ion energy, ion mass and the target atomic mass the disturbed region may encompass a volume approximately equivalent to the entire collision cascade or may occupy some localized volume (sub-cascade). Since all of the atoms in the cascade volume become displaced

from their lattice site, the region is referred to as a displacement spike. Heavy ions with energies in the range of ≈ 10 to 60 keV would typically produce a displacement spike [Thompson (1981)].

When the energy of the moving ion drops below a certain value where it cannot create new displacements, the energy of the ion is dissipated by thermal vibrations to the surrounding lattice, therby raising the temperature of the lattice. This type of energy dissipation forms what is called a thermal spike. A comprehensive analysis of thermal spikes is given by Seitz and Koehler [1956]. A general description of high density cascade effects has been reviewed by Thompson [1981].

Bascially, there are two parameters which influence the relative significance of the energy spike in establishing the damage for a given ion-target system, they are (i) the average energy density deposited in elastic collisions, $\tilde{\Theta}_\nu$ over the cascade volume and (ii) the time required to dissipate the spike energy, i.e. the spike life time. The $\tilde{\Theta}_\nu$ is given by [Thompson (1970)],

$$\tilde{\Theta}_\nu = \frac{0.2\ \nu\ (E)}{N\ V_c\ R_v} \qquad (3.18)$$

where V_c is the volume of the central core of the cascade determined from the

statistical cascade parameters; i.e. longitudinal damage straggling $(\langle \Delta X^2 \rangle)^{1/2}$ and transverse damage straggling $(\langle Y^2 \rangle)^{1/2}$ [Winterbon (1975)].

and R_v is the ratio of the individual cascade volume to the statistical cascade volume.

The average individual cascade volume is determined from Monte-Carlo simulation of several collision cascades [Walker (1977)]. Sigmund [1974] has attempted to define the spike lifetime in terms of normal thermal conductivity considerations for the deposited energy density which, depending upon the material ranges from 10^{-14} to 10^{-11} sec.

3.2. The Nature of Lattice Disorder

In this section, crystal lattice defects produced by heavy ion implantation into metals and semiconductors are discussed. The nature of the damage produced depends on the chemical bond and the structure of the target as well as on the implanted ion species, its energy and dose, and the implantation temperature.

The lattice defects produced in the solids are caused by kinetic energy transfer from the energetic incident ions to the target atoms. When the energy transfer exceeds the threshold displacement energy of the target atom (≈ 10-50 eV), the atom can be displaced permanently from its equilibrium lattice site resulting in an unoccupied site called a vacancy. When the displaced atom or ion comes to rest in a metastable position in the interstices of a lattice it is called an interstitial. This interstitial-vacancy pair is called a Frenkel defect. The displaced atom can either remain in the interstitial site or it may migrate to a sink such as a grain boundary or surface. If the latter occurs, the resulting vacancy is known as a Schottky defect. If vacancies are formed in a compound crystalline material with ionic character, electrical charge neutrality must be maintained and this will result in as many anion vacancies as cation vacancies being produced. In semiconductors, the vacancy may be electrically neutral or have several charge states depending on the position of the Fermi level and whether it acts as a donor or acceptor.

An interstitial introduces considerable lattice strain in the surrounding region compared to the strain produced by a vacancy. In general for metals, the interstitial formation energy, $E_{i.f.}$, is considerably higher than the energy for the formation of a vacancy. Hence, it is expected that interstitials would migrate at a lower energy, $E_{i.m.}$ than vacancies, thereby relieving the strain locally. $E_{i.m.}$ is typically an order of magnitude lower than the vacancy migration energy, $E_{v.m.}$. For example, in CdS, $E_{i.m.}$ for Cd and S are $\simeq$ 0.29 eV and $\simeq$ 0.22 eV respectively [Elsby (1971)], while $E_{v.m.}$ is several eV. Vacancies and interstitials may combine spontaneously over short distances and effectively annihilate and restore lattice perfection. The extent of this mutual annihilation zone has been calculated for copper [Gibson et al. 1960] and found to extend up to 50-100 atomic volumes. Defects may also migrate depending upon their mobility and agglomerate to form clusters. By forming clusters, the overall strain is reduced in the lattice compared to that due to the same number of isolated defects. The common forms of three dimensional clusters are precipitates (cluster of interstitials) and voids (clusters of vacancies).

Another type of lattice imperfection is called a dislocation. A dislocation can be considered as the boundary between two regions (slipped and unslipped) of a surface which are perfect themselves but are out of register with each other. Basically, there are two types of dislocations. One is called an edge dislocation in which an extra half plane of atoms (ABCD) is imagined to be inserted into the lattice, as shown in Fig. 3.5 (a). The edge of the extra plane is called an edge

dislocation line. The other type of dislocation is screw dislocation, in which the lattice is imagined to be sheared on one side of ABCD relative to the other side in the direction AB (Fig. 3.5 (b)). The boundary between the sheared and unsheared regions on plane ABCD (i.e. CD) is called a screw dislocation.

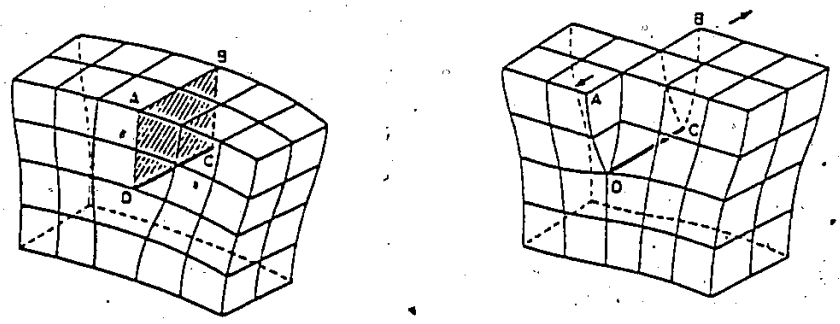

Fig. 3.5 (a) An edge dislocation DC formed by inserting an extra half plane of atoms in ABCD (b) a screw dislocation DC is formed by displacing the face ABCD relative to each other in the direction AB [from Hull (1975)].

A dislocation is defined in terms of a Burgers vector ($\vec{b}$) and a dislocation line. The Burgers vector is defined as a closure failure of the atom to atom path (called a Burger circuit) taken in a perfect crystal compared to the identical circuit taken in the crystal surrounding dislocation as shown in Figs. 3.6 (a) and (b) for an edge dislocation, and Figs. 3.7 (a) and (b) for a screw dislocation. The Burgers vector is then defined as the vector joining the points Q to M. The Burgers vector indicates how much and in what direction the lattice has slipped with respect to the unslipped region. The Burgers vector of an edge dislocation is normal to the line of dislocation while for a screw dislocation it is parallel. The Burgers vector of a dislocation is always the same and is independent of the position of the dislocation.

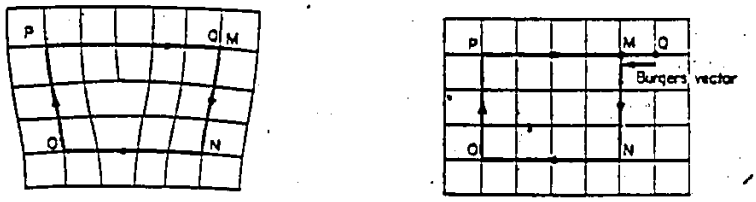

Fig. 3.6 a) A Burgers circuit around an edge dislocation,
b) the same circuit in a perfect crystal; the closure failure (QM) is the Burgers vector [from Hull (1975)].

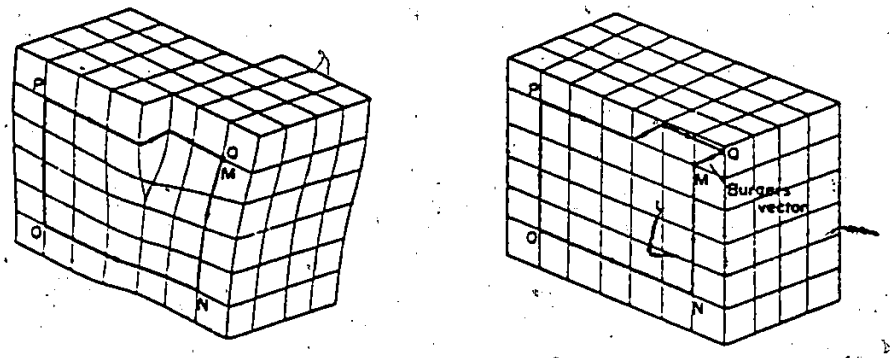

Fig. 3.7 a) A Burgers circuit around a screw dislocation,
b) the same circuit in a perfect crystal; the closure failure (QM) is the Burgers vector [from Hull (1975)].

When a dislocation is contained entirely within a crystal, so that the lattice outside and inside the boundary is perfect, the defect structure is called a dislocation loop. The simplest type of loop is a pure edge dislocation loop formed either by the coalescence of interstitials or vacancies for which the Burgers vector is perpendicular to the plane of the loop. This type of dislocation loop cannot glide and will not move conservatively under the action of an applied stress since the Burgers vector is not in the glide plane [Hull (1965)]. Such a dislocation loop is called a prismatic dislocation loop which is sessile by nature. A schematic representation of vacancy and interstitial loops is shown in Figs. 3.8 (a) and (b) respectively.

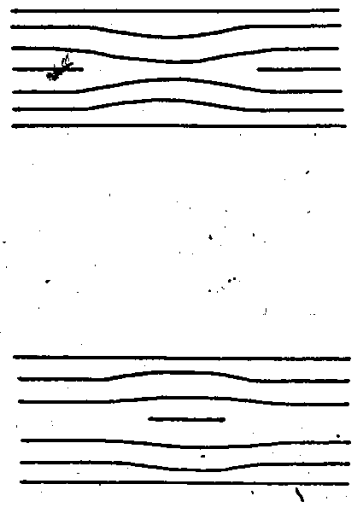

Fig. 3.8 Schematic illustration of the dislocation loop, a) vacancy type (b) interstitial type.

Another type of dislocation loop is one in which the loop and its Burgers vector lie on a glide plane. The nature of the dislocation changes with position along the loop right from pure edge, mixed dislocation to pure screw as shown in Fig. 3.9 (a) and (b). In addition there can be loops whose Burgers vector is neither parallel nor perpendicular to the plane of the loop.

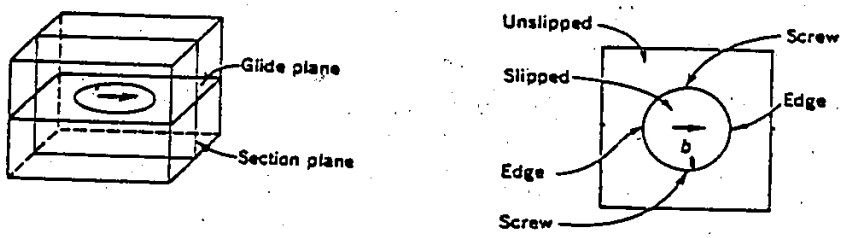

(a) (b)

Fig. 3.9 (a) A dislocation loop on a glide plane; b) with a mixed edge and screw dislocation [from Shewmon (1969)].

The Burgers vector of the dislocation loop is defined using the convention of Finish Start/Right Hand (FS/RH) [Hirsch (1970)], as illustrated in Figs. 3.10 (a) and (b) for vacancy and interstitial loops respectively. According to this convention an interstitial loop has a Burgers vector pointing upward and a vacancy loop has a Burgers vector pointing downward, perpendicular to the plane of the loop.

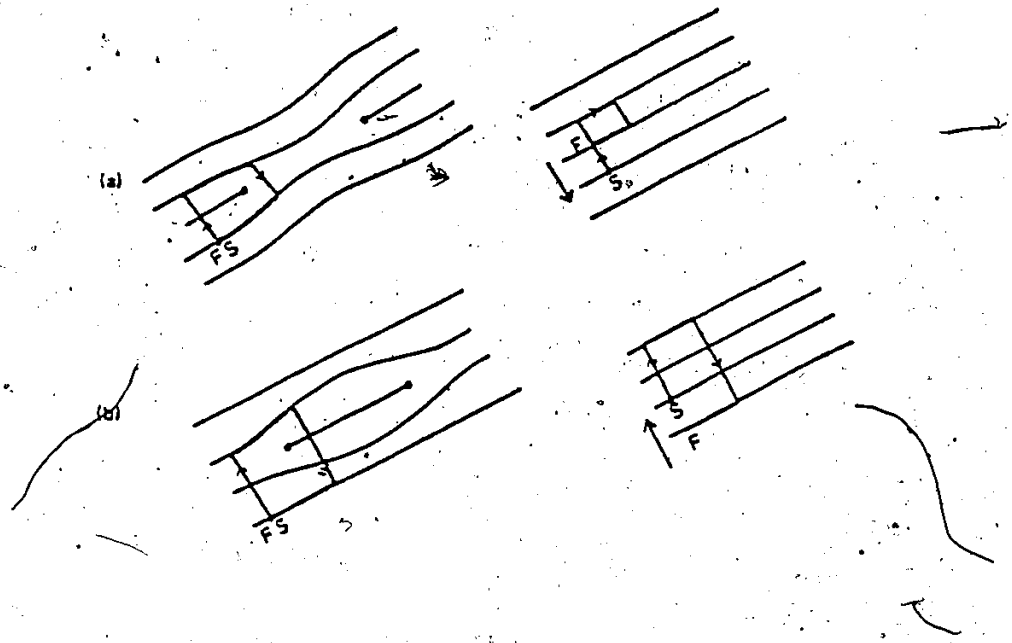

Fig. 3.10 Illustration of the FS/RH convention for defining Burgers vector for (a) a vacancy dislocation loop and (b) for an interstitial dislocation loop [from Lorreto and Smallman (1978)].

Dislocations and dislocation loops are examples of line defects in a crystal. However, a number of planar defects also exist in a crystal, e.g. stacking faults, grain boundaries, twin boundaries, and low angle boundaries. A stacking fault in a crystal results when the stacking of an atomic plane or planes deviates from the normal stacking sequence. The lattice on either side of the fault is perfect. The stacking sequences of sphalerite and wurzite are shown in Figs. 3.11 (a) and (b) respectively, which are represented as follows

sphalerite a α c γ b β a α c γ b β - - - -

wurtzite a α b β a α b β a α b β - - - - .

There are two types of stacking faults in the wurtzite structure; Type I contains one violation of the stacking sequence, or one triplet of a sphalerite structure, while Type II contains two violations of the stacking sequence, or two triplets of the sphalerite structure. The Type I fault is represented as,

Type I a α b β a α b β c γ b β c γ - - -

and Type II fault is represented as

Type II a α b β a α b β c γ a α c γ a α - - - .

The Type I fault has a lower stacking fault energy than the Type II fault, since it contains only one violation of stacking.

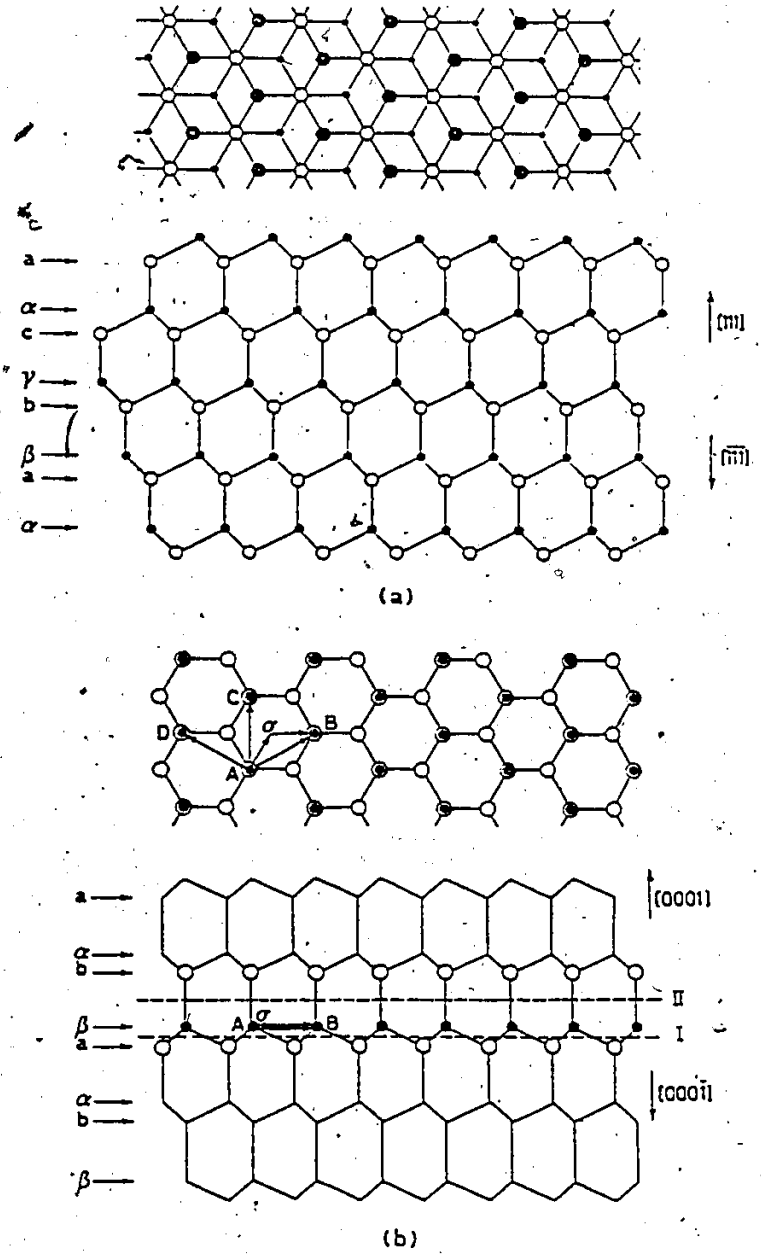

Fig. 3.11 The cross section and projection on the c-plane of sphalerite (a) and wurtzite (b) structures.

CHAPTER 4

ION IMPLANTATION DAMAGE ANALYSIS TECHNIQUES

Introduction: This chapter describes the principles of the TEM and RBS/channeling techniques applicable to the present investigation. Section 4.1 contains a general introduction to the operation of the transmission electron microscope, followed by theories of image contrast and characterization of lattice defects by TEM. In Sec. 4.2 the basic principles of Rutherford backscattering and the channeling techniques are outlined, followed by their application to the measurement of lattice disorder. The methods of data analysis adopted for the present work are also described.

4.1. Transmission Electron Microscopy

4.1.1. Introduction:

The transmission electron microscope is a well established tool for studying crystallographic defects present in crystalline materials. Basically, it consists of an electron source and an assembly of electromagnetic lenses mounted in a vertical column. The column is evacuated to a pressure better than 10^{-5} Torr. The thin sample (<0.1 μm thick) to be investigated is mounted on a goniometer capable of tilting the sample

along two orthogonal axes so that an appropriate set of crystallographic planes can be brought into a diffracting condition. Since the wavelength of high energy electrons (e.g. wavelength of 100 keV electrons is $\approx 3.7 \times 10^{-3}$ nm) is comparable to the magnitude of the lattice strain around a defect, a shadow is formed in the image when lattice planes affected by the defects are in diffracting condition. The resulting contrast in the image is called diffraction contrast.

The electron microscope can be operated in two principal modes; imaging or diffraction. The electrons transmitted through the sample are brought to focus in the back focal plane of the objective lens, forming a diffraction pattern. In the image mode, the image formed by the objective is further magnified by the intermediate and projector lenses while in the diffraction mode, the intermediate lens strength is reduced so that the back focal plane of the objective is focused on the viewing screen, forming a diffracting pattern from the illuminated area of the specimen. When the undiffracted beam is magnified to form the image, one gets a bright field (B.F.) image and when the diffracted beam is magnified to form the image, one gets a dark field (D.F.) image. The selection of B.F. or D.F. images are made by inserting an objective aperture in the back focal plane of the objective.

If another aperture (selector aperture) of diameter D is placed in the first intermediate image plane then those electrons traversing an area of diameter D/M of the specimen will reach the viewing screen, where M is the magnification of the objective lens. In this way, a

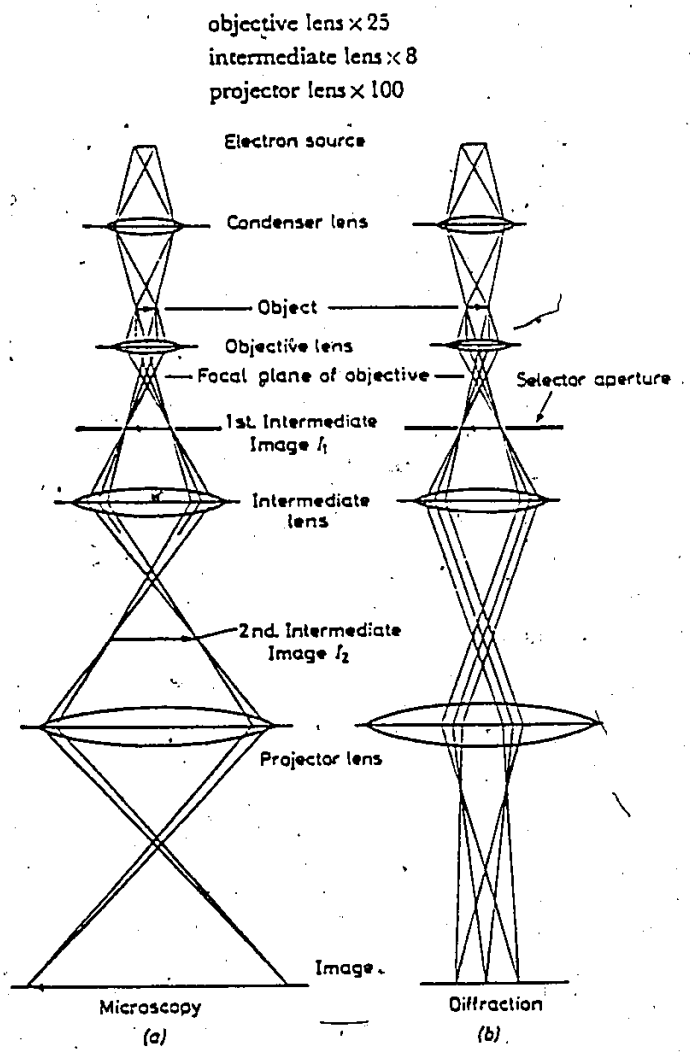

Fig. 4.1 Ray paths in the electron microscope (a) under imaging condition and (b) diffraction condition [from Hirsch et al. (1965)]

diffraction pattern from a small selected area of the sample is obtained. This mode of diffraction pattern formation is called selected area diffraction (SAD).

For proper interpretation of an image (electron micrograph) a SAD pattern from the same area and orientation of the sample is essential. Indexing of SAD patterns has become a standard practice and is dealt with in any text book on electron microscopy [Hirsch et al. (1965) and Edington (1975)]. Once the SAD pattern is indexed the sample orientation (foil orientation) and the electron beam direction ($\bar{B}$) can be determined.

Since very thin samples are essential for transmission of electrons, the reciprocal lattice points of such thin samples get elongated in the form of a rod perpendicular to the foil surface. As a result of this, diffraction spots are obtained even when the reciprocal lattice points do not touch the Ewald sphere. For some defect analysis an additional parameter $\bar{s}_g$, the deviation vector joining the reciprocal lattice point to the Ewald sphere in a direction parallel to $\bar{B}$, is required (Fig. 4.2).

A brief discussion of image contrast theories and methods of characterizing lattice defects pertinent to the present work is given below.

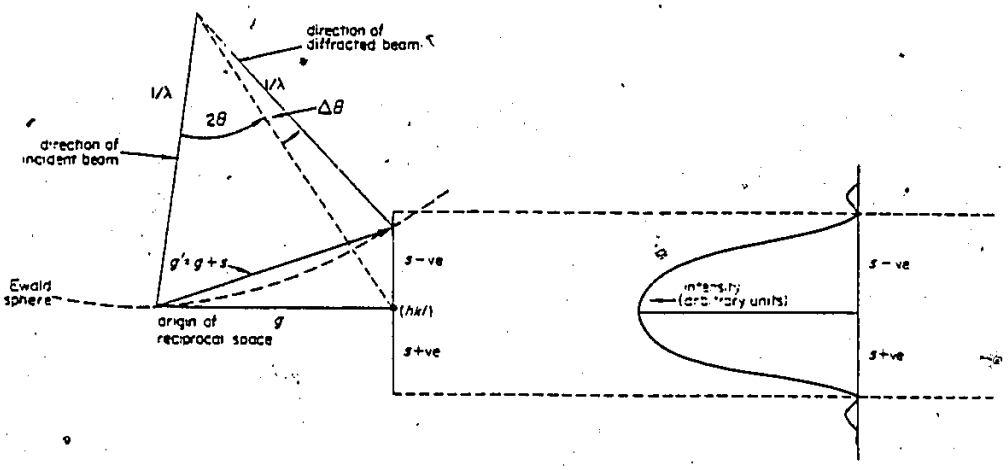

Fig. 4.2 The deviation parameter $\bar{s}_g$ in the terms of the Ewald sphere in reciprocal space [Loretto and Smallman (1978)].

4.1.2. Theories of Image Contrast

To develop the theories of image contrast two simplifying assumptions are usually made. In the first assumption the crystal is theoretically divided into small columns parallel to the diffracted beam direction and these columns are considered independent of each other. The intensity at the bottom surface of the crystal is then obtained by calculating the intensity at the bottom of each column. This approximation is known as column approximation. In the second assumption two beams are considered, one which is strongly diffracted and the other which is transmitted. This assumption is known as the two beam approx-

mation. In the following section two theories of image contrast are discussed: (a) kinematical theory and (b) dynamical theory.

(a) Kinematical theory

Apart from the assumptions made above, the kinematical theory assumes that (i) the electrons are scattered only once and (ii) the depletion in the intensity of the incident beam due to scattering of electrons from the column is considered to be very small and can be ignored.

In order to calculate the intensity at the bottom of each column in a perfect crystal, each column is imagined to be divided into small slabs perpendicular to the direction of the diffracted beam. The intensity contribution from each slab is then calculated assuming that each slab acts as a Fresnel zone and that these contributions are summed up to get the intensity at the bottom surface of the column. The amplitude of the diffracted beam ϕ_g, is then given by

$$\phi_g = (\pi i/\xi_g) \int_0^t \exp [-2\pi i \bar{s}_g z] dz \qquad (4.1)$$

where ξ_g is called the extinction distance for the operative reflection $\bar{g}$, defined as a critical distance in a perfect crystal at which the transmitted intensity falls to zero before increasing again

t is the thickness of the sample.

ξ_g is given as,

$$\xi_g = \pi V_c \cos\theta_B / \lambda f(\theta) \qquad (4.2)$$

where V_c is the volume of the unit cell

$f(\theta)$ is the atomic scattering factor for scattering through an angle θ

θ_B is the Bragg angle.

If $\bar{s}_g$ is not a function of the crystal thickness then integration of eq. (4.1) gives

$$\phi_g = (\pi i/\xi_g)(\sin(\pi t\bar{s}_g)/\pi\bar{s}_g)\ \{\exp(-i\pi t\bar{s}_g)\}. \qquad (4.3)$$

and the intensity of diffracted beam I_g becomes,

$$I_g = \phi_g^2 = (\pi^2/\xi_g^2)(\sin^2\pi t\bar{s}_g/\pi^2\bar{s}_g^2). \qquad (4.4)$$

If $\bar{s}_g \neq 0$ the intensity of the diffracted beam oscillates for increasing sample thickness. Such intensity variation with increase in sample thickness gives rise to thickness fringes which are found in almost all electron microscope specimens.

There are limitations to this simple theory for example,

a) if assumption (i) is to be valid, the thickness of the sample has to

be much smaller than the ξ_g, so that there are not enough scattering centers to rediffract the electrons back to the transmitted beam by multiple scattering. Hence for lower order reflections the sample thickness must be a fraction of ξ_g or $\lesssim$ 10 nm (ξ_g for low order reflection is $\simeq$ 50 nm).

b) when $\bar{s}_g = 0$, eq.(4.4) reduces to

$$I_g = (\pi t/\xi_g)^2; \quad \text{and for} \quad t > \xi_g/\pi \quad \text{then} \quad I_g > I_o,$$

which implies that the diffracted intensity exceeds the incident intensity, which is physically meaningless. Such shortcomings are due to the basic assumption that the diffracted beam is always of very low intensity compared to the undiffracted beam (assumption (ii)), as seen to be true only at large values of $\bar{s}_g$ and/or in very thin crystals. To determine the influence crystal imperfections such as dislocations, stacking faults etc., have on the image contrast, the displacement $\bar{R}$ of a unit cell from its lattice position in the perfect crystal needs to be calculated. For a crystal containing defects Eq. (4.1) will be modified to

$$\phi_g = (\pi i/\xi_g) \int_0^t \exp\{-2\pi i(\bar{s}_g z + \bar{g}.\bar{R})\}\, dz. \qquad (4.5)$$

The expression for the displacement $\bar{R}$ depends upon the type of defects present, for example for a screw dislocation at depth t below the surface of a crystal, the displacement at a point P(x,y,z) (Fig. 4.3) is given by

$$\bar{R} = (\bar{b}/2\pi)\ \tan^{-1}\{(z-y)/x\} \qquad (4.6)$$

where $\bar{b}$ is the Burgers vector

and the scattered amplitude is given as

$$\phi_g = (\pi i/\xi_g) \int_0^t \exp\{-2\pi i(\bar{s}_g z+(\bar{g}.\bar{b}/2\pi)\tan^{-1}[(z-y)/x]\}dz \qquad (4.7)$$

By solving this expression a profile of the electron intensity as a function of distance from the defect can be obtained. Because of the simplifying assumption made in the kinematical theory, details of image contrast cannot be predicted properly. However, the Burgers vector of the dislocations can be determined by observing the image contrast under different diffracting conditions. If one compares the value of ϕ_g for perfect and imperfect crystals the two expressions differ only by the term $\bar{g}.\bar{R}$. Therefore, when $\bar{R}$ is perpendicular to $\bar{g}$, then $\bar{g}.\bar{R} = 0$ and the dislocation is predicted to be invisible. For example in a screw dislocation the displacement vector $\bar{R}$ is parallel to $\bar{b}$ and it will be invisible when $\bar{g}.\bar{b} = 0$. This situation corresponds to the case of the Burgers vector lying in the reflecting plane.

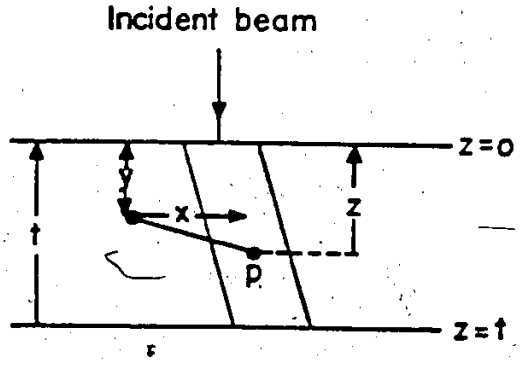

Fig. 4.3 Schematic illustrating the model used to calculate the amplitude of the diffracted beam on the bottom surface of the crystal [Loretto and Smallman (1978)].

(b) Dynamical theory

Dynamical theory of image contrast accurately describes the diffraction process occurring in the electron microscope. The assumptions which were made in the kinematical theory are discarded and now one considers that,

(i) electrons may be rediffracted back from the diffracted beam into the transmitted beam, and

(ii) absorption of electrons by the specimen can occur.

A more detailed formulation of the theory which includes several beams i.e. the multibeam case, is reviewed by Howie and Goringe [1971]. Since the theory allows the rediffraction of the transmitted and diffracted beams, the transmitted amplitude, ϕ_0, and diffracted amplitudes, ϕ_g, are coupled. The coupling is described by a pair of differential equations known as the Darwin Howie-Whelan equations,

$$\frac{d\phi_0}{dz} = \frac{i\pi}{\xi_0}\phi_0 + \frac{i\pi}{\xi_g}\phi_g \exp(2\pi i \bar{s}_g z)$$
$$\frac{d\phi_g}{dz} = \frac{i\pi}{\xi_0}\phi_g + \frac{i\pi}{\xi_g}\phi_0 \exp(-2\pi i \bar{s}_g z). \qquad (4.8)$$

Using this theory the depth variation of the transmitted intensity in a perfect crystal may be obatined from eq. 4.8.

The diffracted intensity I_g is given as

$$I_g = \phi_g^2 = (\pi^2/\xi_g^2) \cdot \sin^2(\pi t \bar{s}_{eff})/(\pi \bar{s}_{eff})^2 \qquad (4.9)$$

and the transmitted intensity is given as

$$I_o = \phi_o^2 = 1 - \phi_g^2 \qquad (4.10)$$

where $\bar{s}_{eff} = (\bar{s}_g^2 + \xi_g^{-2})^{1/2}$.

The intensity oscillates with depth, with a periodicity of ξ_g when $\bar{s}_g = 0$

$$\text{i.e. } \bar{s}_{eff} = \xi_g^{-1}$$

$$\text{and} \qquad \phi_g^2 = \sin^2(\pi t/\xi_g). \qquad (4.11)$$

It can be seen that ξ_g increases with increasing order of reflection because $f(\theta)$ decreases as θ increases. For $\bar{s}_g >> 0$ which is the case for the weak beam condition, $\bar{s}_{eff} = \bar{s}_g$ and Eq. 4.9 reduces to

$$\phi_g^2 = (\pi^2/\xi_g^2) \cdot \sin^2(\pi t \bar{s}_g)/(\pi \bar{s}_g)^2 \qquad (4.12)$$

which is as derived in eq.(4.4) for the kinematical condition.

The contrast from an imperfect crystal is considered in precisely the same way as in the kinematical theory i.e, by introducing an extra phase factor $2\pi \bar{g}.R$, we get

$$d\phi_o/dz = (i\pi/\xi_o)\phi_o + (i\pi/\xi_g)\phi_g \exp(2\pi i \bar{s}_g z + 2\pi i \bar{g}.\bar{R}) \quad (4.13)$$

$$d\phi_g/dz = (i\pi/\xi_g)\phi_o \exp(-2\pi i \bar{s}_g z - 2\pi i \bar{g}.\bar{R}) + (i\pi/\xi_o)\phi_g. \quad (4.14)$$

As seen in the kinematical theory, the invisibility criterion can also be applied here to determine the Burgers vector of the dislocations. There is a smooth transition from the dynamical theory to the kinematical condition which depends on the value of $\bar{s}_g \xi_g$. Consequently, the kinematical condition occurs as $\bar{s}_g$ increases.

4.1.3. Characterization of Lattice Defects by TEM

In this section image characteristics of some of the crystallographic defects relevant to the present study are summarized.

(i) Dislocations:

In the preceeding section it was shown that a screw dislocation is invisible when $\bar{g}.\bar{b} = 0$, which is known as the invisibility criterion. For an elastically isotropic solid, the displacement associated with a screw dislocation is in the direction of the Burgers vector. Therefore $\bar{g}.\bar{b} = 0$ is a sufficient condition for the invisibility criterion. However, for edge and mixed dislocations the displacement field is complex and therefore the invisibility criterion $\bar{g}.\bar{b} = 0$ is not sufficient for complete [illegible] of the dislocation image. For a pure edge dislocation it can be [Hirsch et al. (1967)] that the invisibility criteria are $\bar{g}.\bar{b} = 0$ and $\bar{g}.\bar{b} \times \bar{u} = 0$. If $\bar{g}.\bar{b} = 0$ but $\bar{g}.\bar{b} \times \bar{u} \neq 0$

a residual contrast of the dislocation image remains present, where $\bar{u}$ is the unit vector along the dislocation line.

The Burgers vector for dislocations can be determined by imaging the dislocations under the two-beam condition with several diffracting vectors. A pair of diffracting vectors $\bar{g}_2$ and $\bar{g}_3$ is obtained for which the dislocation goes out of contrast and is observed in the $\bar{g}_1$ reflection, i.e. $\bar{g}_2.\bar{b} = \bar{g}_3.\bar{b} = 0$ but $\bar{g}_1.\bar{b} \neq 0$ as shown in Fig. 4.4 for the case of an edge dislocation. This means $\bar{b}$ is perpendicular to both $\bar{g}_2$ and $\bar{g}_3$. For elastically anisotropic materials, dislocations are often of mixed character (having both edge and screw components) and have a complex displacement field associated with them. In such cases, dislocations do not go completely out of contrast but give a weak contrast when the above invisibility criteria are applied.

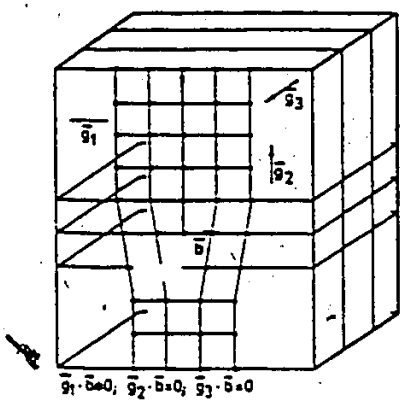

Fig. 4.4 Demonstration of the $\bar{g}.\bar{b} = 0$ rule for an edge dislocation. Only the lattice planes that belong to $\bar{g}_1$ are strongly bent, so that $\bar{g}_1.\bar{b} \neq 0$ whereas $\bar{g}_2.\bar{b} = \bar{g}_3.\bar{b} = 0$ [Reimer (1984)].

(ii) Dislocation loops:

In studying dislocation loops one is primarily interested in determining the type (i.e. interstitial or vacancy) and Burgers vector of the loops. For convenience, the dislocation loops are classified into two groups on the basis of their image contrast which in turn depends upon their size. They are:

(a) large loops with a diameter >10 nm which give clearly resolvable images. The general appearance of large dislocation loops is either circular or elliptical depending upon its orientation with respect to the electron beam direction.

(b) small loops of diameter <5 nm which appear as black-white dot contrast under dynamical conditions (i.e. $\bar{s}_g = 0$).

(a) Characterization of large loops

To distinguish the image contrast produced by dislocation loops of either vacancy or interstitial type, the case of a large prismatic loop is considered here. Fig. 4.5. illustrates vacancy (a) and interstitial (b) loops oriented on either side of the electron beam such that the distorted planes approach the Bragg condition. The position of the image of the loop is determined by the factor $(\bar{g}.\bar{b})s_g$. In the case illustrated, $(\bar{g}.\bar{b})s_g > 0$ for both types of loops. The image of the loop forms inside the loop as shown by the solid line in the figure. In contrast, for the opposite orientation ($(\bar{g}.\bar{b})s_g < 0$) of these loops the image will form outside the loop. If the sign of $\bar{g}$ or $\bar{s}_g$ is

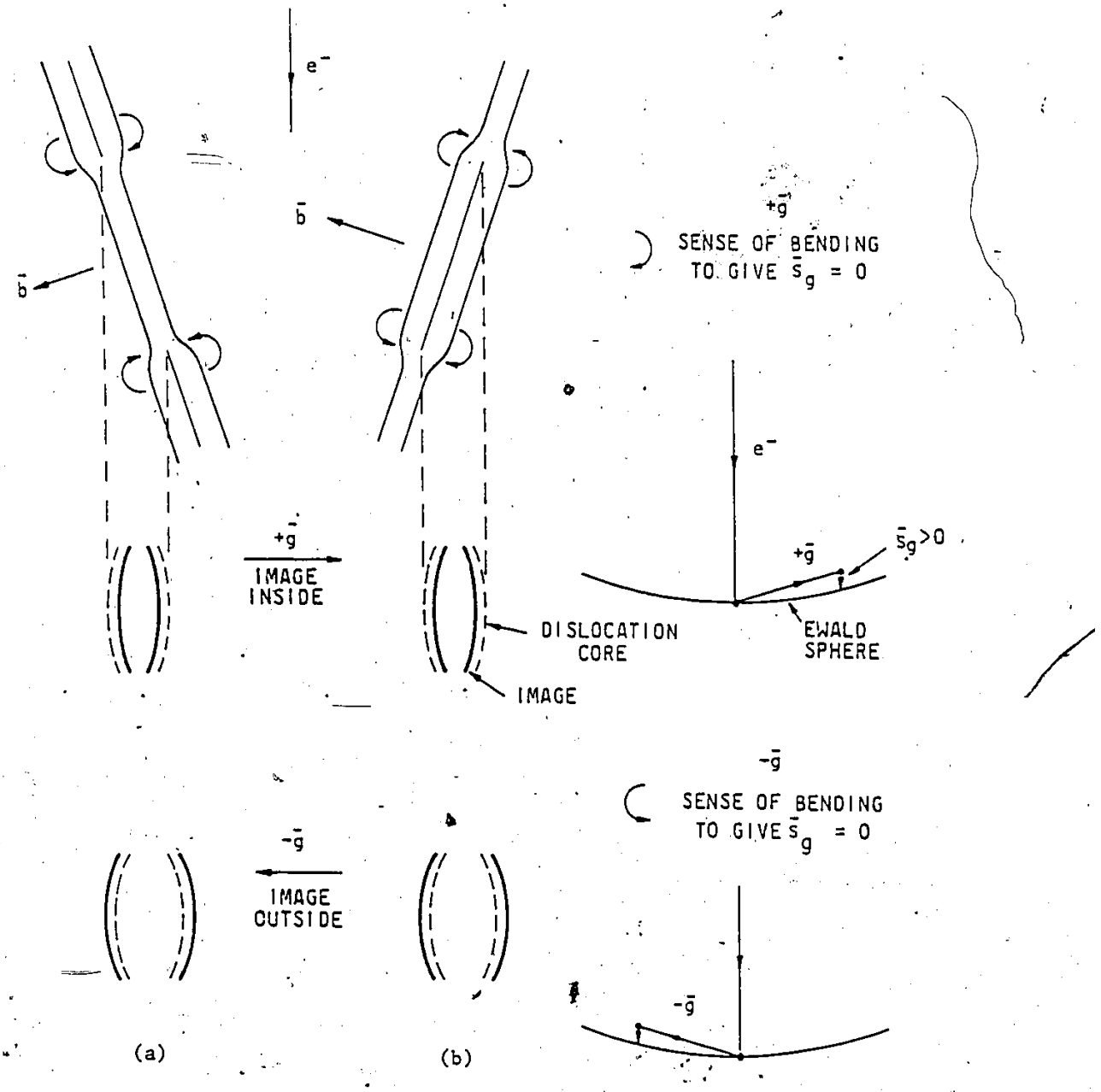

Fig. 4.5 The principles underlying the determination of the character of pure edge dislocation loops of (a) vacancy type (b) interstitial type [from Carpenter (1974)].

reversed, the image of the loop will shift from inside to outside the loop or vice versa. This forms the basis for determining the character of the loops provided the inclination of the loop plane is known.

(b) Characterization of small loops

Small loops (<5 nm) appear as black dots when imaged under kinematical conditions (i.e. $\bar{s}_g \xi_g > 1$). However, if the same loops happen to be near the sample surface they may give rise to black-white dot contrast when imaged under dynamical conditions (i.e. $\bar{s}_g = 0$). The diffraction contrast arising from small loops has been studied in detail by Wilkens et al. [1972]. To determine the nature of loops which give black/white dot contrast, a vector $\bar{T}$ is defined in such a way that it points from the center of the black dot to the center of white dot. The orientation of $\bar{T}$ with respect to $\bar{g}$ depends upon the depth from the surface. The nature of the contrast for interstitial and vacancy loops at different depths of the sample is schematically depicted in Fig. 4.6 (a) and (b) respectively.

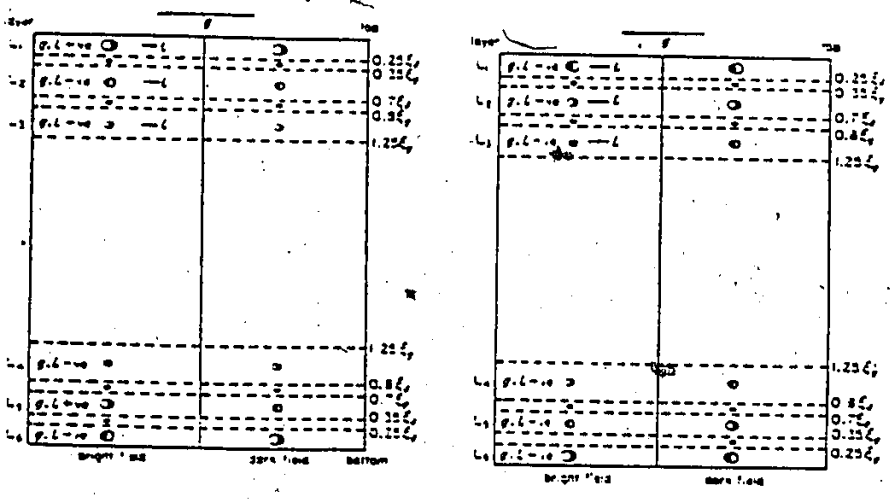

(a) (b)

Fig. 4.6 Schematic of diffraction contrast from small (a) interstitial loops and (b) vacancy loops from different depths within the sample [from Wilkens (1972)].

(iii) Stacking faults

Image contrast arising from stacking faults in the wurtzite structure has been studied by a number of workers [Black et al. (1962, 1964) Chadderton et al. (1963,1964)]. The general feature of the contrast consists of a parallel series of alternate dark and bright fringes of equal thickness. The stacking faults are invisible when $\bar{g}.\bar{R}_F = 0$, or an integer, where R_F is the displacement vector of the fault. The type of faults in the wurtzite structure has been identified by Black et al. [1964] by observing the contrast of the first and last fringe under various diffraction conditions.

4.2. Damage Analysis by RBS/Channeling

In this section the theoretical aspects of the RBS/channeling technique are given along with the procedures for obtaining the number of displaced atoms or scattering centers. Dechanneling of the aligned He^+ beam by various defects is also discussed.

4.2.1. Theoretical Aspects of the RBS/Channeling Technique

(a) Rutherford Backscattering

When a beam of high energy (typically 1-3 MeV) protons or helium ions strikes the surface of a target some of the incident particles will be elastically backscattered. The energy, E_1, of the particles scattered through an angle θ is related to the incident particle energy E_0 by

$$E_1 = KE_0, \tag{4.15}$$

where K is called the kinematic factor which is given by

$$K = \left[\frac{[1-(M_1/M_2)^2\sin^2\theta]^{1/2}+(M_1/M_2)\cos\theta}{1+(M_1/M_2)}\right]^2 . \tag{4.16}$$

The kinematic factor depends only on the ratio of the incident, M_1, to the target, M_2, atomic masses and on the scattering angle. The

likelihood of the occurrence of an elastic scattering event at an angle, θ, in the laboratory coordinate system is given, for $M_1 << M_2$, by

$$d\sigma/d\Omega = (Z_1 Z_2 e^2/4E_0)^2[\sin^{-4}(\theta/2) - 2(M_1/M_2)^2 + ----] \quad (4.17)$$

where $d\sigma/d\Omega$ is the differential Rutherford scattering cross-section.

Fig.4.7 illustrates the fundamental features of an experimental arrangement for Rutherford backscattering analysis. The incident beam of protons or helium ions is collimated with a set of apertures before impinging on the target. A small fraction of these particles will backscatter from the target. Part of this fraction is collected by a suitable particle detector (generally a silicon surface barrier detector) situated at an angle θ, with a solid angle $d\Omega$.

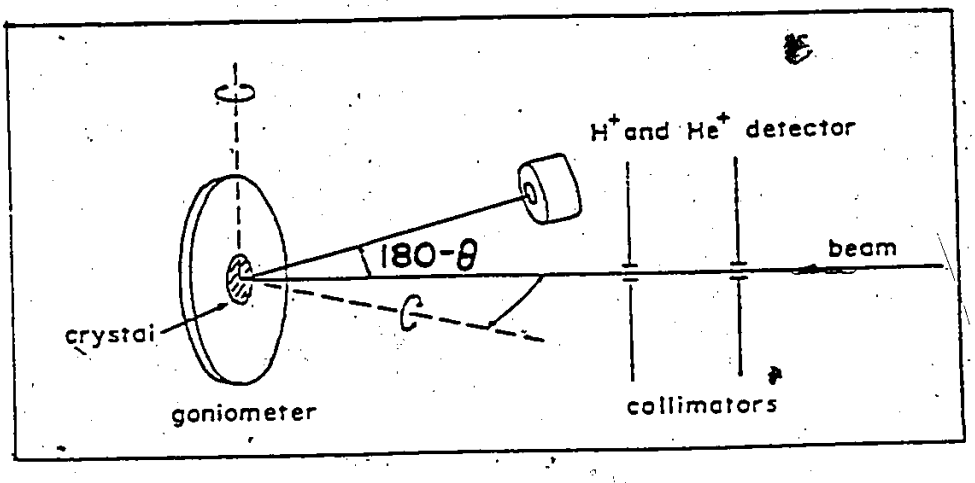

Fig. 4.7 Schematic diagram of the experimental set-up for a channeling-backscattering experiment

A typical backscattering spectrum from an amorphous target of atomic mass M_2 is shown in Fig. 4.8. The incident particles which are elastically scattered from the surface of the target are detected at an energy E_1, according to equations (4.15) and (4.16). This energy corresponds to the high energy edge of the spectrum. Those particles which penetrate into the sample steadily lose energy through inelastic collisions with target electrons. These may be backscattered elastically from different depths within the target and give rise to the plateau region of the spectrum. Since the differential scattering cross section is seen from equation (4.17) to be inversely proportional to the square of the energy immediately before the scattering event, the backscattering yield increases for particles that have penetrated deeper inside the target. Those particles which penetrate deeper inside the target and subsequently backscatter at a depth t, will lose energy during the ingoing trajectory and the outgoing trajectory. If it is assumed that the detected particles have suffered only one elastic collision at a depth t, then the energy of such particles after leaving the target may be used to establish the depth at which the backscattering event occurred.

The energy of the exiting particle is given by

$$E_1 = K (E_o - \Delta E_{in}) - \Delta E_{out} \qquad (4.18)$$

where ΔE_{in} and ΔE_{out} are the inelastic energy losses during the ingoing and outgoing trajectories (as seen in Fig. 4.8).

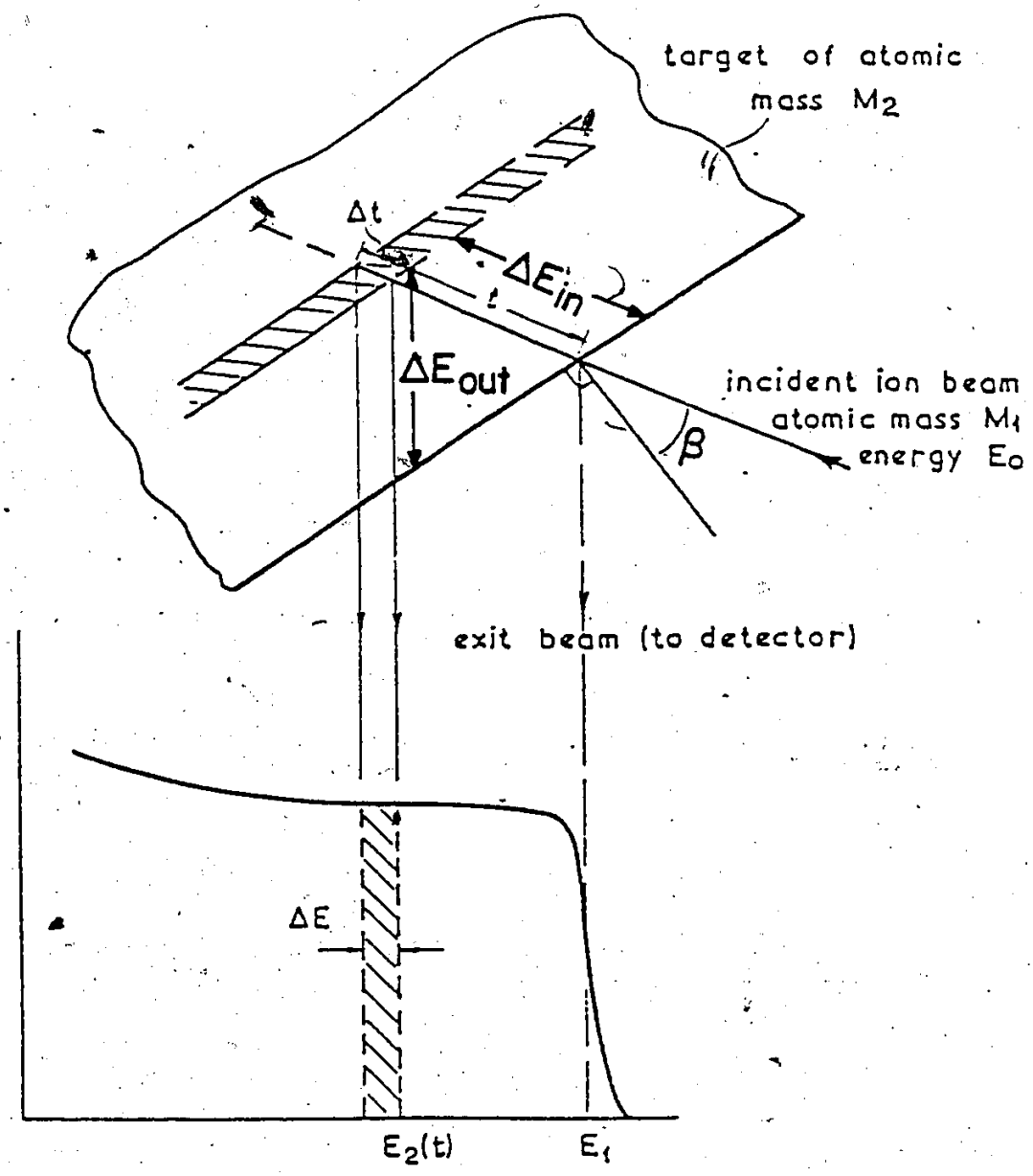

Fig. 4.8 A typical backscattering spectrum from an amorphous target.

For small values of t (≈100 nm), the stopping power during the ingoing trajectory $S(E_{in})$ and the outgoing trajectory $S(E_{out})$ can be considered constant.

Hence,

$$E_1 = K[E_o - tS(E_{in})/\cos\beta] - tS(E_{out})/\cos(180 - (\beta + \theta)) \quad (4.19)$$

where β is the angle between the surface normal and the incident trajectory.

Differentiation of Eq. (4.19) gives the required energy to depth conversion as

$$-\Delta E = \Delta t\,[\{KS(E_{in})/\cos\beta\} + S(E_{out})/\cos(180 - (\beta + \theta))] \quad (4.20)$$

The minimum value of Δt which can be measured i.e. the depth resolution, depends upon the energy resolution ($\Delta E''$) of the detector and the scattering angle. For a good quality Si surface barrier detector, $\Delta E'' \approx 15$ keV for MeV He^+ ions; then if $\beta=0$ and $\theta = 160^o$, the depth resolution for 2 MeV He^+ on CdS has a value of approximately ≈ 25 nm.

The depth resolution can be improved by modifying the scattering geometry such that the path length of the ingoing beam and/or outgoing beam is increased. This can be done by either tilting the

sample with respect to the incident beam (glancing angle of incidence) and/or installing a detector at a glancing exit angle. However there are practical limitations to the attainable depth resolution due to surface roughness, energy straggling and angle of acceptance into the detector [Williams (1975) and (1978)]. Also the glancing angle geometry introduces large inaccuracies in quantitative analysis if the angle is not known accurately. The depth resolution for 2 MeV He^+ on CdS as calculated for $\Delta E'' = 15$ keV, $\beta = 0$, $\theta = 100^0$ is $\simeq 6$ nm.

(b) Channeling

When a major axis or plane of a single crystal is oriented parallel to the direction of an energetic incident ion beam the ions are gently steered away from the atomic rows or planes by a series of correlated small angle collisions. The ions are then said to be channeled and this steering phenomenon is called channeling. The implication of this picture of channeling is that the channeled ions oscillate between the strings of atoms and never penetrate closer to the strings than the screening distance, a, (≈0.01nm). Thus close encounter processes such as those that occur in backscattering, the production of X-rays or in nuclear reactions are prohibited for channeled ions. The channeling phenomenon is well described in a number of books [Morgan (1973); Feldman, Mayer and Picraux (1982)] and excellent reviews [Gemmel (1974), Davies (1978)], hence, only a brief outline of the relevant part of the theory will be presented here.

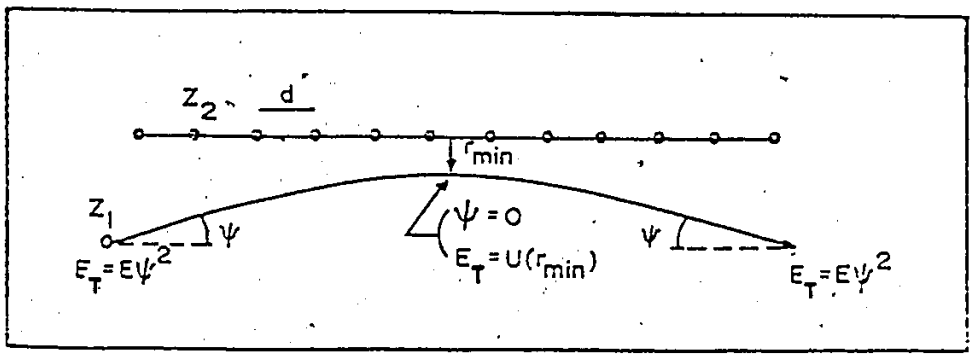

Fig. 4.9 Schematic diagram illustrating the channeling phenomenon

Fig. 4.9 illustrates the phenomenon of channeling in which an energetic beam of protons or helium ions is incident at an angle ψ with respect to the atomic rows. The angle ψ is smaller than a critical angle ψ_c, which is defined as the largest angle for which ions can maintain their channeled trajectories. Since many atoms in the rows are participating in the steering process, one may consider a continuum model [Lindhard (1965)] in which the nuclear charges of these atoms are assumed to be uniformly distributed along the row. Hence the trajectories of the channeled particles can be described in terms of a single continuum potential U(r), where r is the perpendicular distance from the atomic row. Lindhard [1965] gives the continuum potential as

$$U(r) = (Z_1 Z_2 e^2/d) \ln[(Ca/r)^2 + 1] \qquad (4.21)$$

where r is the distance from the row of atoms

d is the atomic spacing along the channeling direction, and

$C = \sqrt{3}$ is a constant.

U(r) is approximated as being independent of the distance along the row, and acts perpendicularly to the atomic row. An important consequence of this model is the conservation of the transverse energy of the channeled ions, E_T.

For a channeled ion,

$$E_T \simeq E_o \psi^2 + U(r). \qquad (4.22)$$

The concept of the critical angle for channeling emerges from the fact that when channeled ions approach the atomic row too closely the continuum approximation breaks down and the gentle steering process is disturbed as the ion interacts with individual atoms. Breakdown of this steady state process leads to dechanneling. The minimum distance of approach for which channeling occurs, r_{min}, corresponds to the case when ions are incident at the critical angle ψ_c. The critical angle ψ_c can be defined by the corresponding maximum transverse energy of the channeled ions i.e,

$$E_T^{max} = E_o \psi_c^2 \simeq U(r_{min})$$

$$\text{or} \quad \psi_c = \{U(r_{min})/E_o\}^{1/2}. \qquad (4.23)$$

Substituting for $U(r_{min})$ from equation (4.21) in equation (4.23) one determines that channeling occurs for angles,

$$\psi \leq \psi_c = \{Z_1 Z_2 e^2/E_o d) \ln[(Ca/r)^2 + 1]\}^{1/2}. \qquad (4.24)$$

Generally, except at low temperatures (<< 300 K), the thermal motion of the atoms in the direction perpendicular to the channel limits the minimum distance of approach r_{min}. Hence, a first order estimate of the critical angle ψ_c for axial channeling is obtained by substituting the transverse root mean square thermal vibrational amplitude, ρ_{rms} for r_{min} in equation (4.24),

$$\psi_c = \{Z_1 Z_2 e^2/E_o d) \ln [(Ca/\rho_{rms})^2 + 1]\}^{1/2}$$

$$\text{or} \quad \psi_c = (\psi_1/2) \ln [(Ca/\rho_{rms})^2 + 1]^{1/2} \qquad (4.25)$$

where $\psi_1 = (2Z_1 Z_2 e^2/E_o d)^{1/2}$, which is called the characteristic angle

Fig. 4.10 (a) shows the backscattered energy spectra for 1.0 MeV He^+ incident along the <111> axis and in a non-aligned direction in a silicon crystal, and Fig. 4.10 (b) shows the normalized backscattering yield as a function of tilt angle (angular scan) obtained for 1.0 MeV He^+ incident about the <111> direction in a silicon crystal. As can be seen, the backscattering yield decreases as the incident beam approaches the channeling direction. The half angular width at the half minimum, $\psi_{1/2}$, as shown in the Fig. 4.10 (b) is the experimental critical angle. The normalized minimum yield χ_{min}, as shown in Fig. 4.10 (b) is defined

as the ratio of the backscatter yield for an aligned incident ion beam to that in a non-aligned direction and is given by Lindhard (1965) as

$$\chi_{min} = Nd\pi(p^2_{rms} + a^2) \qquad (4.26)$$

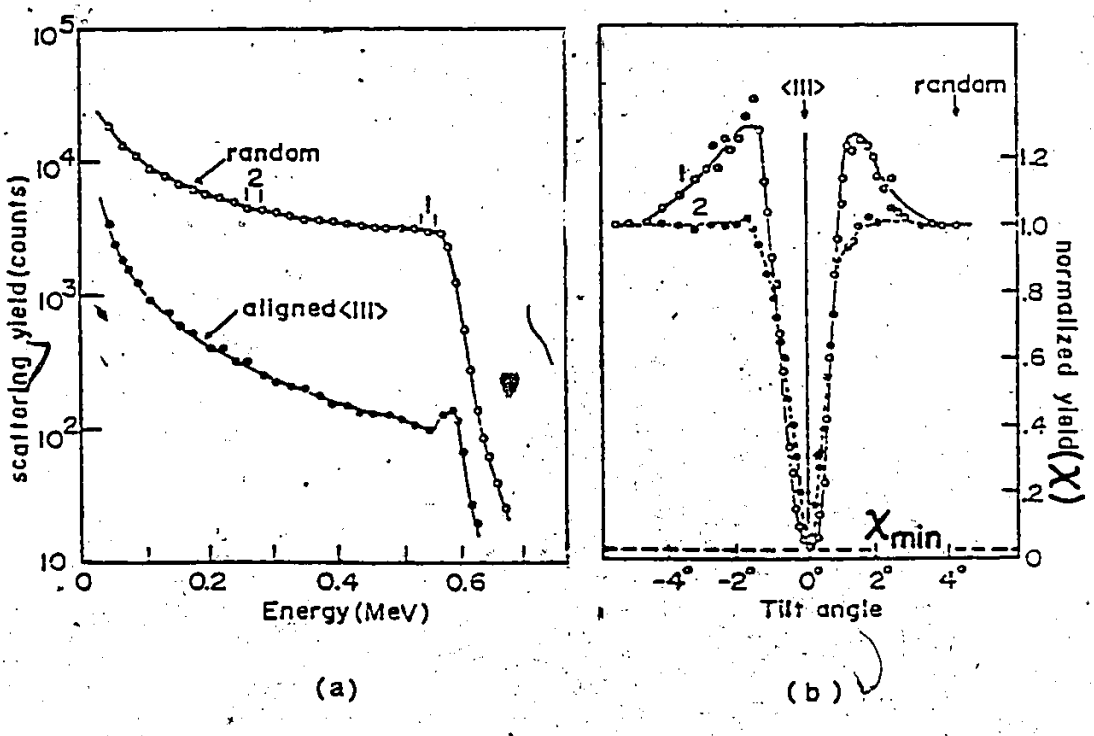

Fig. 4.10 a) RBS spectra for 1.0 MeV He^+ incident on Si along the <111> and non-aligned directions.
b) Orientation dependence of the energy regions 1 and 2 in (a) [from Walker (1977)].

Any experimentally measured value of χ_{min} is affected appreciably by the thermal vibrations of the lattice atoms, interstitial impurities, lattice defects in the crystal and also by the initial divergence of the incident beam. It is this behaviour that enables the channeling phenomenon to be used as an analytical tool in the study of lattice disorder, identification of lattice defects and determination of the lattice location of impurities in a crystal provided that the spatial distribution of the channeled ions (flux distribution) across the channel is known. The flux distribution across the channel can be calculated as explained below.

The ion flux $F(\bar{r},t)$ at any position $\bar{r}$, in the plane perpendicular to the channeling direction (transverse plane) can be calculated if the potential $U(\bar{r})$, at that point is known. The potential $U(\bar{r})$ can be calculated from the Moliere numerical approximation [1945] to the Thomas-Fermi interatomic potential and is given by

$$U(\bar{r}_{in}) = (Z_1 Z_2 e^2/\bar{r})(0.1e^{-6\bar{r}/a} + 0.35e^{-0.3\bar{r}/a} + 0.55e^{-1.2\bar{r}/a}). \quad (4.27)$$

Figs. 4.11 (a) and (b) show plots of equipotential contours as seen by He^+ ions incident along the two major axial channels in CdS. Atomic rows parallel to the c-axis, are formed by alternate Cd and S atoms while atomic rows parallel to the a-axis are formed by pure Cd and pure S atoms. For the mixed rows an average of Z_2 of Cd and S was taken in calculating the continuum potential. An ion entering the crystal at the point r_{in}, picks up an initial transverse energy $U(r_{in})$. If the

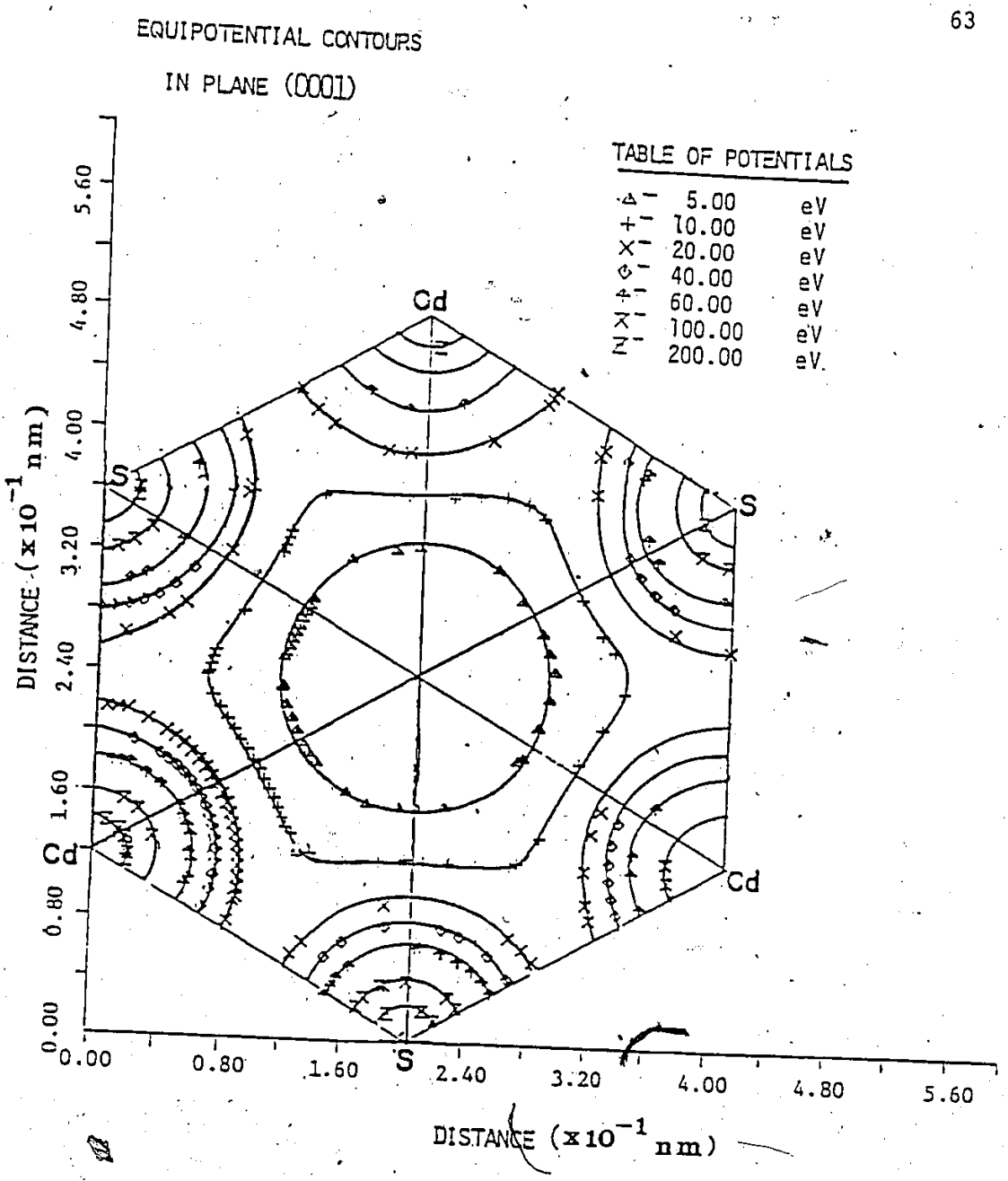

Fig. 4.11 a) Equipotential contours of the axial continuum potential for the He beam aligned along the c-axis.

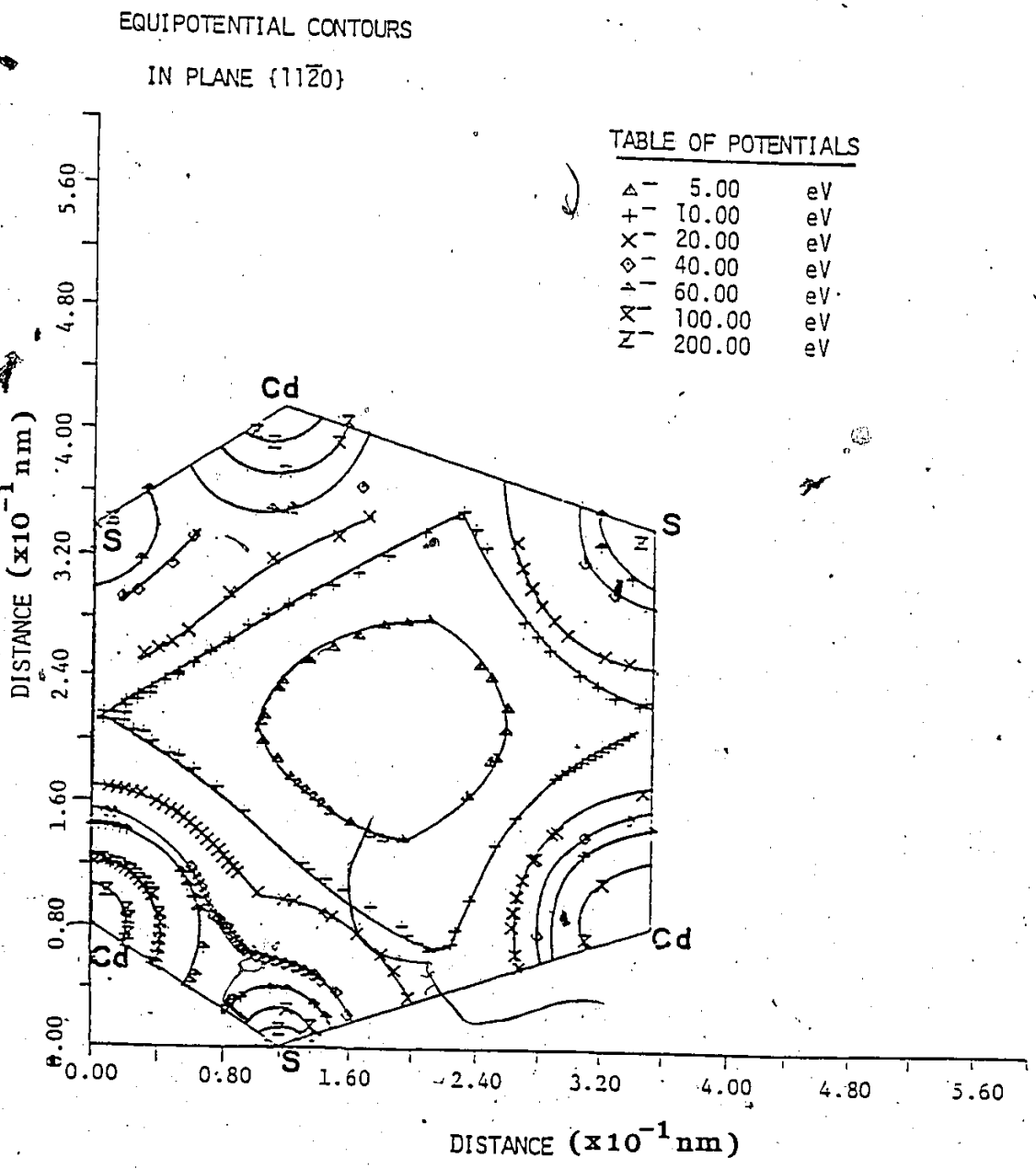

Fig. 4.11 b) Equipotential contours of the axial continuum potential for the He beam aligned along the a-axis.

angle of incidence with respect to the lattice row is ψ, then the total transverse energy, E_T, is given by

$$E_T = E(r_{in}, E_o, \psi) = U(r_{in}) + E_o \sin^2\psi. \qquad (4.28)$$

If defects are present within the channel then multiple scattering by these defects will lead to an angular divergence, $\delta(t)$, which increases with depth, t. This will result in an additional component to E_T in Eq. (4.28) of $E_o \sin^2\delta(t)$. For $\psi = 0$, the ion is constrained to move in the area $A(E_T)$ of the equipotential contour defined by r_{in}, E_o and $\delta(t)$. Lindhard [1965] has shown that after penetrating a certain depth ions reach a statistical equilibrium. In this situation, the ions have equal probability of being anywhere within $A(E_T)$. The probability of finding a particle somewhere in the allowed area $A(E_T)$ is given by

$$P(E_T, \bar{r}) = 1/A(E_T) \quad \text{for } U(\bar{r}) < E_T$$
$$= 0 \quad \text{for } U(\bar{r}) > E_T. \qquad (4.29)$$

The net probability of finding an ion at $\bar{r}$ can be found by integrating the above probability over the incident transverse plane perpendicular to the incident beam direction. This is given by

$$F(\bar{r}) = \int_{E_T > U(\bar{r})} dA(\bar{r}_{in})/A(E_T). \qquad (4.30)$$

From this result the flux at any point $\bar{r}$ in the channel for any incident angle can be calculated. Fig. 4.12 shows the flux distri-

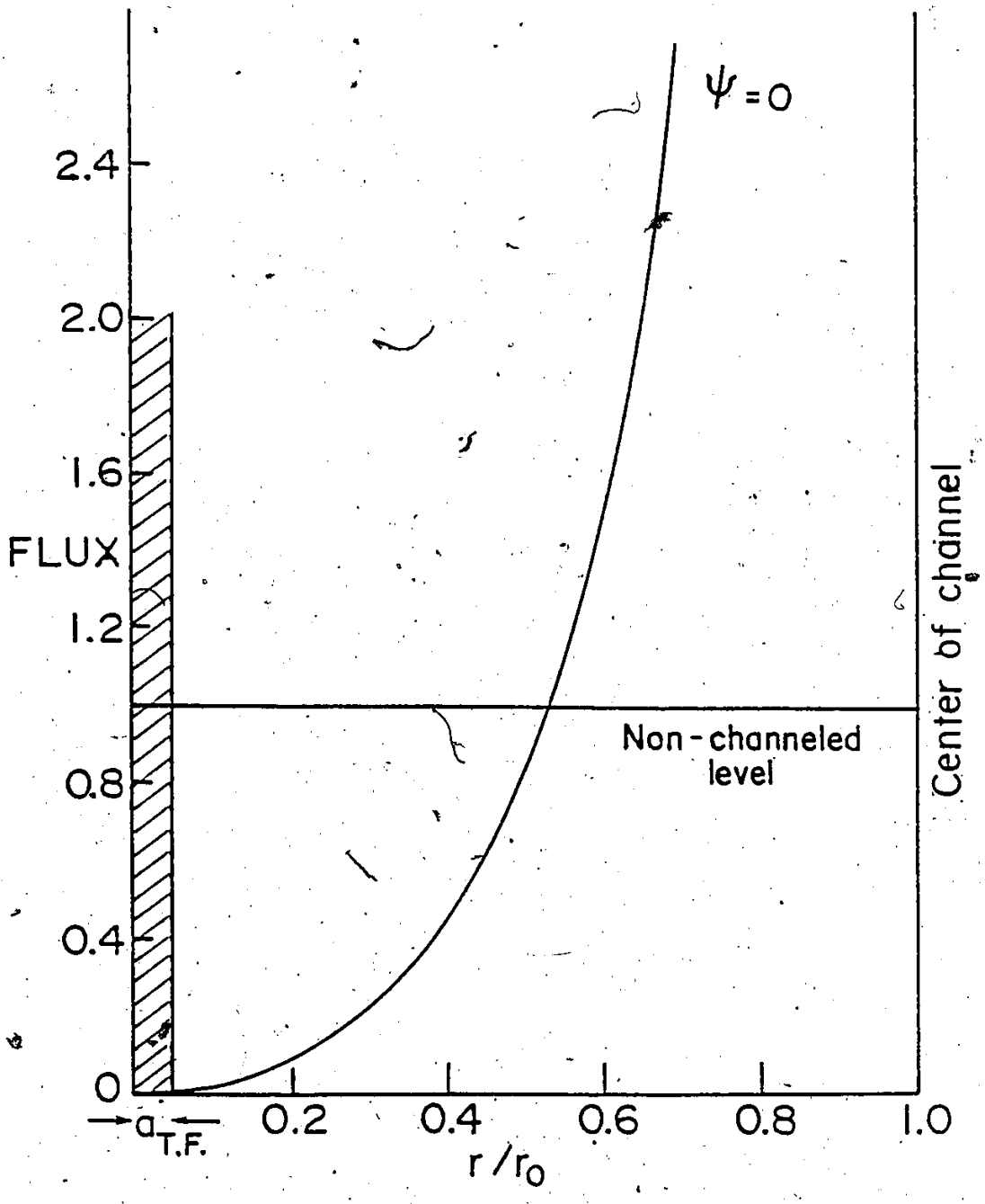

Fig. 4.12 Flux distribution of the He beam channeled along the c-axis as a function of distance from the row of atoms in the CdS crystal.

bution across the c-axis channel in CdS in terms of r/r_o (where r_o is radius of the channel) for 2 MeV He^+ ions. This plot shows that the effect of channeling is to transfer a spatially uniform distribution of channeled ions into a distribution that is peaked at the center of the channel. This feature of channeling is called flux peaking and shows that the flux intensity and hence the close encounter probability approaches zero near the atomic rows. The experimental evidence for flux peaking has been given by Andersen et al. [1971].

Flux peaking is an equilibrium process which requires a few hundred nanometers depth to become fully established. Also the amount of flux peaking is extremely sensitive to the initial perfection of the crystal, to the incident beam divergence, thermal vibrational amplitude and to the amount of lattice disorder in the crystal. All these parameters are sources of multiple scattering which reduce the flux peaking. While it is difficult to specify the extent of the flux peaking in any given situation, the flux near the lattice rows is always very small.

4.2.2 Damage Determination

In Sec. 3.1.4, it was mentioned that in ion implantation damage studies, one is interested in determining the total damage, the depth distribution of the damage and the type of defects produced. In this section methods of determining the above quantities are discussed.

To quantify the ion implantation damage, the measured backscatter yield needs to be separated into two components, one due to the backscattering of the channeled particles from the displaced atoms, and the other due to backscattering from all of the atoms of the crystal of particles that have been dechanneled at shallower depths. The analytical procedure for measuring damage can be explained with the help of Fig. 4.13 which shows the backscattering yield for 2 MeV He^+ incident along the c-axis and in a non-aligned direction on an unimplanted and a 40 keV Bi implanted ($1x10^{15}$ ions.cm^{-2}) CdS crystal.

The small peak that appears near the surface in the undamaged crystal spectrum is due to backscattering from atoms at the beginning of each row in the crystal; additional contributions can arise from the presence of a surface oxide or thin amorphous layer on the crystal surface. The backscattered yield for a damaged crystal exibits a larger peak due to backscattering from the displaced atoms and an increase in yield beyond the damage region because of the increased dechanneling of He ions as they pass through the damage region and are scattered by the defects through angles > ψ_c.

The backscattered yield under the damage peak, Y_D, after correcting for the dechanneled component is the result of weighting the radial distribution of the displaced atoms at a depth t, G(r,t), by the channeled beam flux distribution F(r,t), i.e,

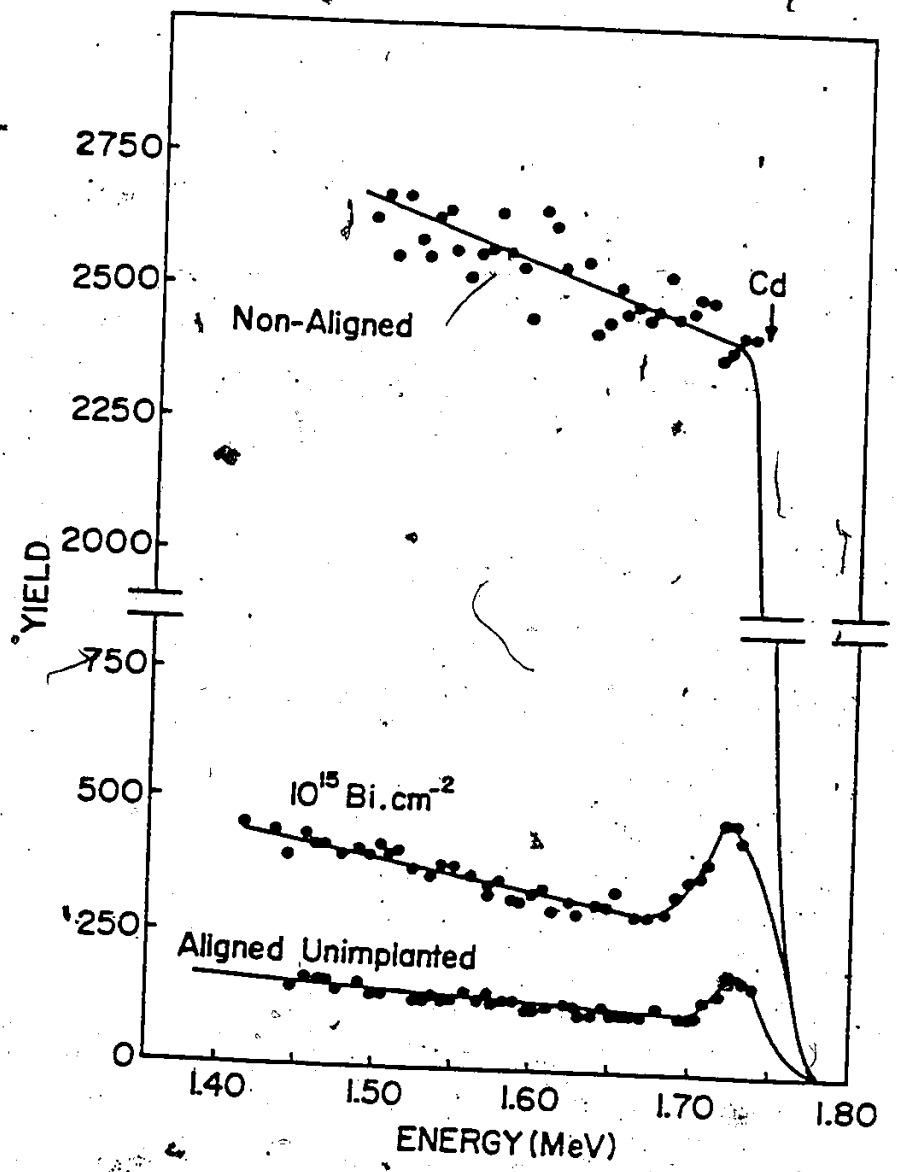

Fig. 4.13 Non-aligned and c-axis aligned RBS spectra for an unimplanted and 40 keV Bi^+ implanted ($1x10^{15}$ ions.cm^{-2}) CdS crystal.

Baxter [1977]

$$Y_D \propto \int_A G(r,t).\ F(r,t)\ dA \qquad (4.31)$$

where A is the area of the channel accessed by the beam

First it will be assumed that G(r,t) and F(r,t) are uniform across the channel and later the effects of nonuniformity of the distribution of the scattering centers across the channel will be discussed.

The analytical procedure by which the backscatter peak is related to the amount of damage present is based on the assumption that at some depth t, below the crystal surface, the incident aligned beam consists of an aligned and a non-aligned (random) component [Bøgh (1969)]. The probability for a transition from the random component to the aligned component is considered to be negligible [Bøgh (1969)]. The backscattering yield $Y_D(t)$ from a depth t, is given by

$$Y_D(t) = Y_N(t)\ [\{1-\chi_R(t)\}\ N_D(t)/N + \chi_R(t)] \qquad (4.32)$$

where χ_R is the non-aligned fraction of the analysing beam, given as Y_R/Y_D, where

Y_R is the backscatter yield for ions which have been dechanneled by scattering from lattice defects,

$N_D(t)$ is the atomic density of displaced atoms at a depth t, and

N is the atomic density of the crystal.

The first term on the right is due to the scattering of channeled ions from displaced atoms and the second term is due to the non-aligned portion of the beam. If equation (4.32) is solved for $N_D(t)$ one gets,

$$N_D(t) = N\,[\{Y_D(t)/Y_v(t)\} - \chi_R(t)]/\{1 - \chi_R(t)\} \qquad (4.33)$$

It can be seen from this equation that in order to obtain the concentration of scattering centers at a given depth, the random fraction of the beam at a depth t must be known. This requires a knowledge of the type of dechanneling behaviour which occurs in the damage region. An exact model for dechanneling will depend on the number of small-angle scattering events which characterize the channeled to non-channeled transition.

The total number of displaced atoms, $N_D = \int N_D(t)dt$ can be obtained using a simple linear dechanneling approximation. In this approach [Feldman (1971)] a straight line is drawn from the channel (a) behind the damage peak in the damaged spectrum to zero at the surface channel (b), as shown in Fig. 4.14 and a correction is made for the contribution from the undamaged yield to the total yield. The number of scattering centers (N_D) can then be calculated from the following equation.

$$N_D = N\Delta E_c/S_{Av}\;\frac{\sum_{i=a}^{c} Y_D(i) - (b-a)Y(a)/2 - [\sum_{d}^{c} Y_v(i) - Y_v(d).(b-d)/2]}{Y_N - Y_D(a)/2}\,, \qquad (4.34)$$

where points a, b, c and d are channels defined in the figure

S_{Av} is the average random stopping power of He ions incident on Cd in CdS and

ΔE_c is energy width of the channel.

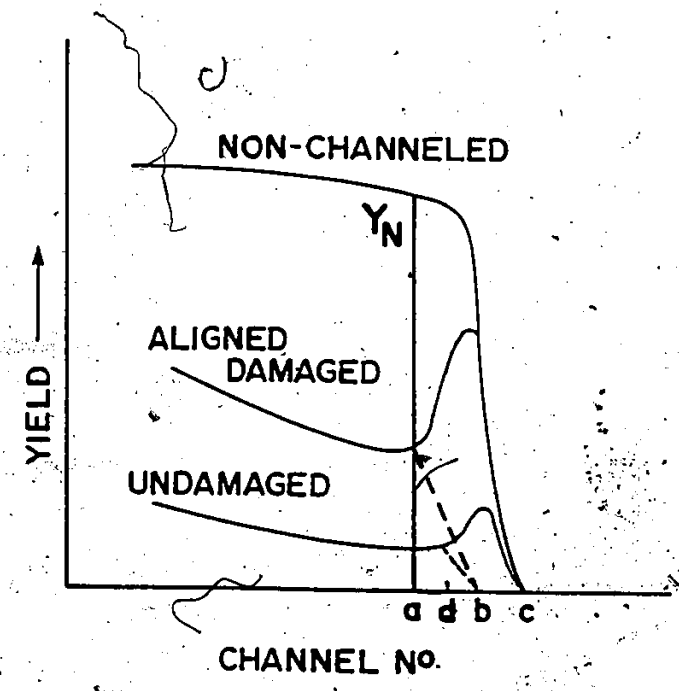

Fig. 4.14 The linear dechanneling approximation to determine the amount of disorder.

The use of a random stopping power for the aligned beam introduces some error in the value of N_D, since the stopping power for an aligned beam is always smaller than the stopping power for a non-aligned beam. The difference in the stopping powers depends upon the channeling direction, the incident beam energy, and also on the type and the amount of damage. The difference in stopping powers for the two directions was found to be about 30% for 1-2 MeV He^+ in an undamaged crystal [Böttiger and Eisen (1973)]. This difference decreases rapidly as the damage builds up in the crystal.

In the backscatter spectra of a damaged CdS crystal the cadmium disorder peak is distinctly observable while the sulphur disorder peak is much smaller and superimposed on high background due to counts from Cd atoms lying deeper in the target, consequently in the present study only the cadmium disorder was determined. Since the channeled beam will lose energy by inelastic scattering events with both the sulphur and the cadmium atoms of the crystal, an average of the Cd and the S atoms stopping power [Bragg rule (1905)] was used in the calculation of N_D. To facilitate the damage calculations, a computer program was used to determine the total damage. The total damage was calculated over the same depth for all the analysing beam energies.

When scattering centers are non-uniformly distributed across the channel, it is possible to obtain information on the radial distribution of the scattering centers $G(r,\phi)$, by measuring $N_D(t)$ for different values of area accessed across the channel. A method of

varying the accessed area of the channel by the incident beam is to tilt the crystal by a small angle ψ, ($<\psi_c$) away from the channeling direction. By doing this channeled ions will pick up additional transverse energy E_T, equal to $E_0\psi^2$, and move closer to the rows of atoms. The total transverse energy of the channeled ions then becomes (ref. eq. 4.28)

$$E_T = U(r_{in}) + E_0\psi^2 + \Delta E$$

where ΔE is the additional increase in transverse energy due to the finite collimation of the beam and to multiple scattering from the radiation damage as well as from inelastic scattering from atomic electrons.

By changing ψ the total transverse energy of the channeled ions can be varied. The radial distribution of the scattering centers can now be determined by measuring N_D for different values of transverse energy i.e. distance from the atomic rows. This method of determining G(r,t) has been applied by Foti et al.(1976) and Thompson et al. (1976).

4.2.3. Dechanneling by Defects

As discussed in Sec. 4.2.2 an incident aligned beam consists of channeled and non-channeled components within the target. Scattering from electrons, thermal vibrations, lattice defects such as point defects and extended defects provide mechanisms for scattering the

channeled component into a non-channeled condition. Once the incident particles are dechanneled, they may be scattered through larger angles because correlated collision events no longer occur and they may penetrate closer to the lattice atoms. Dechanneling in undamaged crystals at different temperatures has been studied by the Catania group for Si and Ge [1970] and by Davies et al. for W crystals [1972]. For the axial channeling case the Catania group reported a ρ^2_{rms} dependence of the dechanneling rate (dechanneling per unit depth), while Davies et al. found a weaker dependence on the vibrational amplitudes.

The presence of defects within the crystal increases the rate of dechanneling. The probability of dechanneling per unit depth (dP/dt), is given by the product of the dechanneling factor σ_D, which depends on the type of defect, and the defect density, N_D. If σ_D is known, the random fraction of the beam, $\chi_R(t)$, can be determined from

$$\chi_R(t) = \chi_v(t) + [1 + \chi_v(t)][1 - \exp\{-\int_0^t \sigma_D N_D(t')dt'\}] \qquad (4.35)$$

where $\chi_v = Y_R/Y_v$, Y_v is the minimum yield in the undamaged spectrum.

A detailed description of dechanneling by defects can be found in a recent review article by Pathak [1982] and an excellent book 'Materials Analysis by Ion Channeling, Submicron Crystallography' by Feldman, Mayer and Picraux [1982]. A brief description of dechanneling

by various defects follows.

a) Dechanneling by Point Defects

The defect dechanneling factor σ_D for isolated atoms in a channel is given by the Rutherford scattering cross section for particles scattered through an angle Θ, greater than the critical angle ψ_c,

$$\sigma_D(\psi_{1/2}) \simeq \int_{\psi_{1/2}}^{\infty} (d\sigma/d\Omega)d\Omega \qquad (4.36)$$

Substituting for $(d\sigma/d\Omega)$ from equation (4.17), and approximating for

$$\psi_{1/2} \simeq \psi_1 = (Z_1 Z_2 e^2/E_o d)^{1/2},$$

σ_D can be given as

$$\sigma_D = \pi Z_1 Z_2 e^2 d/2E_o. \qquad (4.37)$$

Thus, for a particular ion-target combination the dechanneling is inversly proportional to the energy of the analysing beam. This method of calculating σ_D assumes that dechanneling is caused by single collision events as discussed in Sec 4.2.2. The single scattering approximation holds for an areal atomic density of $< 10^{17}$ displaced atoms.cm^{-2}. If the areal density of randomly displaced atoms exceeds 10^{17} atoms.cm^{-2}, the number of scattering events increases and a plural [Feldman et al. (1970)] or multiple [Keil et al. (1960)] scattering

approximation should be applied. Dechanneling under these conditions has been treated by Luggujjo and Mayer [1973].

b) Dechanneling by Dislocations

Fig. 3.1 (a) shows a schematic of an edge dislocation with the Burgers vector, $\vec{b}$, normal to the dislocation line CD (a description of the dislocation is given in Sec. 3.2). Dislocations generate atomic displacements in the surrounding crystalline material where rows and planes are bent in such a way that neighbouring atoms in the rows and planes are shifted a small amount from their equilibrium position. When channeled particles pass through these distorted channels they encounter a smooth curvature of the channel. The effect of this curvature is to increase the transverse energy of the channeled ions thereby enhancing the dechanneling of the incident beam. An estimate of the dechanneling due to a dislocation can be obtained by determining the maximum amount of curvature of the channels which would allow the channeled particles to remain channeled after traversing the dislocation. Quéré [1968] has derived an analytical expression to obtain values for σ_D for dislocations. He assumed a cylindrical region around the dislocation axis referred to as the "dechanneling cylinder", inside which the lattice distortion is large enough such that particles entering this region will become dechanneled. In the region outside the "dechanneling cylinder" the lattice distortion is not large enough for dechanneling to occur. The results of this analysis showed that

$$\sigma_D = \kappa\,[a\delta]^{1/2}/\psi_1 \qquad (4.38)$$

where κ is a constant dependent on axial or planar channeling, dislocation type and orientation predicting an $E_o^{1/2}$.

The author calculated the values of κ for axial channeling averaged over all possible orientations, which are 0.40 for screw dislocations and 0.47 for edge dislocations. Equation (4.38) predicts an $E_o^{1/2}$ dependence of the dechanneling factor. The probability of dechanneling per unit depth dP_D/dt, is obtained by multiplying σ_D by the projected length n_D per unit volume of the dislocation,

i.e. $dP_D/dt = \sigma_D\, n_D(t)$.

Picraux et al. [1978] have developed a method to obtain the dechanneling factor from the experimental data of ion implanted aluminum and silicon crystals for both axial and planar channeling. The authors derived the following expression for the dechanneling probability assuming that the direct backscattering of channeled ions is very small compared to the total dechanneling,

$$dP_D/dt = \sigma_D\, n_D(t) = \ln[(1-\chi_v(t))/(1-\chi_D(t))]. \qquad (4.39)$$

Their results gave the same energy dependence of the dechanneling factor as the one obtained by Quéré. Results of Zn implanted Al crystals [Foti et al. (1977)] and Cu, Ga, Ge and Cs implanted Al crystals [Hussain and Linker (1980)] also showed the $E_o^{1/2}$ dependence for the dechanneling factor. Foti et al. further characterized the

damage by TEM and found the presence of dislocations in the implanted crystals.

As mentioned above, the dechanneling factor depends upon the channeling direction relative to the Burgers vector of the dislocations. For example, for edge dislocations, as shown in Fig. 3.5(a), particles channeled along the dislocation axis will have a minimal amount of dechanneling because there are effectively no planar distortions in the channeling direction, while particles channeled normal to the plane defined by the dislocation axis and the Burgers vector, will have maximum dechanneling because the planar distortion is maximum in this direction.

iii) Dechanneling by Dislocation Loops

The mechanism of dechanneling by dislocation loops is similar to that of dislocations, except that the extent of the distortion around the dislocation loop is much smaller because outside the loop the Burgers vector sums to zero [Hull (1975)].

The energy dependence of the dechanneling factor per unit length of a dislocation loop, due to circular vacancy loops in aluminum, has been theoretically investigated by Kudo [1976, 1978]. Figure (4.15) shows that the dechanneling width for channeled He^+ ions increases initially as $E_0^{1/2}$, reaching a maximum at $E_0 \approx 500$ keV, and has an almost constant value at higher energies. In the low energy regime channeled

ions preferentially feel a displacement field in the vicinity of the loop, where the displacement field is similar to that for a straight dislocation. At higher energies the period of the oscillations of the channeled ion trajectories becomes larger than the distorted region of the channel and hence the dechanneling width becomes independent of E_o. Results of Picraux et al. [1982] for the channeling of He^+ along (111) planes of Al containing dislocations loops agreed with this theoretical prediction.

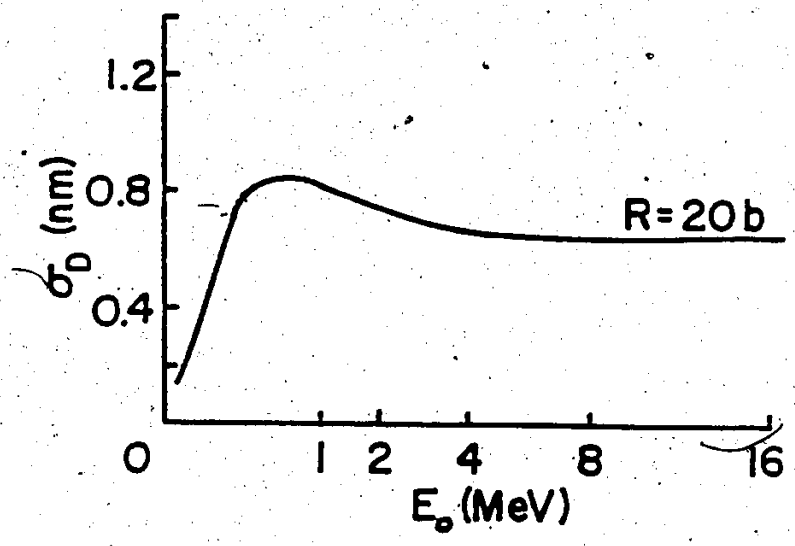

Fig. 4.15 Calculated energy dependence of the dechanneling factor, for a circular dislocation loop of radius R = 4.7 nm = 20xb, where b is the magnitude of the Burgers vector [from Kudo (1978)].

iv) Dechanneling Due To a Combination of Point Defects and Line Defects

So far, the discussion of dechanneling has considered individual types of defects, however a more general case would involve a combination of point defects and extended defects. In the following an attempt to separate the total dechanneling into the various components is given.

χ_{min} measured behind the damage peak at channel a is a summation of three dechanneling components. These components are:

i) dechanneling by multiple scattering from the target electrons and scattering from the vibrating nuclei in an undamaged crystal, $[\chi_v(a)]$,

ii) dechanneling by point defects produced by implantation $[\chi_R^P(a)]$, and

iii) dechanneling by extended defects produced by implantation, $[\chi_R^L(a)]$.

To separate the dechanneling component of the line defect, χ_R^L the following assumptions are made to simplify the calculation:

i) the dechanneling components are considered to be simply additive,

i.e.

$$\chi_{min}(a) = \chi_v(a) + \chi_R^P(a) + \chi_R^L(a) \qquad (4.40)$$

or
$$\Delta\chi_{min} = \chi_{min}(a) - \chi_v(a)$$
$$= \chi_R^P(a) + \chi_R^L(a).$$

The additivity of lattice dechanneling due to vibrations and point defects has been examined for various materials by Howe et al.[1976]. However in some cases they found that the total dechanneling deviated

appreciably from the additivity of the individual components. However, in the following calculation this deviation is ignored because of a lack of the exact knowledge of the amount of the deviation.

ii) dechanneled particles are not scattered back into channels; and

iii) the critical angle is not changed by the introduction of disorder.

χ_R^P is calculated for measured values of N_D (for randomly distributed atoms) using Bøgh's single scattering model [1968] at different energies, as shown in Fig. 4.16. $\chi_v(b)$ is measured experimentally. Hence, the dechanneling contribution by extended defects $\chi_R^L(b)$ can be determined.

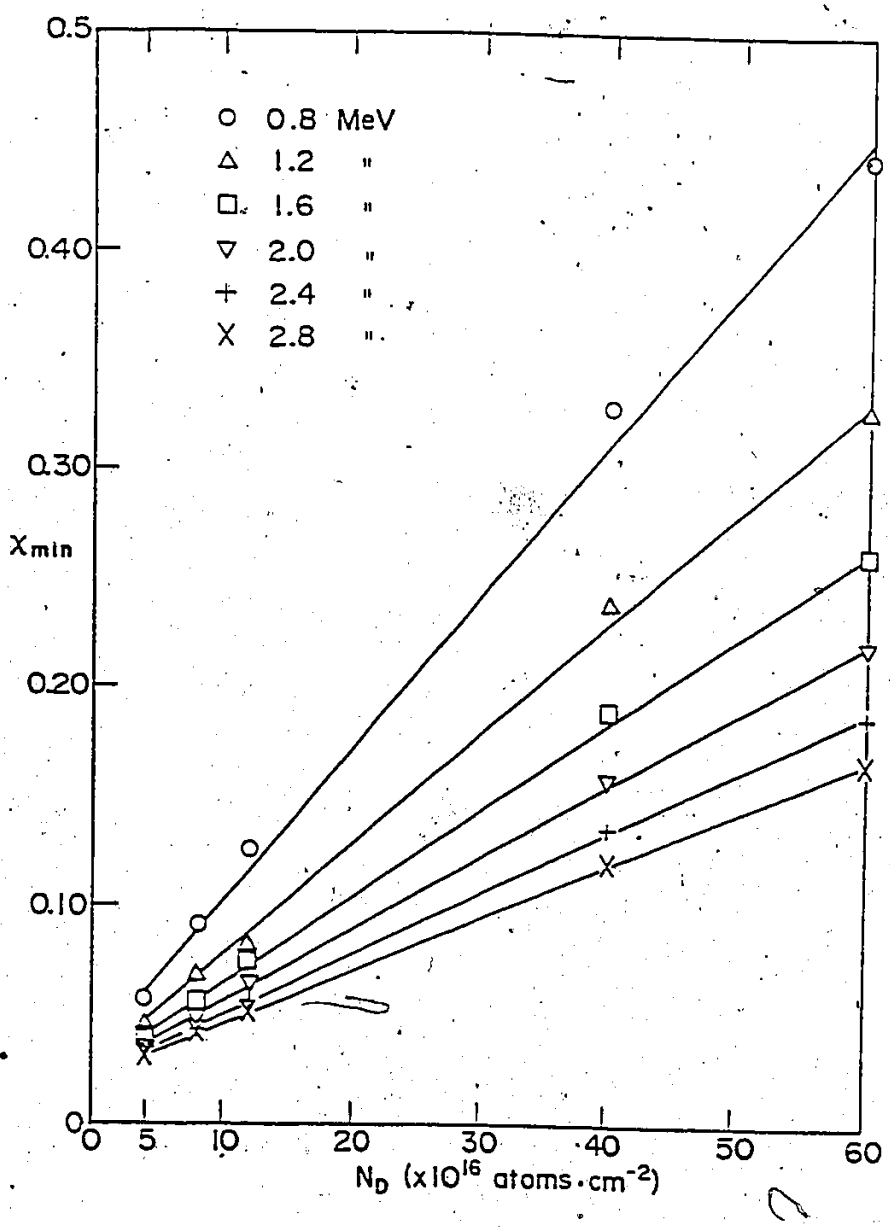

Fig. 4.16 Calculated χ_R^p vs. N_D using the Bøgh single scattering model vs. N_D for various He beam energies.

CHAPTER 5

EXPERIMENTAL TECHNIQUES

Introduction: Transmission electron microscopy and Rutherford backscattering/channeling techniques were used to study ion implantation damage in CdS crystals. This chapter describes the experimental facilities used for this work as well the method of sample preparation. Some relevant experimental parameters are also presented. The chapter is divided into two main sections. In Sec. 5.1. details of the transmission electron microscopy experiments are given while in Sec. 5.2. details of the ion implantation and RBS/channeling experiments are presented.

5.1. ELECTRON MICROSCOPY

5.1.1. The Transmission Electron Microscope

The TEM work presented here was carried out using two transmission electron microscopes, one at the McMaster University (Philips Model 300G) and another at PMRL-CANMET, Ottawa (Philips Model 400T). A preliminary study of implantation damage was done on the Philips 300G, while the Philips 400T microscope was used for the high resolution studies. The Philips 300G was operated at 100 kV with a fixed diffra-

ction aperture (1 μm) for selected area diffraction, while the Philips 400T was operated at 120 kV with an adjustable diffraction aperture. A cold finger situated near the sample was always maintained at liquid nitrogen temperature. This reduced the effective pressure in the vicinity of the sample which minimizes the carbon contamination on the sample.

5.1.2 Sample Preparation For TEM Studies

Thin flakes (a few microns thick) of CdS crystals were obtained from Cleveland Crystal Inc. Various techniques to thin the samples were attempted, of which the following one was most successful. The crystals were floated in a bath of dilute HCl (30 %), maintained at a temperature of 45° C. If the temperature of the etching solution was raised, etching of the crystals proceeded faster, and very small thin regions around the sample edge were produced. At lower temperatures the etching rate slowed down considerably. Crystals were removed from the solution from time to time to check the thickness using an optical microscope. Once the edges were thin enough they were rinsed with distilled water followed by a methyl alcohol rinse. The crystals were dried on lintless lens cleaning paper. These thinned samples were then mounted between a folded copper grid of mesh size 100. All the samples were examined in the TEM before implantation to check the crystal quality. Those samples which were found to have stacking faults or other growth defects were discarded.

5.2. Implantation and RBS/Channeling Experiments

In this section a coupled accelerator system is described which was used for 10-150 keV ion implantation and in-situ damage analysis by the backscattering/channeling technique. A brief decription of the target chamber, sample manipulation and data aquisition system is given in Sec. 5.2.2. A detailed description of the experimental set-up is given by Walker [1977]. In Sec. 5.2.3. the experimental procedure for surface preparation and alignment of single crystals of CdS for axial channeling is outlined and in Sec. 5.2.4. important experimental parameters are calculated.

5.2.1. Implantation and RBS/Channeling Apparatus

A coupled accelerator system shown schematically in Fig. 5.1, has been used for implantation and in-situ analysis. It consists of a 150 kV ion implanter and a 3.5 MV Van de Graaff accelerator. A beam from either accelerator may be directed to the target via a common analysing magnet, thereby allowing in-situ analysis of implantation damage to be carried out. A feedback circuit is used to stabilize the energy of either beam to ± 2 keV. Damage analysis was performed using 0.6 to 2.8 MeV He^+ ions from the Van de Graaff, with the beam being channeled parallel to either the c- or the a-axis of the CdS crystal. Typical He^+ beam current densities used in acquiring the aligned and non-aligned spectra were ≈ 10 nA/mm^2 and ≈ 5 nA/mm^2 respectively. The analysing beam was collimated using a pair of 0.75 mm diameter apertures

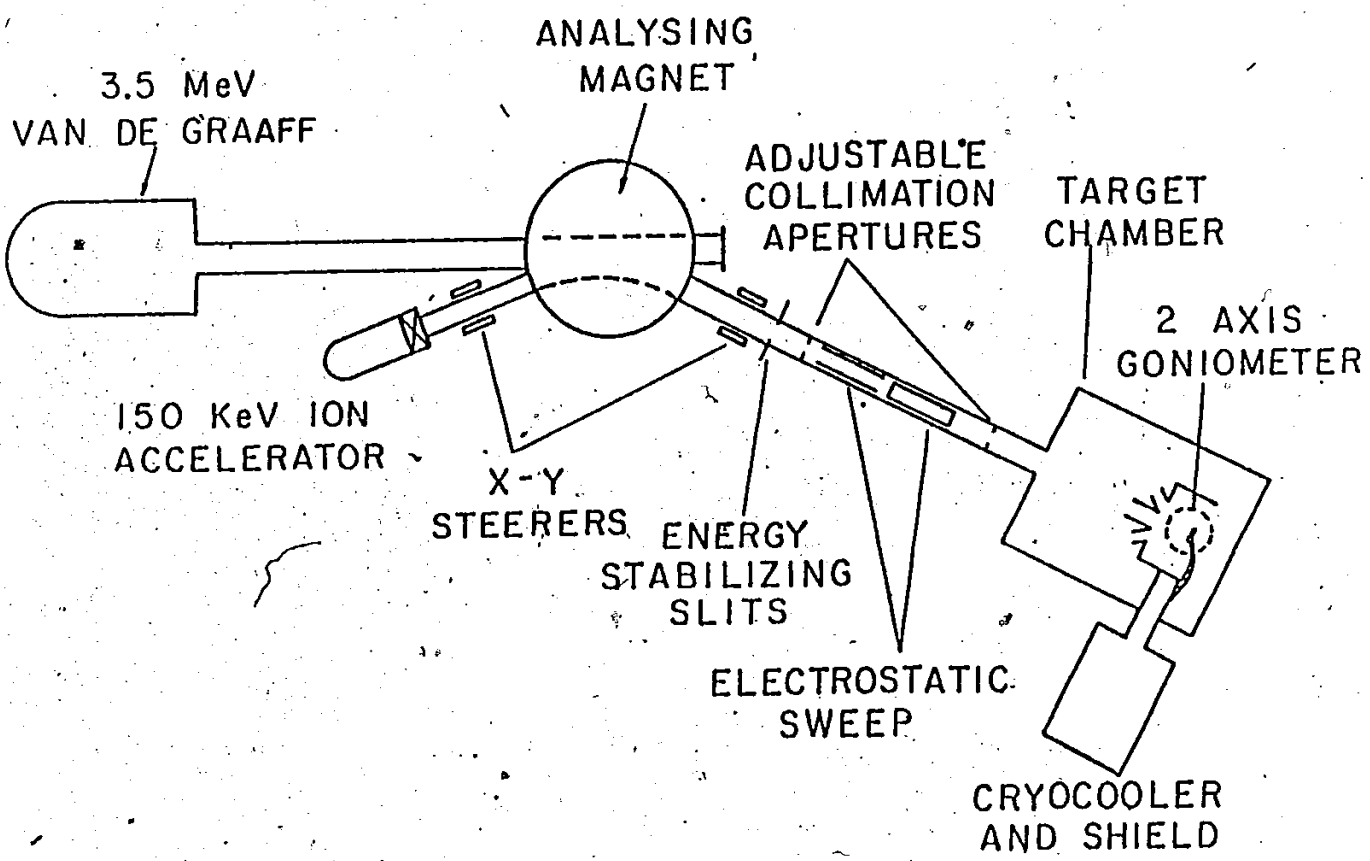

Fig. 5.1 Schematic of the McMaster University RBS and ion implantation facility

separated by 130 cm. This resulted in a half angular divergence of 0.026^{o}. The collimating apertures are movable vertically (resettable to <0.01 mm) so that analysis at different positions on the target could be performed.

The ion implanter used was a Texas Nuclear Corporation Model 9509 Cockroft-Walton neutron generator which was modified to accommodate a Danfysik 911A "Universal" ion source suitable for producing ions from gas and solid sources. During implantation, the collimating apertures were replaced by 2 mm and 4 mm apertures, the latter one being nearest to the target. To ensure the uniformity of the implant, the ion beam (after passing through the 2 mm aperture) was rastered horizontally and vertically across the 4 mm aperture using two pairs of electrostatic plates. Also both the apertures were placed off axis vertically with respect to the beam axis so that there is no direct path along the beam line from the magnet to the target. This ensures that implantation of ions neutralized between the magnet and target is avoided. The pressure in the system was $< 1x10^{-6}$ Torr.

5.2.2. Target Chamber, Sample Manipulation and Data Aquisition

Fig. 5.2. shows a schematic of the interior of the target chamber. The sample is mounted on a goniometer with two degrees of rotation with respect to the incident beam. The angular resolution of the tilt angle is $<0.025^{o}$ and for the azimuthal angle is $<1^{o}$. The target is connected to a cryocooler by a flexible copper braid surrounded by a

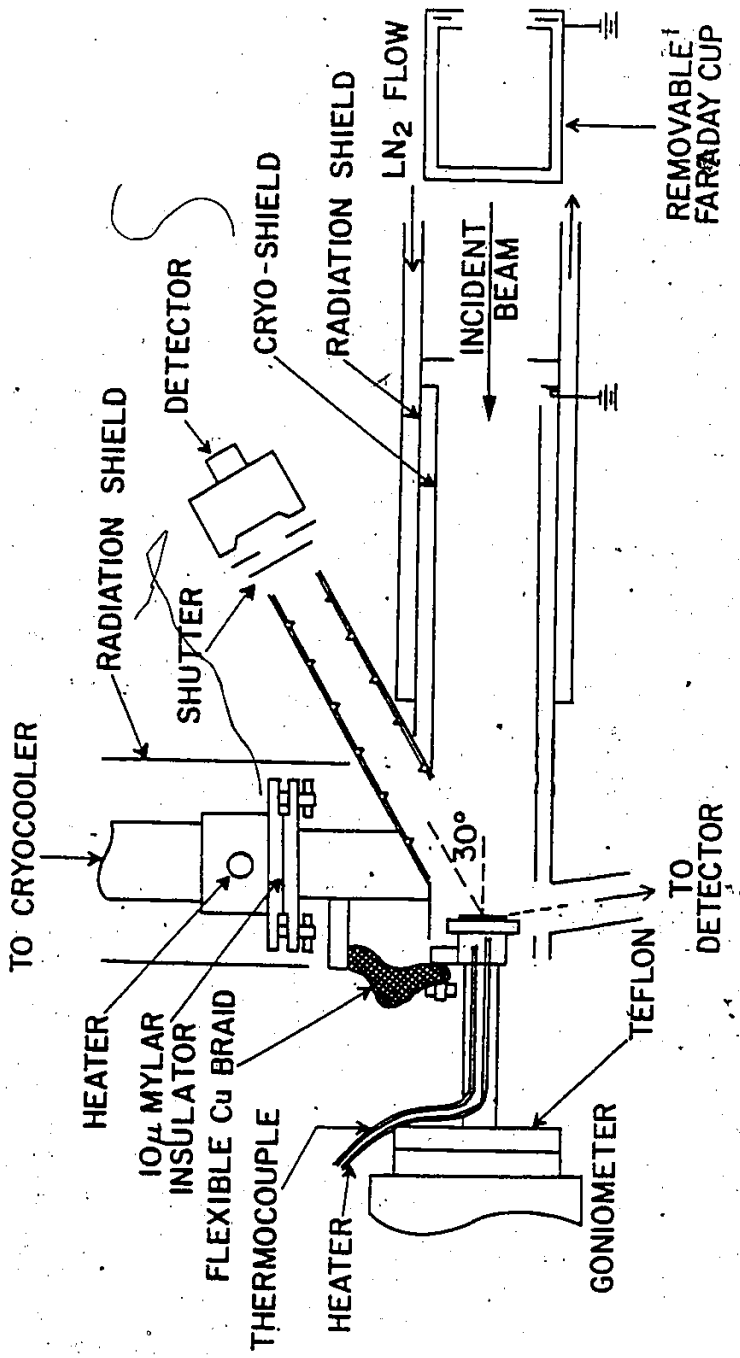

Fig. 5.2 Schematic of the target chamber

copper inner shield which is also connected to the cryocooler. When implantation and analyses were done at 300 K, the shield surrounding the target was still cooled to 50 K. The inner shield and the target are electrically isolated from the cryocooler by a 10 μm Mylar film. Another shield directly cooled by liquid nitrogen enclosed the greater part of the inner shield. The inner cold shield acts to reduce the effective pressure in the vicinity of the target to $<10^{-10}$ Torr since the partial pressure of all gases except H_2, He and Ne is $<10^{-10}$ Torr.

To avoid loss of secondary electrons from the target, a suppression voltage of -220 V was applied to two metal rings which were mounted on teflon rings placed inside the inner shield, in the front and rear end of the inner shield. Integration of the total incident current on target was made by summing the target and shield currents. A removable Faraday cup is located at the entrance of the target chamber for initial beam set-up and to check the effectiveness of the electron suppression on the target.

In the damage analysis, the backscattered He^+ particles are detected by two silicon surface barrier detectors (FWHM ≈ 15 keV) at scattering angles of 100^o and either 150^o or 160^o. Radiation damage of the detectors during implantation of the sample is avoided by externally controlled shutters which cover them. Fig. 5.3 shows a block diagram of the data aquisition system. A current integrator (Ortec model 439) measures the beam current on the target or on the Faraday cup. A timer/scaler (Ortec model 771) is used as a control unit for the data aqui-

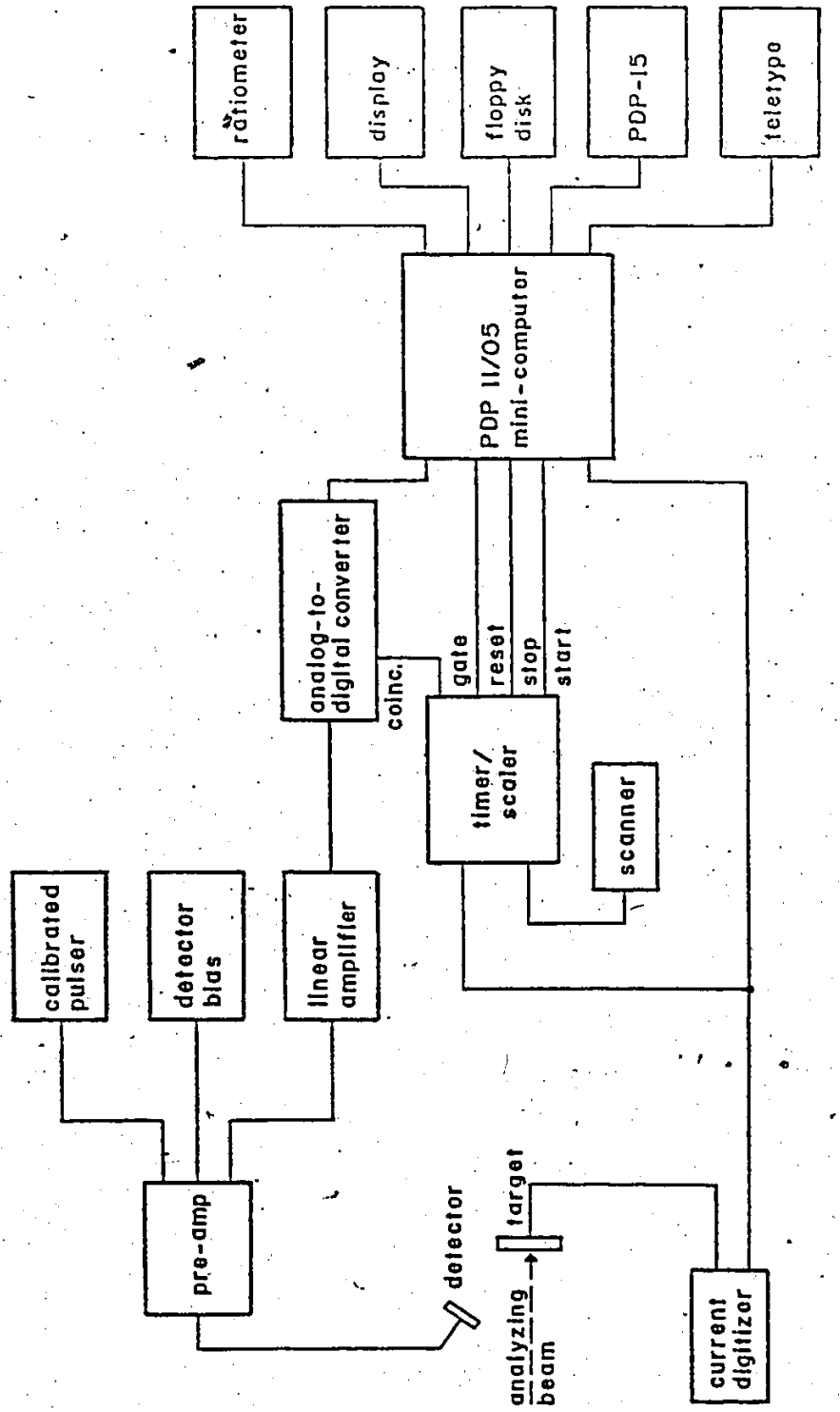

Fig. 5.3 « Block diagram of the data acquisition system

sition. It is normally preset to stop counting after the digitizer output reaches a preset total charge, and simultaneously it stops the pulse height analyser (PHA) by turning off the analog to digital converter (ADC) via a gate (Ortec model 426).

The backscattered He particles which reach the detectors produce a signal (pulse) which is proportional to the energy. This pulse passes through a pre-amplifier (Canberra model 1408), and a linear amplifier (Ortec model 572). The signal is digitized using a Northern Scientific (model 8192) ADC. The ADC is connected to a PDP 11/05 computer, programmed for pulse height analysis data acquisition. Another similar set of electronics and an ADC (Tracor Northern model TN 1314) are used for data aquisition for the other scattering geometry (100^{o}).

5.2.3. Surface Preparation and Alignment Procedure for Axial Channeling of CdS Crystals

The single crystals of cadmium sulphide (5x5x2 mm) used throughout this work were purchased from Cleveland Crystal Inc. These crystals were annealed in a sulphur ambient to ensure stoichiometry after growth. Some crystals were cut parallel to the c-axis while others were cut perpendicular to the c-axis. The crystals were re-used after removing the previous implantation damage by polishing with a 0.3 μm alumina slurry with water on a DP cloth [Struers Scientific Instruments]. The final polish was done by chemical lapping with a 50% dilute solution of HCl on an acid resistant pellon cloth [PAN-W Struers Scientific

Instruments] for few minutes.

The crystal quality and surface polish was inferred from the backscattering/channeling technique by considering the measured values of χ_{min}. The value of χ_{min} theoretically attainable was calculated from equation (4.26); with $\rho^2_{rms} = 0$, χ_{min} is 0.007. The measured value of χ_{min} determined from RBS with 2.0 MeV He^+ at 300 K was ≈.0.04 while at 50 K it was ≈ 0.015. The presence of lattice strain, defects, surface contamination and experimental beam divergence will all contribute to an increase in χ_{min}.

CdS crystals were aligned either parallel to the c- or the a-axis by the method proposed by Andersen et al. [1967]. The basic operation is to observe the backscattered yield at the detector as a function of the angle between the beam and the sample (azimuthal and tilt angles). When the beam is incident within the (small) critical angle for channeling along a low index crystallographic plane or axis, a dramatic reduction in the yield will result. In practice, the crystal was tilted approximately 6^o from normal to the beam and rotated to find yield decreases as major planes become parallel to the beam. Keeping the same planar dip the crystal was tilted to 8^o and the corresponding azimuthal angle was found. In this way several pairs of tilt and azimuthal angles corresponding to various planar dips, could be found. Then, the angular conditions for the planar dips were plotted on a standard stereogram. The intersection of the lines drawn through each pair of points corresponding to the same plane gives the major axial

direction. The unit cell of the CdS crystal structure is hexagonal and consequently there are six major planes in the direction of the c-axis and the a-axis (refer to Fig. 2.1). Hence six major planar dips could be obtained.

5.2.4. Calclulation of RBS and Channeling Parameters

i) The Kinematic Scattering Factor (K)

During the course of this work, three scattering angle geometries were used, namely 100^{o}, 150^{o} and 160^{o}. The kinematic factors for these angles were calculated using equation (4.16) and is reported in Table 5.1.

Table 5.1

The kinematic scattering factor (K) for Cd and S for the three scattering geometries (^{4}He as projectile).

	Scattering angle		
	100^{o}	150^{o}	160^{o}
K_{Cd}	0.9199	0.8756	0.8710
K_{S}	0.7447	0.6259	0.6144

ii) Stopping Cross-section for Helium in CdS

The semi-empirical values for the stopping cross section ε (in electron volts per 10^{15} atoms.cm^2) for He as given by Ziegler and Chu [1974] were used in this work. These values are approximately 10% lower than the values experimentally obtained by Hutchby et al. [1972] for helium in amorphous cadmium sulphide in the energy range 0.25-3 MeV. For compound semiconductors, the Bragg additivity rule (ref. Sec. 4.2.2) has been applied to determine the total stopping power. The average stopping powers are listed in Table 5.2 for the beam energies used in this work.

iii) Energy to Depth Conversion

Accurate conversion of the energy scale into a depth scale requires the knowledge of the stopping power of the sample for a beam in a non-aligned direction, and in a channeling direction, for undamaged and damaged crystals. Since experimental values for stopping power in the channeling direction are not available in the literature, the stopping powers in a non-aligned direction for $^4He^+$ at different energies are used in the energy to depth conversion. For the three scattering angles (100^o, 150^o, and 160^o) the energy to depth conversion (scaling factor F) was calculated by taking the molecular density of CdS to be 2.01×10^{22} molecules.cm^{-3}.

Table 5.2

Calculated stopping power for CdS for different He^+ beam energies for the three scattering angle geometries.

Energy E_o (MeV)	Stopping Power $S_{Av.}$ ($eV.10^{-15}$ atoms.cm^{-2}) scattering angle			Scaling factor F(eV/nm) scattering angle		
	100^o	150^o	160^o	100^o	150^o	160^o
1.0	1325	399.6	381	26.6	8.0	7.7
1.6	1204	362.5	345	24.2	7.3	6.9
2.0	1117	343.3	326	22.5	6.9	6.6
2.4	1038	319.5	304	20.9	6.4	6.1
2.8	906	301.5	287	19.4	6.1	5.8

iv) Analysing Beam Energy Calibration

The incident energy of the beam was calculated from the channel of the cadmium edge of the non-aligned spectrum, and a knowledge of the gain of the ADC (keV/channel) and accounting for the dead layer loss in the silicon surface barrier detecter (≈ 30 keV). The gain of the ADC is calculated by acquiring a spectrum using a precalibrated pulser (Ortec model 812) at various known energies. The pulser was initially calibrated with respect to the given detection system and associated electronics. This was done by acquiring a spectrum of alpha particles of known energies 5.486 MeV, 5.443 MeV and 5.389 MeV emitted from an ^{241}Am source and normalizing the pulser output to match these emitted energies.

v) Detector Geometry Calibration

The solid angle subtended by the detector to the center of the target can be measured geometrically and cross checked by RBS analysis using either a thin film of a heavy atomic mass element, of known thickness deposited on a lighter atomic mass substrate or a known concentration of heavy mass atoms implanted into a lighter mass substrate.

In the present investigation, the solid angle, Ω, was confirmed by taking a RBS analysis of a silicon standard implanted with $1x10^{15}$ $Bi.cm^{-2}$ at Chalk River Nuclear Laboratories [CRNL].

The RBS analysis of the sample gave an isolated peak on high energy end of the spectrum. The total number of counts in the peak is given by

$$\text{Yield} = (Nt)\ Q\ (d\sigma/d\Omega)\ \Omega \qquad (5.1)$$

where Nt is the number of Bi atoms.cm^{-2}

Q is the total number He ions incident on the target

$d\sigma/d\Omega$ is the differential scattering cross-section for He on silicon

The solid angles of the 160^{0} and 100^{0} detectors were determined to be 2.61×10^{-3} sr. and 2.11×10^{-3} sr. respectively.

vi) Implant Dose Determination

The implant dose was determined by measuring the integrated charge on the target over the time of implant and knowing the area of the implant. The area of the implant was calibrated by implanting a dose of bismuth into a silicon crystal, analysing it by RBS to determine the dose using equation 5.1., with the calibrated detector geometry. The radiation damage in the silicon crystal produced by the bismuth implant changes the surface colour and allows the area to also be measured geometrically to confirm the calculated implant area.

CHAPTER 6

RESULTS AND DISCUSSION

Introduction: This chapter is divided into three major sections. In Sec. 6.1, the results obtained from TEM studies of ion implantation damage produced in CdS crystals are presented. Sec. 6.2. gives the results from the RBS/channeling studies of the lattice disorder produced by the implantation of various doses at 50 K and 300 K, analysed either along the c-axis or along the a-axis. Finally, in Sec. 6.3, results of the TEM and backscattering experiments are correlated.

6.1. TEM

The TEM results are divided into four sections: in Sec. 6.1.1. the implantation induced defects are characterized and the dose dependence of defect production is presented; in Sec. 6.1.2. a comparison is made of defects produced by different ion species; in Sec. 6.1.3. observations are presented for samples implanted at 50 K and annealed for 20 hr. at 300 K; and in the last Sec. 6.1.4. an attempt is made to identify the type of dislocation loops.

6.1.1. Damage Characterization and Damage Dependence on Implant Dose

To study the effects of ion dose on the size and concentration of defects, the samples were implanted at 300 K with 60 keV Ar^+ ions to doses of $5x10^{14}$ ions.cm^{-2} and $2x10^{15}$ ions.cm^{-2}. In another experiment samples were implanted at 300 K with 60 keV Bi, to doses of $1x10^{14}$, $1x10^{15}$ and $2x10^{15}$ ions.cm^{-2}.

Figs. 6.1 (a) and (b) show the bright field electron micrographs in the quasi-two beam condition (0002 and $\bar{2}110$ reflections respectively) from a sample implanted to a dose of $5x10^{14}$ Ar^+.cm^{-2}. The corresponding selected area diffraction patterns are inset. Fig. 6.1 (a) shows mostly black dot contrast, however near the edge of the sample black/white dot contrast (indicated by the arrows) is observed. This type of contrast generally results from either very fine precipitates or voids, or possibly from dislocation loops with very small diameters. The possibility of voids and precipitates was ruled out by tilting experiments, confirming the observed contrast to be due to dislocation loops [Hirsch et al. (1970)].

Fig. 6.1 (b) also reveals black dot contrast indicating the presence of small loops; as well, large loops are seen. The number density of loops in Fig. 6.1 (a) is $9x10^{15}$ cm^{-3}, whereas that in Fig. 6.1 (b) is measured as $3.5x10^{16}$ cm^{-3}. The sample thickness used in the density calculation was measured for some samples from their stereo micrographs, and found to be ≈ 60 nm. The average diameter of the loops

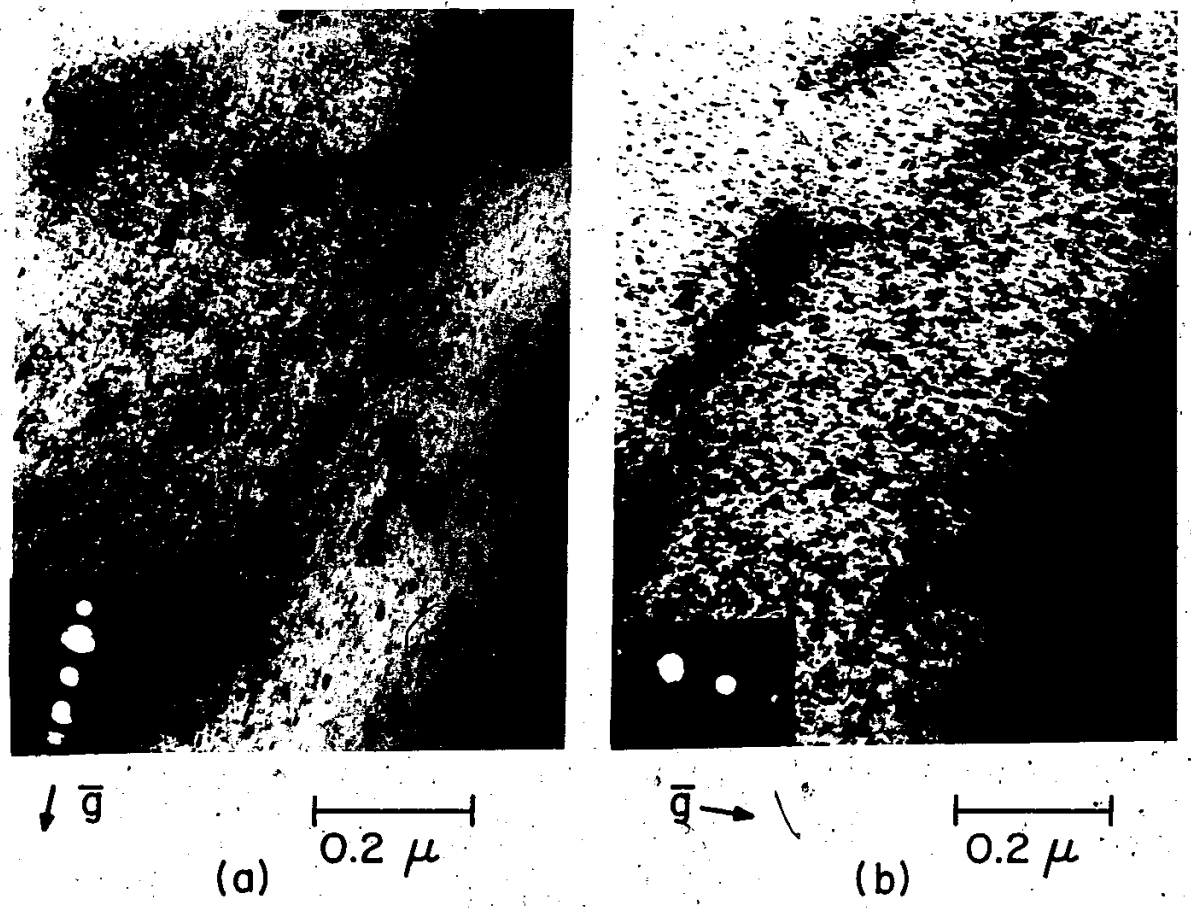

Fig. 6.1 Electron micrographs from a CdS crystal implanted with a dose of 5×10^{14} $Ar^{+} cm^{-2}$ at 300 K showing black and black/white dot contrast: (a) with $\bar{g} = 0002$; (b) with $\bar{g} = \bar{2}110$.

with the reflection $\bar{g} = 0002$ is ≈ 7 nm and that with $\bar{g} = \bar{2}110$ is ≈ 13 nm. Both micrographs were taken from the same region of the sample. Comparision of these micrographs shows that the large loops which are in contrast using $\bar{g} = \bar{2}110$ are out of contrast for $\bar{g} = 0002$. Because of the very high density of loops observed for $\bar{g} = \bar{2}110$, it was not possible to establish a one to one correspondence between the two micrographs for the dots due to small loops. However the drastic change in number density of loops shows that a large number of small loops also go out of contrast with the reflection $\bar{g} = 0002$. This means that those loops which are present in the 0002 reflecting condition have a Burgers vector along the c-axis and the loops which are present in the $\bar{2}110$ reflecting condition have a Burgers vector along the a-axis or perpendicular to the c-axis. The magnitude of the Burgers vector along the c-axis is one-half the lattice spacing along the c-axis i.e. $\bar{b} = c/2 = 1/2\ [0001]$, and the magnitude of the Burgers vector perpendicular to the c-axis is the lattice spacing along the a-axis i.e. $\bar{b} = a = 1/3\ \langle 11\bar{2}0 \rangle$ [Yoshiie et al. (1980), (1981)]. The former type of loops will hereafter be called "type I" and the latter type of loops "type II".

Fig. 6.2 is a diffraction pattern from a large region of an argon implanted sample (2×10^{15} $Ar^{+}.cm^{-2}$) showing a foil orientation of $(01\bar{1}0)$ while Fig. 6.3 shows a schematic standard diffraction pattern of a h.c.p. structure with $(01\bar{1}0)$ orientation for comparision. The diffraction pattern of Fig. 6.2 showed neither any distinguishable degradation of the pattern nor any extra spots or rings compared to the diffraction

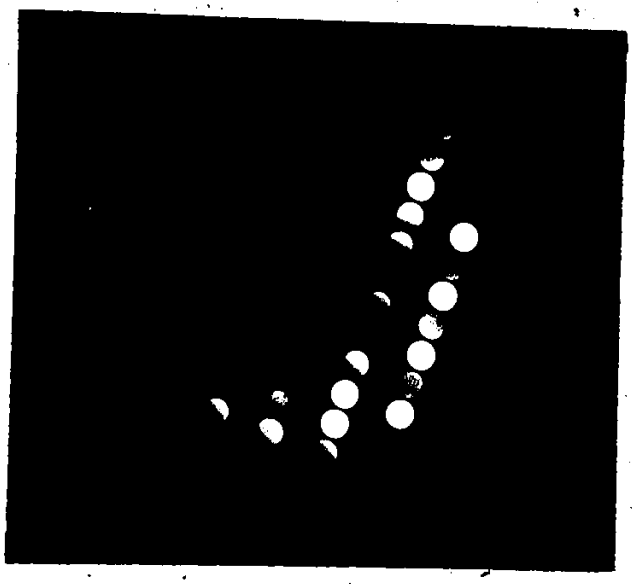

Fig. 6.2 A diffraction pattern from an argon implanted CdS crystal ($2x10^{15}$ $Ar^{+}.cm^{-2}$) in the $(01\bar{1}0)$ orientation.

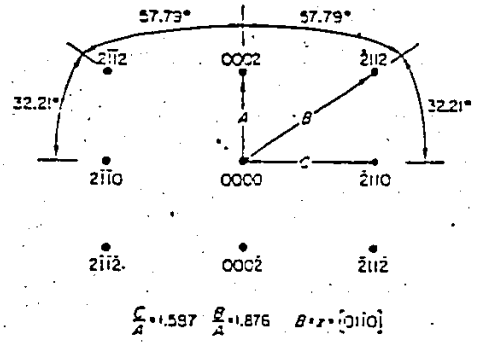

Fig. 6.3 A standard diffraction pattern for the h.c.p. structure with $(01\bar{1}0)$ orientation [Edington (1975)].

pattern of the unimplanted sample. This observed diffraction and the images for the implanted samples show that the crystal structure does not amorphize after heavy ion implantation.

Fig. 6.4 (a) and (b) are micrographs with reflections 0002 and $\bar{2}110$ respectively, from a region of a sample implanted to a dose of 2×10^{15} $Ar^{+}.cm^{-2}$, the former showing well defined circular loops. Large loops with segments which are parallel to $\bar{g}$ are out of contrast as expected theoretically for this reflection condition (see Sec. 4.3.3). Fig. 6.4 (b) shows a large density of defects in which a noticeable feature is that there are many pairs of parallel lines oriented perpendicular to $\bar{g} = \bar{2}110$. Such line contrast appears to be due to dislocation loops lying in the prism planes of type $\{11\bar{2}0\}$, which are perpendicular to the foil plane $\{01\bar{1}0\}$. Since these loops are slightly inclined to the beam direction they give contrast from the upper and lower part of the loops, which would appear as pairs of lines. This means that these loops lie in the prism planes $\{11\bar{2}0\}$ which are perpendicular to the $\bar{g} = 11\bar{2}0$. In general, the circular contrast arises due to circular loops lying in the foil plane i.e. $(01\bar{1}0)$. Circular loops which are lying in other planes will give elliptical contrast. If the dislocation loops are lying in the basal plane and have a Burgers vector along the c-axis, i.e. prismatic loops, they should give either a straight line contrast perpendicular to $\bar{g} = [0002]$ (when seen edge on), or pairs of parallel lines when inclined to the beam direction. Fig. 6.4 (a) does not show any line contrast; rather it shows well defined circular loops indicating that these loops are also lying in the foil,

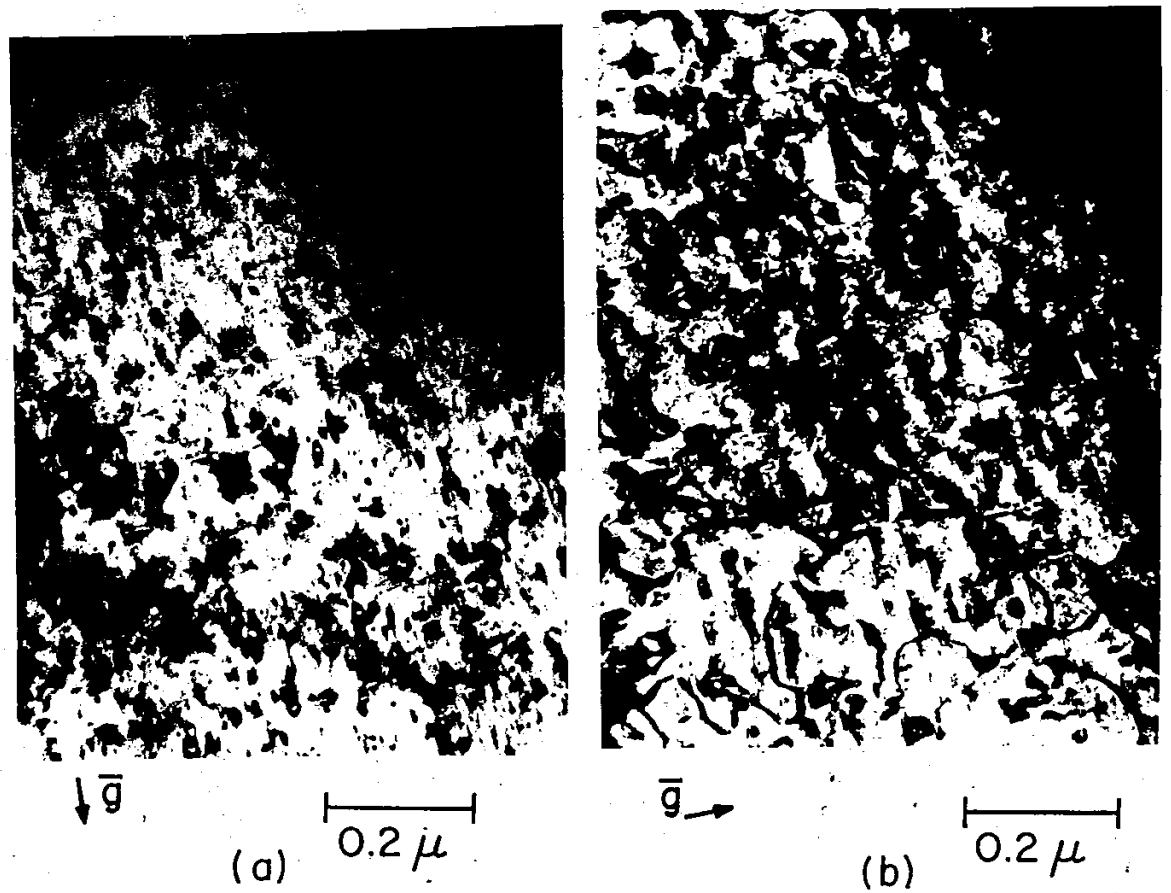

Fig. 6.4 Electron micrographs from a CdS crystal implanted with a dose of 2×10^{15} $Ar^{+}.cm^{-2}$ at 300 K showing dislocation loop contrast: (a) with $\bar{g} = 0002$; (b) with $\bar{g} = \bar{2}110$.

plane having a Burgers vector along the c-axis. If there are small prismatic loops (<2-3 nm in diameter) it would be difficult to distinguish their contrast from that for loops lying in the prism planes having a Burgers vector along the c-axis.

The next set of micrographs, Figs. 6.5 to 6.8, are taken from a sample implanted with increasing doses of 60 keV Bi^+ at 300 K. Fig. 6.5 is a micrograph corresponding to a dose of $1x10^{14}$ $Bi^+.cm^{-2}$ taken in the 0002 operating reflection. It shows loops of type I in black dot as well as black-white dot contrast. The average diameter and density of the loops are ≈ 7 nm and $2x10^{16}$ cm^{-3} respectively. The same sample was further implanted to a total dose of $1x10^{15}$ $Bi^+.cm^{-2}$ and a pair of micrographs were taken from the same region under the 0002 and $11\bar{2}0$ reflecting conditions (Figs. 6.6 (a) & (b)). The average loop size increased to a diameter of ≈ 15 nm and consequently the loop contrast changed from dot contrast to a typical double arc contrast, i.e. the diameter perpendicular to $\bar{g}$ went out of contrast as seen in Fig. 6.6(a). Fig. 6.6 (b) shows a very high density of dislocation loops of type II. However some well defined dislocation loops may be seen in the micrograph.

The same sample was further implanted to a total dose of $2x10^{15}$ $Bi^+.cm^{-2}$, and two pairs of stereo micrographs were taken from the same area under 0002 and $10\bar{1}0$ reflecting conditions, which are shown in Figs. 6.7 and 6.8 respectively. When these pairs are observed in a stereo viewer, small and large loops are seen to be distributed through-

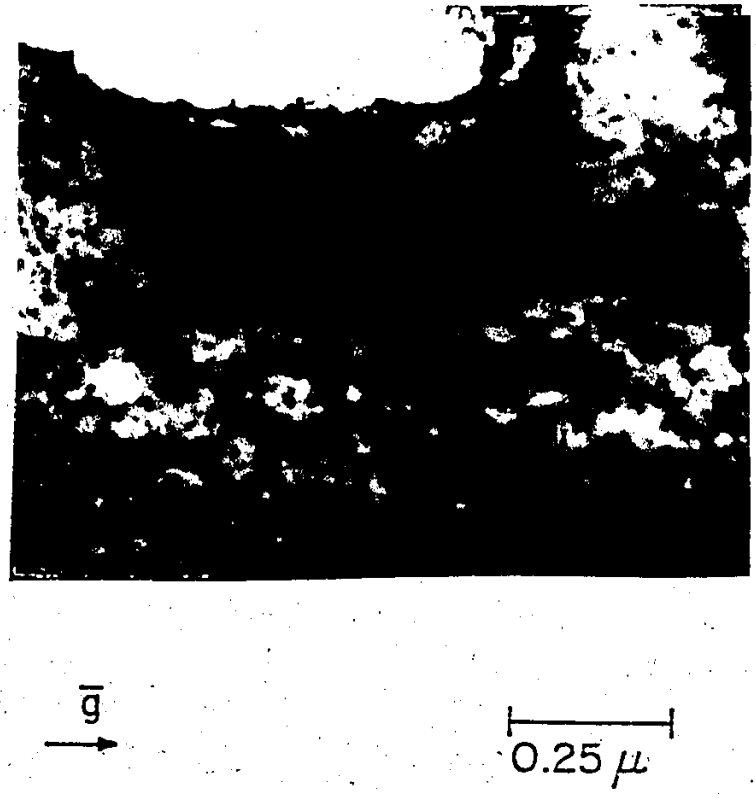

Fig. 6.5 Electron micrograph showing black dot, and white dot contrast from a CdS crystal implanted with a dose of 1×10^{14} $Bi^{+} cm^{-2}$ at 300 K.

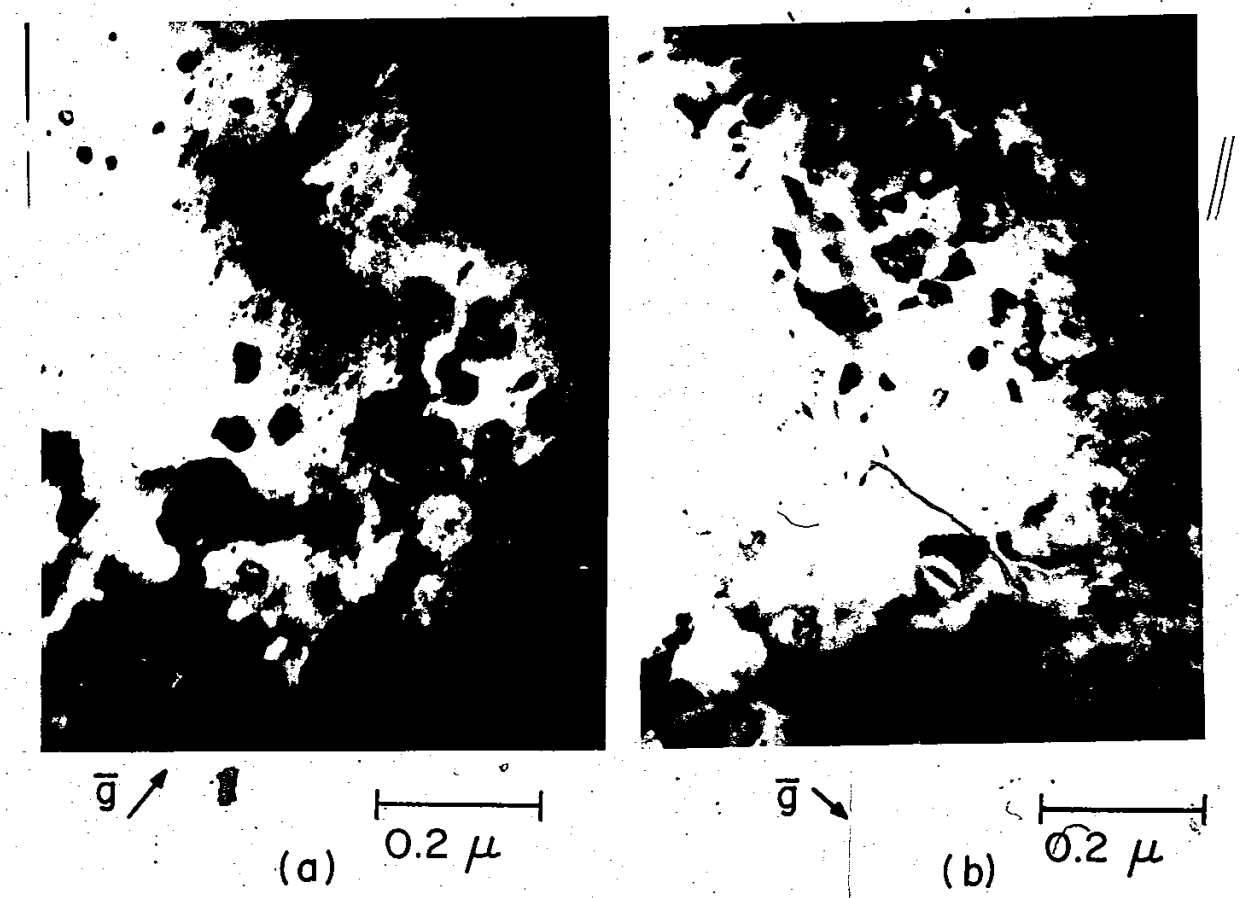

Fig. 6.6 Electron micrographs showing dislocation loop contrast from a sample implanted with a dose of 1×10^{15} $Bi^{+} cm^{-2}$ at 300 K: (a) with $\bar{g} = 0002$; (b) with $\bar{g} = \bar{2}110$.

out the depth. After identifying the upper and lower surfaces, the thickness of the sample was estimated at several places to be 60 ±10 nm.

The stereo pairs for the reflection $\bar{g}$ = 0002 (Fig. 6.7) show loops in double arc contrast. The diameter of the loop perpendicular to $\bar{g}$ is out of contrast. The same loops (marked with arrows) when observed with $\bar{g}$ = 10$\bar{1}$0 reflection (Fig. 6.8) go completely out of contrast and now appear with stacking fault contrast. These observations suggest that these loops are due to partial dislocations lying in the basal plane.

The loop diameter and the loop density dependence on implanted dose for argon and bismuth are given in Table 6.1. The loop diameter increased while loop density decreased, with increasing implant dose.

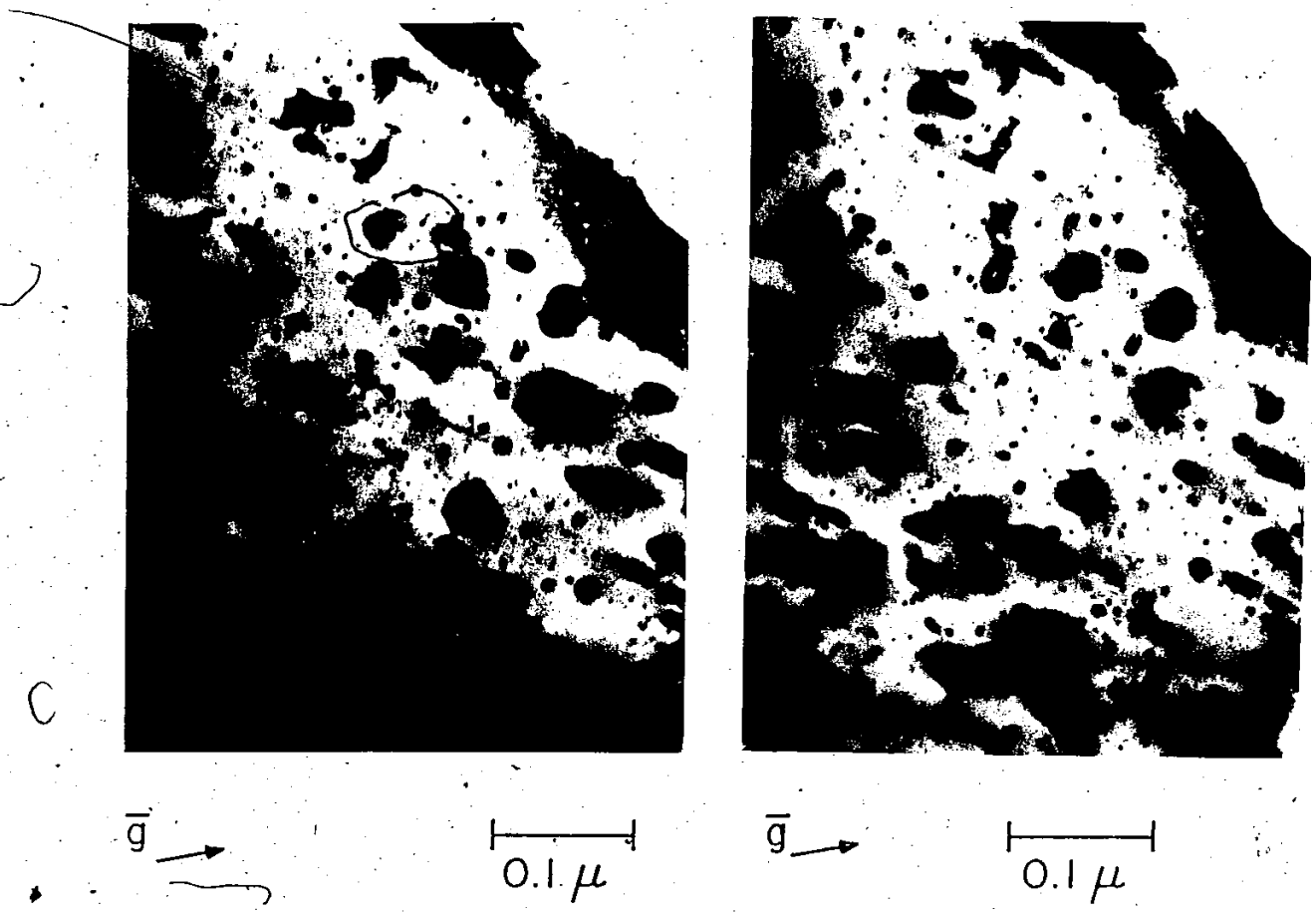

Fig. 6.7 A pair of stereo micrographs showing dislocation loops in double arc contrast from a CdS crystal implanted with a dose of 2×10^{15} $Bi^{+}.cm^{-2}$ ($\bar{g} = 0002$).

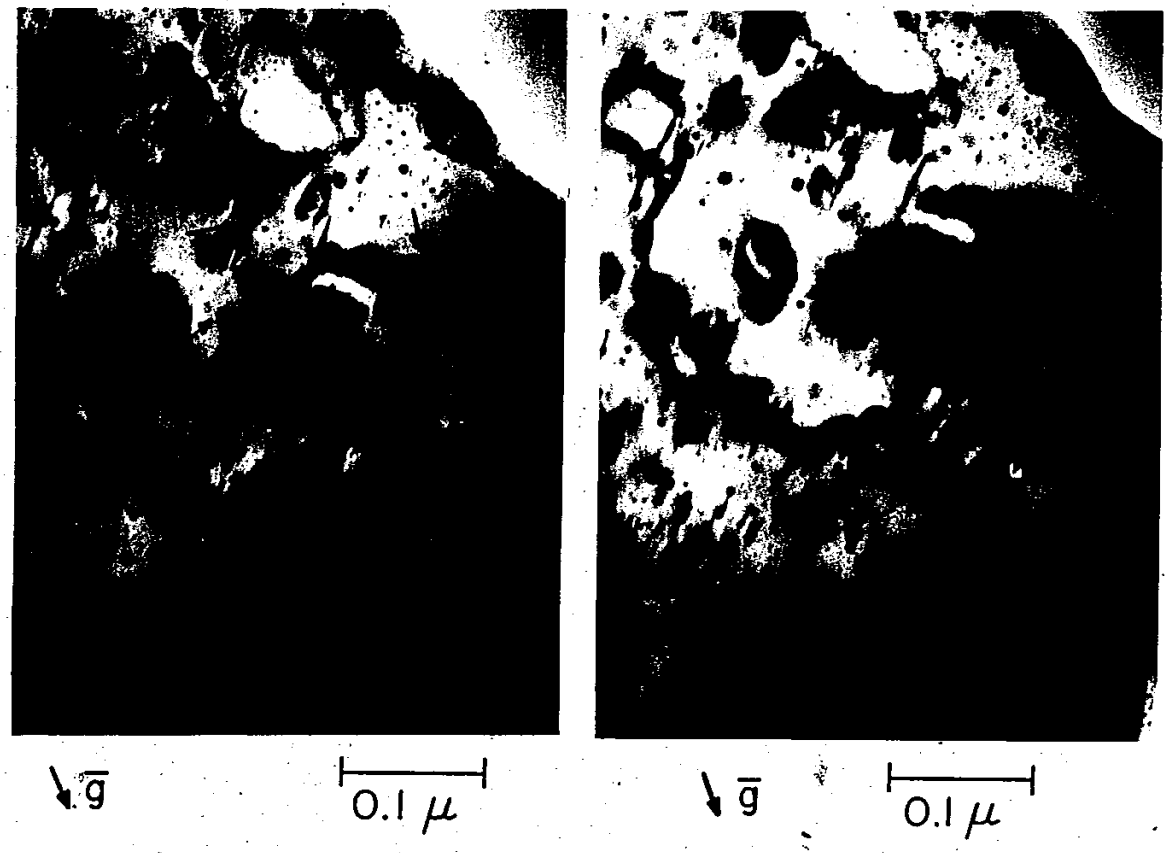

Fig. 6.8 A pair of stereo micrographs showing the dislocation loops observed in Fig. 6.7, going completely out of contrast and appearing as stacking fault fringes ($\bar{g} = \bar{2}110$).

Table 6.1

The size and density of dislocation loops as a function of implant dose.

Ion species	Dose (ions.cm^{-2})	Average Loop Diameter (nm)		Average density (cm^{-3})	
		B ∥ c	B ⊥ c	B ∥ c	B ⊥ c
60 keV Bi^+	$1x10^{14}$	7	16	$2x10^{16}$	$4.5x10^{16}$
	$1x10^{15}$	15	21	$9x10^{15}$	$2.2x10^{16}$
	$2x10^{15}$	20	25	$7x10^{15}$	$1.5x10^{16}$
60 keV Ar^+	$5x10^{14}$	7	13	$9x10^{15}$	$3.5x10^{16}$
	$2x10^{15}$	13	20	$1.3x10^{16}$	$1.2x10^{16}$

As mentioned in Sec. 5.1.2, all samples were mounted in a folded copper grid before implantation. To observe the difference between implanted and unimplanted regions, one of the implanted samples was deliberately moved slightly so that the regions covered by the grid bars were exposed to the electron beam along with the implanted region. Fig. 6.9 shows the micrograph of such a region, where implanted and unimplanted regions are seen together. The corresponding SAD patterns from each region show the same orientation as seen from the insets. The observations of this section may be summarized as follows :

(i) Bismuth and argon implantations do not amorphize the crystals but produce dislocation loops.

(ii) Generally, two types of loops are observed: type I has a Burgers vector along the c-axis, and type II has a Burgers vector perpendicular to the c axis.

(iii) The loops of type I & type II lie predominantly in the prism planes of type $1\bar{1}00$ and $11\bar{2}0$, except for high dose implants where the image contrast becomes too complicated to analyse.

(iv) The diameter and the density of loops of type II are nearly 2 to 3 times larger than those of type I loops.

(v) The diameter of the loops increases while the density of the loops decreases with increasing implant dose.

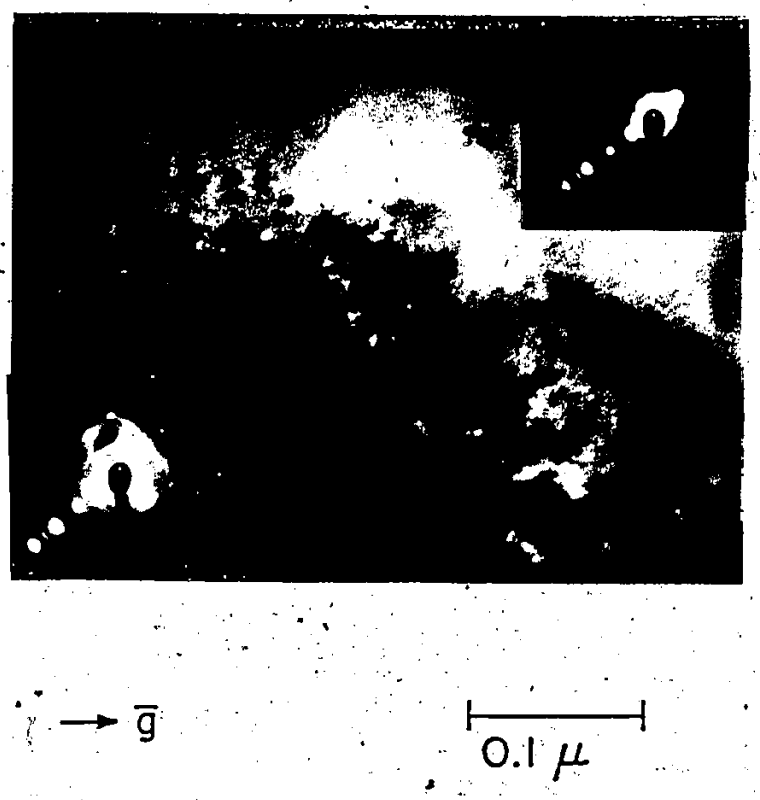

Fig. 6.9 Electron micrograph from a CdS crystal implanted with a dose of 2×10^{15} $Bi^{+}.cm^{-2}$ at 300 K showing implanted and unimplanted regions side by side.

6.1.2. Comparision of Damage Production with Elastically Deposited Energy

In this section a comparison is made of defect production by different ion species implanted to a dose of $2x10^{15}$ ions.cm^{-2}. Figs. 6.10 (a) & (b) are a pair of micrographs taken in the 0002 and 11$\bar{2}$0 reflecting conditions respectively from the same region of the sample implanted with 45 keV neon at 300 K. The contrast which appears in the 0002 reflection goes out of contrast in the 11$\bar{2}$0 reflection and vice versa. The loops of type I have an average diameter and density of $\simeq$ 8 nm and $\simeq 7x10^{14}$ cm^{-3} respectively. The loops of type II have an average diameter and density of $\simeq$ 13 nm and $1.4x10^{16}$ cm^{-3}. The type II loops are $\simeq$ 1.5 times larger in diameter and the density is nearly two times greater than those of type I.

To compare the damage production by different ion species, in effect the energy deposited into elastic collision by the ions and the range over which it is deposited, the results of the bismuth and the argon implants for the same dose ($2x10^{15}$ ions.cm^{-2}) from the previous section are used along with the results from the neon implants. Table 6.2 gives the implanted ion species, their total elastic energy deposited per ion, the ion range, the damage range, the damage stragglings, $\tilde{\theta}_\nu$ and the diameter and density of the loops of type I and type II. The $\tilde{\theta}_\nu$ for these ions were calculated using equation 3.18. In this calculation R_ν has taken from the Monte-Carlo results of Walker [1977] for Ge (equivalent to an average of Cd and S masses). Cadmium sulphide

sublimes at 980° C, at atmospheric pressure with a heat of sublimation, ΔH_{sub}, of 51 kCal/mole (≈ 2.2 eV/atom) [Abrikosov (1969)]. The energy required to raise the temperature from 25° C to 980° C is ≈ 0.25 eV/atom [Abrikosov (1969)] which is a small fraction of the sublimation energy. It is necessary to mention that sublimation is a surface phenomenon where atoms are bonded by half the number of bonds compared to the atoms which are in the bulk of the material.

From Table 6.2 it can be seen that $\tilde{\Theta}_\nu$ for Bi is approximately equal to the total heat required to sublime CdS from 25° C while for Ar and Ne ions the $\tilde{\Theta}_\nu$ values are ≈ 0.4 and ≈ 0.2 ΔH_{sub}. The dislocation loops produced by Bi implantation have an average diameter of ≈ 25 nm which is approximately equal to the damage range plus two standard deviations (longitudinal stragglings) indicating that Bi ions create collision cascades which cover the whole volume defined by the longitudinal and transverse straggling. For Ar and Ne implants the damage range is much deeper than the size of the loops indicating that these ions produce subcascades.

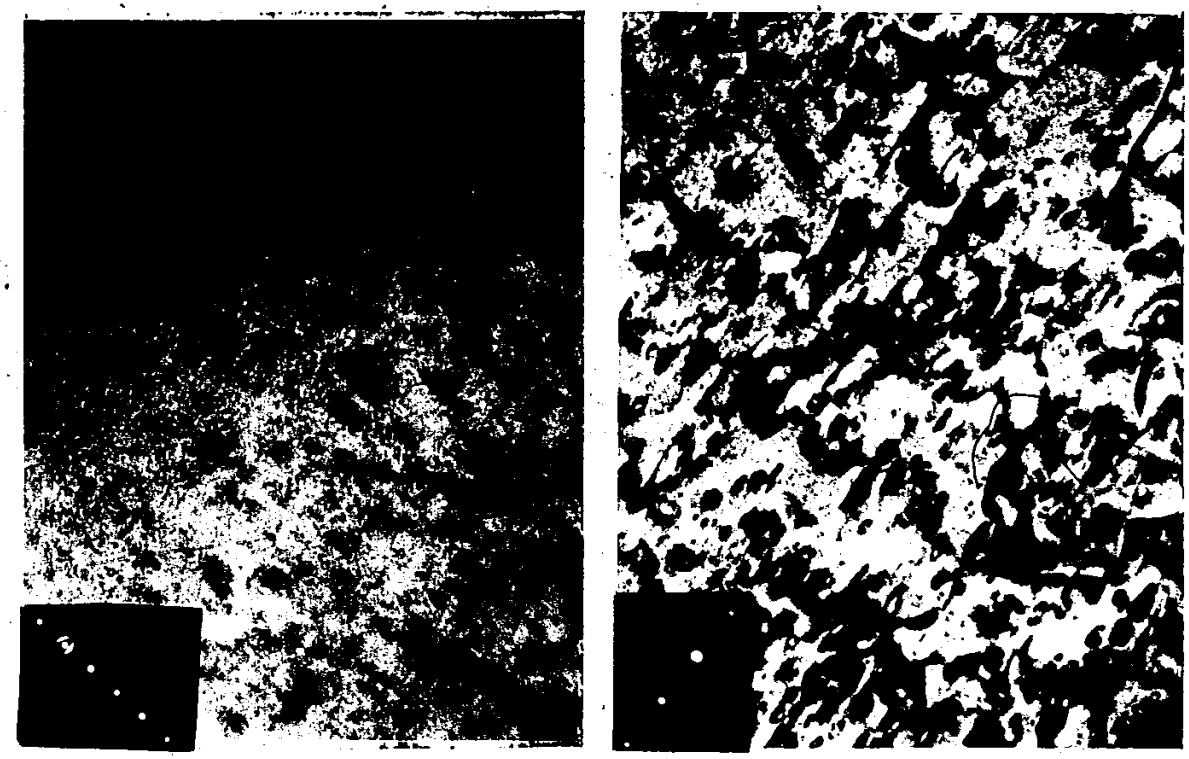

Fig. 6.10 Electron micrographs from a CdS crystal implanted with a dose of 2×10^{15} $Ne^{+}.cm^{-2}$ at 300 K: (a) with $\bar{g} = 0002$; (b) with $\bar{g} = 11\bar{2}0$.

Table 6.2

The size and density of dislocation loops as a function of energy deposited into elastic collisions.

Ion Species	Dose (ions.cm^{-2})	Ion Range R_p (nm)	Elastic Energy Deposited (keV)	Damage Range (nm)	Damage Straggling $\langle \Delta X^2 \rangle^{1/2}$ (nm)	Damage Straggling $\langle Y^2 \rangle^{1/2}$ (nm)	R_v	$\tilde{\theta}_v$ (eV/atom)	Average Loop Diameter (nm) $\vec{b} \parallel c$	Average Loop Diameter (nm) $\vec{b} \perp c$	Average Loop Density (cm^{-3}) $\vec{b} \parallel c$	Average Loop Density (cm^{-3}) $\vec{b} \perp c$
60 keV Bi^+	2×10^{15}	18	43.7	13.0	4.6	3.0	0.8	2.4	20	25	7×10^{15}	1.5×10^{16}
60 keV Ar^+	2×10^{15}	44	37.3	34.0	7.4	5.0	0.6	1.0	13	20	1.3×10^{16}	1.2×10^{16}
45 keV Ne^+	2×10^{15}	59	23.6	46.0	13.0	9.4	0.4	0.58	8	13	7×10^{15}	1.4×10^{16}

6.1.3. Possible Annealing at 300 K

In this section the TEM observations of samples implanted at 50 K and annealed at 300 K are presented. The samples were implanted at 50 K with 60 keV Bi^+ ions at doses of $2x10^{14}$ and $2x10^{15}$ Bi^+cm^{-2}. After implantation the samples were warmed to room temperature over a period of about an hour and immediately recooled down to liquid nitrogen temperature (77 K) for storage. After a few days, the samples were again warmed up to room temperature and were vacuum dried in a desiccator for about half an hour before observing them in the microscope. During the TEM observations the samples were cooled to liquid nitrogen temperature. A series of micrographs were taken from various regions of the samples in the 0002 and $11\bar{2}0$ reflecting conditions. After the TEM observations the samples were warmed to room temperature and were kept at this temperature for about 20 hours. The samples were observed again after this annealing period and a series of micrographs were taken for 0002 and $11\bar{2}0$ reflecting conditions.

Figs. 6.11 (a) & (b) are micrographs from the same region of the sample implanted at 50 K to a dose of $2x10^{15}$ $Bi^+.cm^{-2}$ in the 0002 and $11\bar{2}0$ reflecting conditions respectively. Fig. 6.11 (a) shows large circular loops with an average diameter of ≈ 13 nm and small black dot contrast with an average diameter of ≈ 5nm. The average density of loops in reflection (0002) is ≈ $1.4x10^{16}$ cm^{-3}. Fig 6.11 (b) shows a highly strained region of complicated contrast indicating a very high density of defects. This complicated contrast feature which appears

in the $11\bar{2}0$ reflection goes out of contrast for $\bar{g} = 0002$. However, because of the high density of defects for the reflection $\bar{g} = 11\bar{2}0$, it is difficult to determine whether the loops with $\bar{g} = 0002$ go out of contrast in the reflection $\bar{g} = 11\bar{2}0$. The same sample shows an extremely high density of defects when photographed in the $\bar{g} = 11\bar{2}0$ reflection condition (Fig.6.11(b)) compared to that obtained in the $\bar{g} = 0002$ reflection condition (Fig. 6.11(a)). This is because most of the loops in Fig. 6.11 (b) have their Burgers vector perpendicular to the c-axis and go out of contrast in Fig. 6.11 (a). Loops in Fig. 6.11 (a) have their Burgers vector along the c-axis.

When the sample was kept at 300 K for 20 hr. most of the damage annealed out, as shown in Fig. 6.12 (a) and (b). Fig. 6.12 (a) shows some loops in the dot contrast with considerably reduced number density. The average diameter of the loops in the reflection (0002) is $\approx$ 7 nm, which is approximately half the size of the loops observed before annealing. The density of the loops also decreased by an order of magnitude from 1.4×10^{16} cm^{-3} to 1.8×10^{15} cm^{-3} after the annealing period. The dramatic effect of annealing is seen in Fig. 6.12 (b), where most of the defects have annealed out and only a few well defined dislocation loops remained. The average diameter and density of the loops in Fig. 6.12 (b) are $\approx$ 40 nm and $< 1 \times 10^{15}$ cm^{-3}. Many of the loops with circular contrast are lying in the foil plane $\{1\bar{1}00\}$, with their Burgers vector along the a-axis. There is also extended line contrast perpendicular to $\bar{g} = 11\bar{2}0$ which arise from loops whose dislocation lines intersect the foil surfaces.

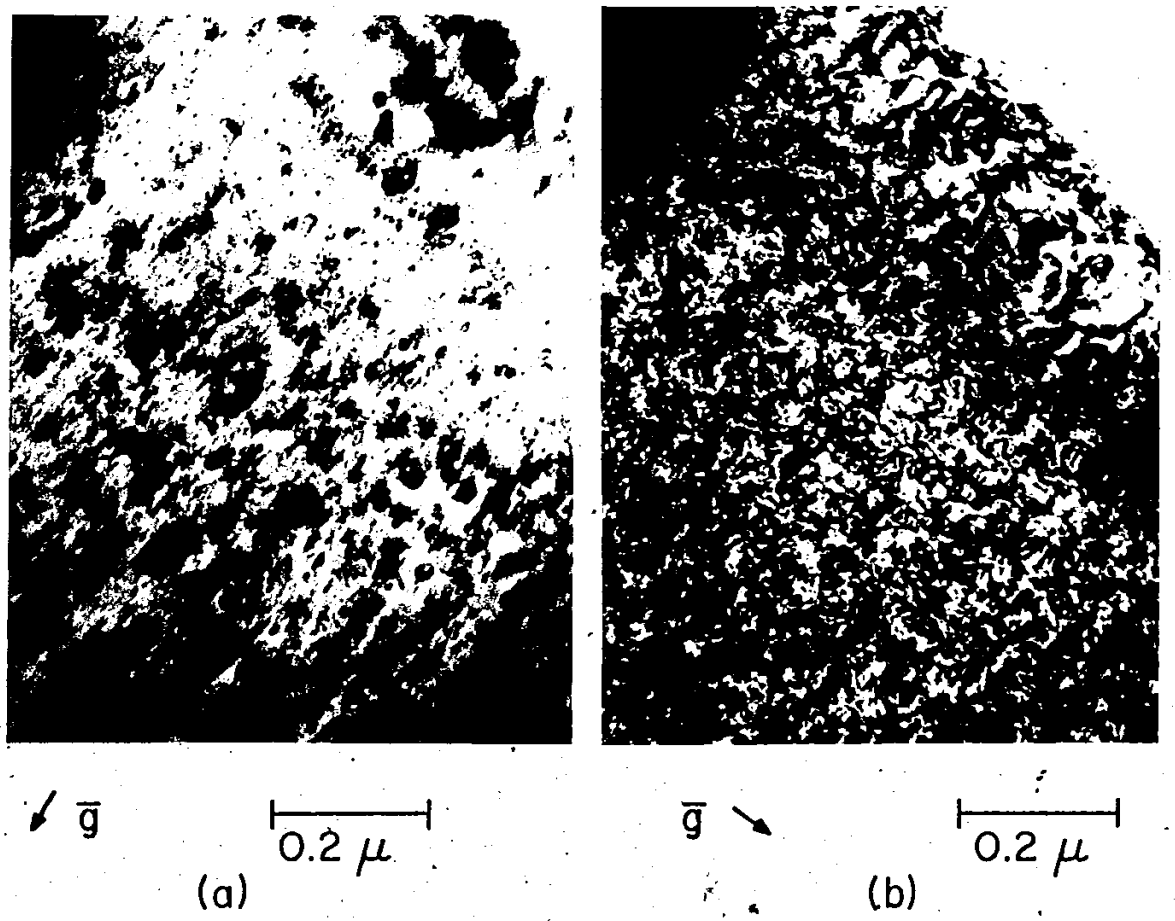

Fig. 6.11 Electron micrographs from a CdS crystal implanted with a dose of 2×10^{15} $Bi^{+}.cm^{-2}$ at 50 K: (a) with $\bar{g} = 0002$; (b) with $\bar{g} = 11\bar{2}0$.

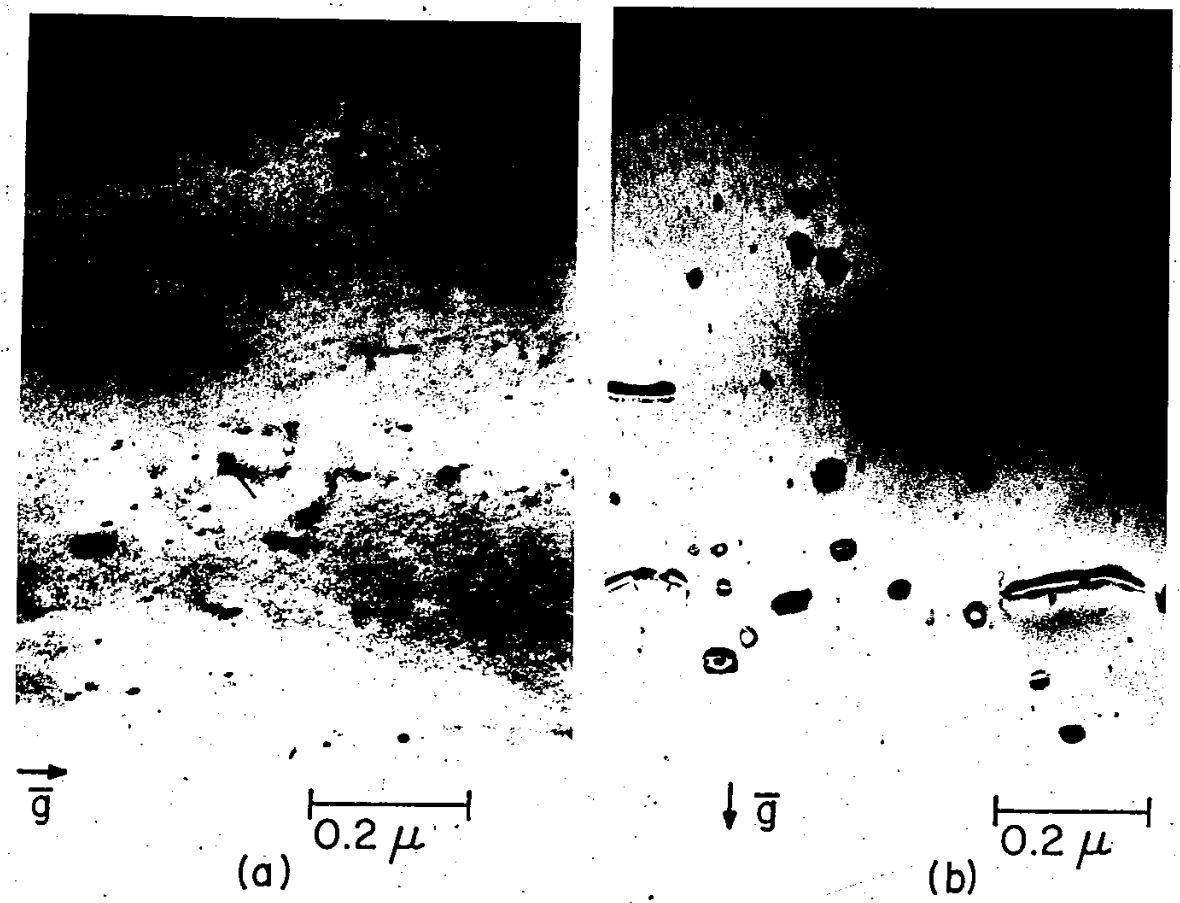

Fig. 6.12 Electron micrographs form the sample of Fig. 6.11 after keeping it at 300 K for 20 hr. showing the dramatic annealing of dislocation loops: (a) with $\bar{g}$ = 0002; (b) with $\bar{g}$ = $\bar{2}$110.

The sample which was implanted to a dose of $2x10^{14}$ Bi.cm^{-2} at 50 K showed black dot contrast when $\bar{g}$ = 0002 (Fig. 6.13 (a)) and black dots plus extended line contrast when $\bar{g}$ = 11$\bar{2}$0 (Fig. 6.13 (b)). After keeping the sample at 300 K for 20 hr. the image contrast did not change much (Fig. 6.14 (a) and (b)). The majority of black extended lines are perpendicular to the $\bar{g}$ = 11$\bar{2}$0. This contrast may be due to the loops lying in the prism plane having a Burgers vector in the a-direction.

The annealing of the damage by warming the high dose implanted sample to 300 K may be due to the large strain energy stored in the sample, which provides sufficient driving force for the defects to anneal. For higher doses, the average separation between the collision cascades decreases, hence the defects are closer together, and can interact strongly. When dislocations of opposite sign come close together they attract each other and annihilate to reduce their total strain energy [Hull (1978)].

The damage produced by 50 K implants is different from that produced at 300 K. The damage produced by the dose of $2x10^{14}$ Bi.cm^{-2} at 50 K is characterized by extended line contrast, whereas there is black dot/loop contrast in the sample implanted at 300 K. At the higher dose the low temperature implants show higher damage than the samples implanted at 300 K.

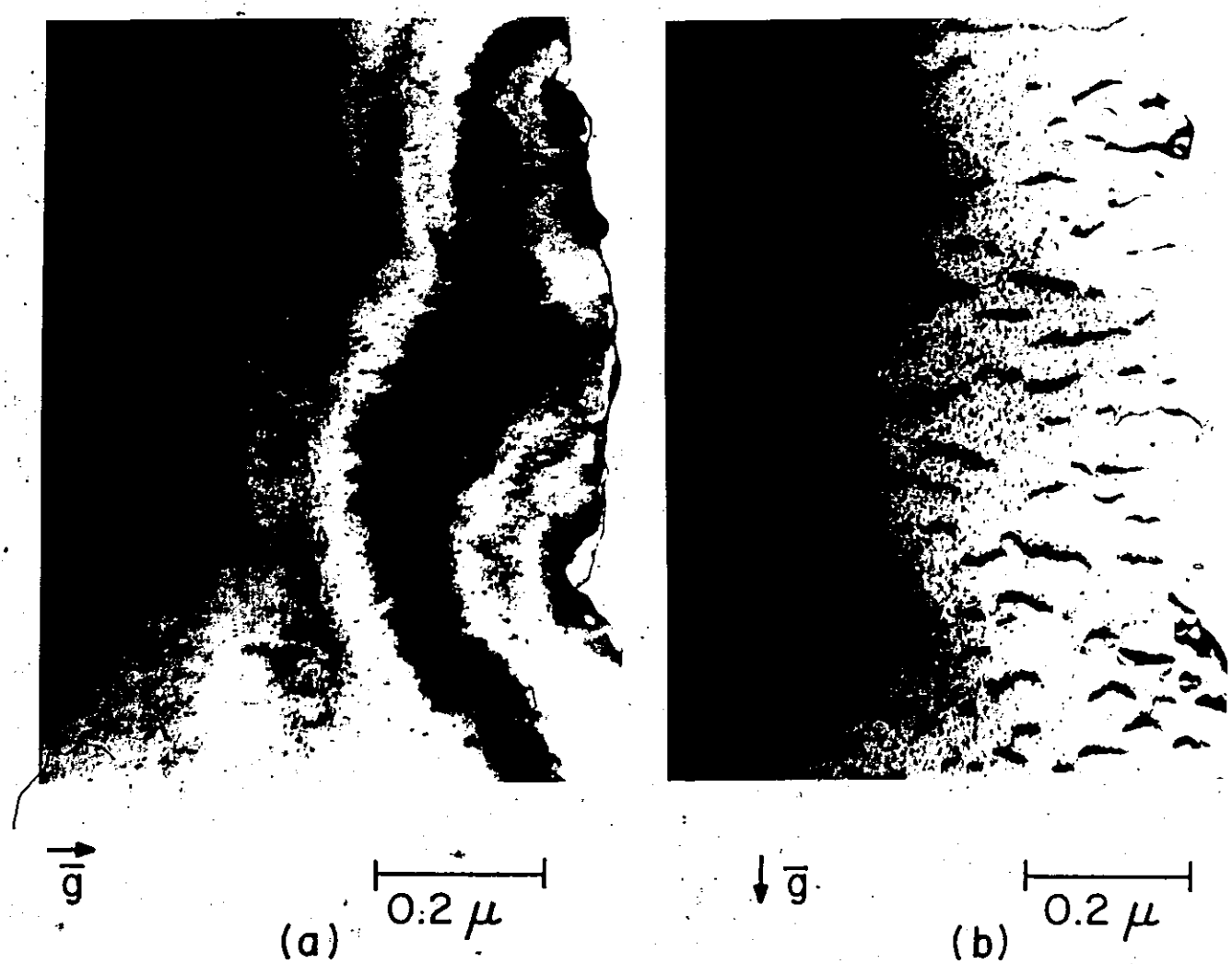

Fig. 6.13 Electron micrographs from a CdS crystal implanted with a dose of 2×10^{14} $Bi^{+}.cm^{-2}$ at 50 K: (a) with $\bar{g} = 0002$; (b) with $\bar{g} = \bar{2}110$.

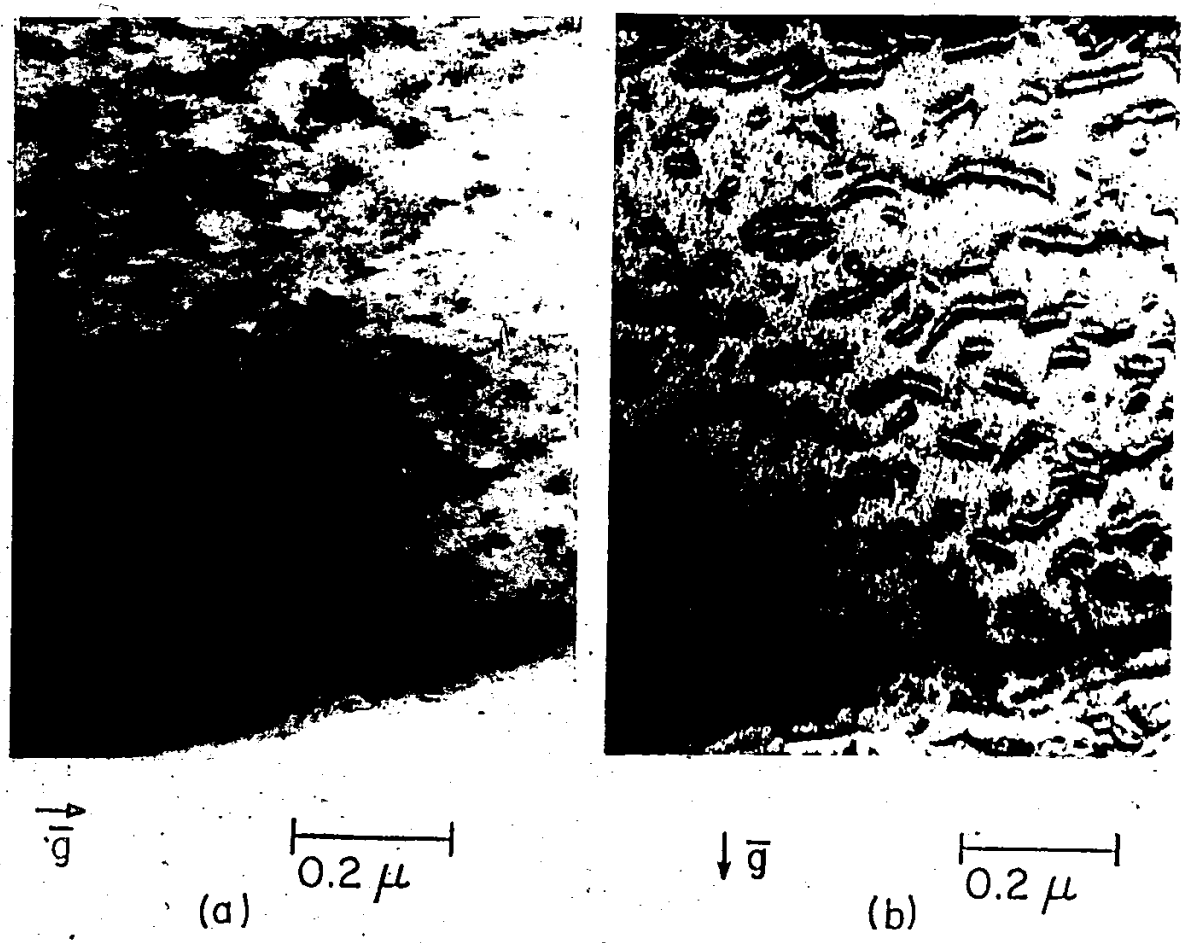

Fig. 6.14 Electron micrographs from the sample of Fig. 6.13 after keeping it at 300 K for 20 hr.: (a) with $\bar{g}$ = 0.002; (b) $\bar{g} = 11\bar{2}0$.

It is known that in CdS the sulphur and cadmium interstitials become mobile at 170 K and 230 K respectively [Elsby (1971)]. Therefore the lower damage observed for implantation at 300 K may be understood in terms of defect migration and annealing occurring simultaneously at this temperature. On the contrary, for implantation at 50 K all the defects are frozen-in and thus at this temperature the density of the defects is expected to be higher than that for implantation at 300 K, as observed.

To summarize the observations of this section the following points are noted:

i) The majority of defects produced at 50 K with $2x10^{15}$ $Bi.cm^{-2}$ have a Burgers vector along the a-axis.

ii) The sample implanted at 50 K to a dose of $2x10^{14}$ $Bi.cm^{-2}$ showed extended line contrast, while there was black dot contrast for the sample implanted at 300 K for the reflection $\bar{g} = 11\bar{2}0$. The sample implanted to $2x10^{15}$ $Bi.cm^{-2}$ at 50 K shows higher damage than the sample implanted at 300 K to the same dose.

iii) The sample implanted to a dose of $2x10^{15}$ $Bi.cm^{-2}$ showed large annealing of defects when it was left at 300 K for about 20 hr., whereas the sample implanted to a dose of $2x10^{14}$ $Bi.cm^{-2}$ did not show any visible annealing.

iv) The amount of damage produced by the bismuth implantation at 50 K is different than that produced at 300 K.

6.1.4. Characterization of Dislocation Loops

Attempts were made to determine the nature of the dislocation loops (i.e. vacancy or interstitial) produced by $2x10^{15}$ $Ar.cm^{-2}$ implanted into CdS crystals. To do this a pair of stereo micrographs (Fig. 6.15) and a pair of micrographs with $\pm \bar{g}$ condition (Fig. 6.16 (a) and (b)) were taken from the same region of the sample.

Those loops which are numbered on both sets of micrographs were analysed. The orientation of the loops was found by observing the pair of stereo micrographs in a stereo viewer. From the pair of $\pm \bar{g}$ micrographs, the change in loop contrast (inside/outside) was recorded. The type of loop was determined by knowing the orientation of each loop and following changes in its contrast features between $\pm \bar{g}$ conditions as explained in Sec. 4.1.3.

There are several problems associated with these measurements:

i) The specimens are sensitive to the probing electron beam which with time affects the quality of the image. Also, dislocation rearrangment occurred between successive electron beam exposures. For example in the stereo pairs some small loops disappeared and some large loops or segments of loops rearranged themselves. This also was seen for the $\pm \bar{g}$ pairs.

ii) The large loops do not lie on a simple crystallographic plane but are irregular, probably due to glide. It is unlikely that the loops

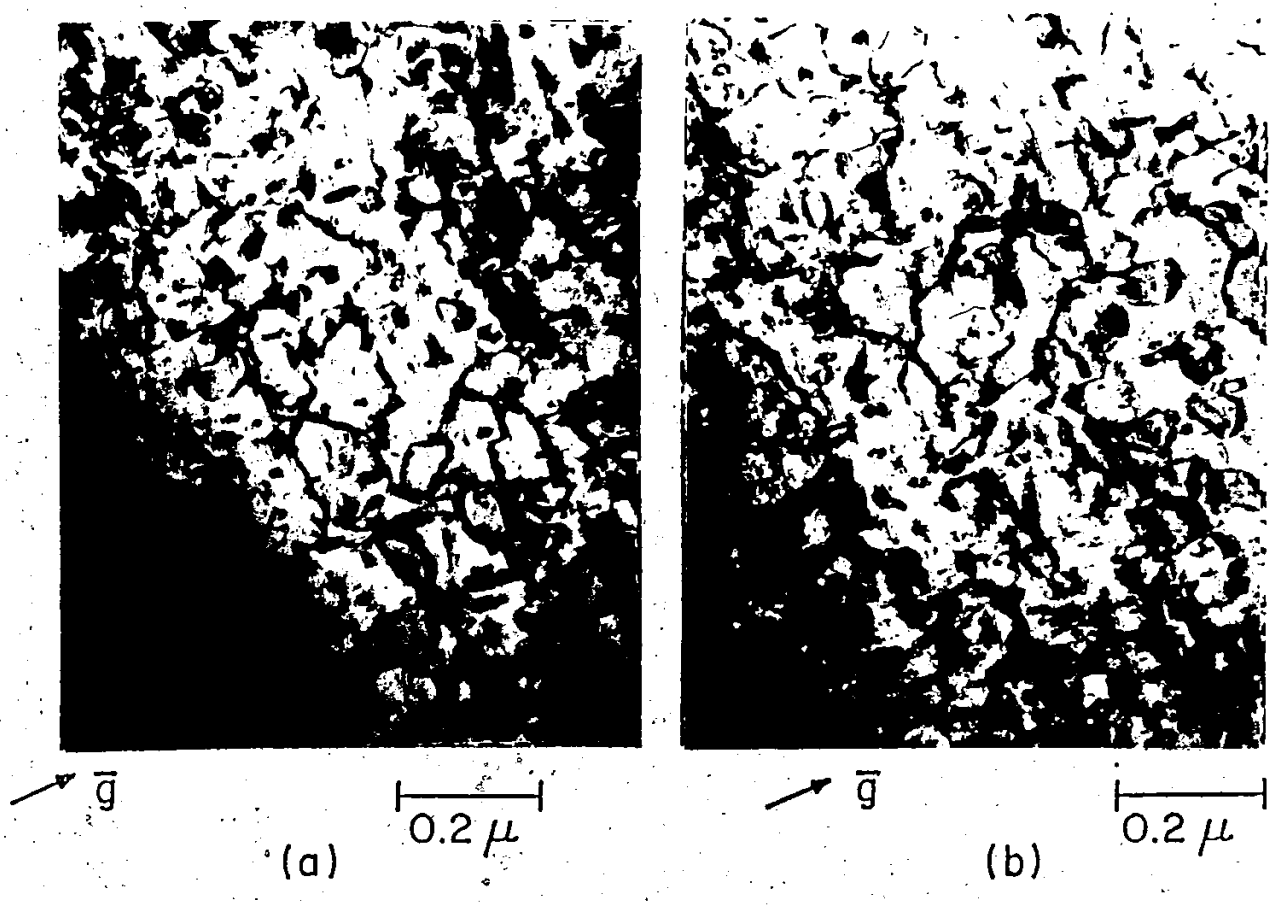

Fig. 6.15 A pair of stereo electron micrographs showing dislocation loops from a CdS crystal implanted with 2×10^{15} $Ar^{+}.cm^{-2}$. The orientation of the numbered loops is indicated in Table 6.3.

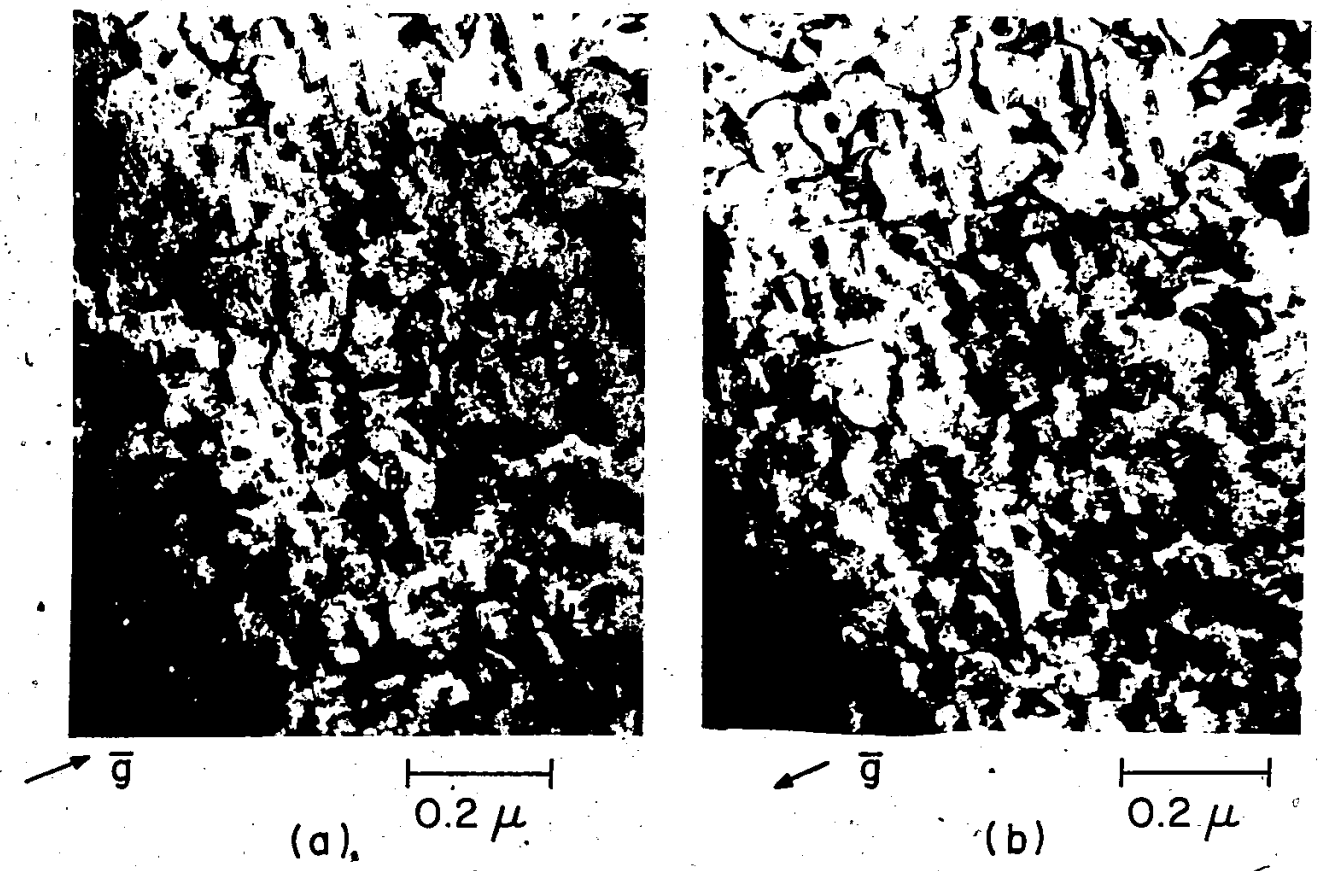

Fig. 6.16 A pair of micrographs from the same region of Fig. 6.15 under the ± $\bar{g}$ condition. The nature of the numbered loops is indicated in Table 6.3.

observed are pure edge loops. The presence of a substantial screw component in the loop complicates the analysis.

The ideal technique for loop characterization is to obtain ± $\bar{g}$ pairs with $\bar{g}$ approximately normal to the long axis of the projected image, as shown in Fig. 6.17. This gives better inside/outside contrast. However, to determine the inclination of the loop, it is necessary to tilt the sample through a large angle about an axis normal to $\bar{g}$. This causes $\bar{g}$ to change, and so some loops will go out of contrast, making the analysis difficult.

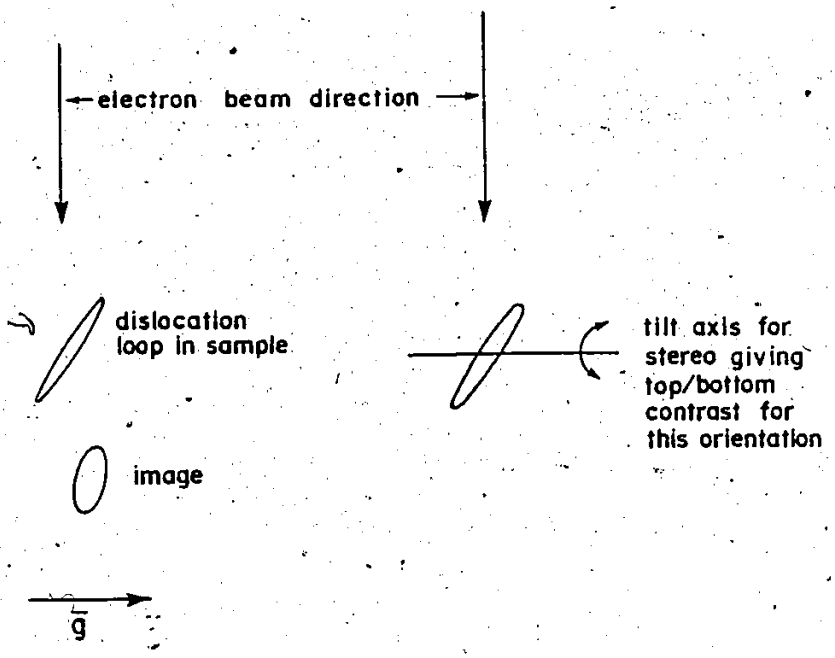

Fig. 6.17 An ideal technique for loop characterization is shown schematically.

A total of 20 loops were analysed. Of these, the nature of only 11 loops could be determined: nine were found to be vacancy type while only two were interstitial type. Table 6.3 identifies the loops, their orientation and inside/outside contrast. From this analysis it is concluded that a majority of the large loops are of vacancy type.

Lattice disorder in ion implanted CdS has been investigated using TEM by Govind et al. [1971], and Williams and Yoffe [1970]. The results of their investigations showed that implantation damage produces small clusters, a complex tangle of dislocation lines and loop-like features. These authors did not determine the Burgers vector of the dislocations. Yoshiie et al. [1981] studied 1 MeV electron damage produced in CdS foils and found that dislocation loops appear after irradiation with electrons for energies higher than 300 keV at temperatures below 600 K. These loops were found to be interstitial type, either with a Burgers vector $\vec{b}$ = 1/3 $\langle 2\bar{1}\bar{1}0\rangle$ on $\{\bar{1}2\bar{1}0\}$ or with $\vec{b}$ = 1/2 [0001] on the (0001) plane.

Results of the present study are similar to those of Yoshiie et al. [1983] except that the dislocation loops in the present investigation were identified as being predominantly vacancy type loops. This difference in the type of the loops produced may be due to the difference in mechanisms of damage production by electrons and heavy ions. Generally, electrons produce isolated interstitial - vacancy pairs while heavy ions of keV range produce displacement cascades involving many atoms [Sec. 3.1.4]. Heavy ion damage often results in a vacancy rich

Table 6.3

Characterization of dislocation loops produced by 60 keV Ar^+ implanted into CdS crystals ($2x10^{15}$ ions.cm^{-2}).

Loop No.	Loop Orientation (Fig. 6.15)	Inside/Outside Contrast (Fig. 6.16)	Type of loop I for Interstitial V for vacancy
2	/	✓	V
4	/	✓	V
5	?	✓	-
6	/	✓	V
7	\	✓	I
8	/	✓	V
9 to 11	/	✓	V
12	?	✓	?
13	/	✓	V
14	-	✓	?
15	/	✓	V
16	irregular		
17	-	✓	?
18	-	✓	?
19	-	✓	?
20	\	✓	I

core in the cascade, which may collapse and form vacancy loops surrounded by an outer shell which is rich in interstitials atoms. Intertstitial loops are generally formed by the agglomeration of freely migrating interstitials. Vacancy loops have been observed by Condon [1976] for As^+ and Kr^+ implanted crystals of CdTe, a II-VI compound which also has the wurtzite structure.

Since there is a similarity in the structures of hexagonal close packed (h.c.p.) and wurtzite crystals, the results of irradiation damage in h.c.p. metals are worth comparing with the present results. TEM studies of bismuth irradiated alpha-titanium (h.c.p. structure) were carried out by Wop et al. [1982], whose results showed that dislocation loops of vacancy type were formed, with a Burgers vector perpendicular to the c-axis. No evidence was found for a Burgers vector with a c-axis component. Another h.c.p. metal, zirconium has been studied extensively by Carpenter et al. [1981] (irradiated by 1 MeV electrons) and by Kelly et al. [1973] (neutron irradiated). Both groups showed that the damage structure consisted of dislocation loops with a unique Burgers vector $\vec{b} = 1/3 \langle 11\bar{2}0 \rangle$. Both vacancy and interstitial loops were found in the specimens irradiated at 400° C and annealed for an hour at 800° C but the vacancy type loops predominated.

6.2. RBS/Channeling

The results of the channeling/backscattering experiments are presented in the following five sections. In section 6.2.1. results are given of the cadmium disorder measured as a function of ion dose and ion species, implanted and analysed in-situ at 50 K. The damage was analysed using a 2 MeV He^+ beam channeled along the c-axis of the crystal. The analysing beam itself could introduce disorder in the crystal by atomic collisions. This has been investigated by bombarding both unimplanted and implanted (1 and $2x10^{15}$ $Bi^+.cm^{-2}$) CdS crystals in a non-aligned direction with 1 and 2 MeV He^+ and analysing with the same energy He^+ beam channeled along the c-axis. No significant change in the initial damage level of the crystal was observed for He^+ doses up to a total dose of 80 μC. Hence throughout this study, the total He^+ beam dose on a given area of the sample was maintained below this dose. For each individual analysis a He^+ dose of 2 μC was used, which resulted in a statistical uncertainty of < 10 %.

Damage produced by bismuth and neon implantation at 50 K was measured for either c-axis or a-axis channeling with 2 MeV He^+ and is reported in Sec. 6.2.2. To study the effects of temperature on damage production and damage analysis in CdS, the crystals were implanted and analysed at 300 K. The results are given in Sec. 6.2.3. and are compared with the results of implantation at 50 K. In Sec. 6.2.4. the implantation damage produced at 50 K and 300 K is measured as a function of the analysing beam energy channeled either along the c or along the

a-axis. Finally in Sec. 6.2.5. the radial distribution of displaced atoms across the channel is measured by introducing a small misalignment ($0.25\psi_c$ to $0.65\psi_c$) of the crystal axis with respect to the analysing beam.

6.2.1. Dose Dependence of Damage

Fig. 6.18 shows the energy spectra for 2.0 MeV He^+ channeled along the c-axis and scattered through 160^0 from crystals implanted with 0.5 to 4×10^{15} $Bi.cm^{-2}$ at 50 K. Also shown in the figure are the aligned unimplanted and the non-aligned spectra. The aligned spectra are characterized by a peak near the cadmium edge, due to cadmium disorder, which increases with increasing ion dose. The yield immediately behind the disorder peak, due to dechanneling of the ions traversing the disorder, also increases with ion dose. These increases in both the damage peak and the dechanneling level appear to saturate at a dose of $\simeq 2 \times 10^{15}$ $Bi^+.cm.^{-2}$ However the damage peak height only reaches up to $\simeq$ 50% of the non-aligned backscattering level.

The height of the damage peak depends on the number of scattering centers per unit area and on the depth resolution of the detector. For 2.0 MeV He^+ scattered through 160^0 from Cd atoms in CdS the depth resolution is $\simeq$ 25 nm. Since the projected range of 60 keV bismuth in CdS is $\simeq$18 nm [Winterbon table (1975)], which is smaller than the detector resolution, the damage peak will not reach the non-aligned level even if the implanted region becomes amorphous. In order to

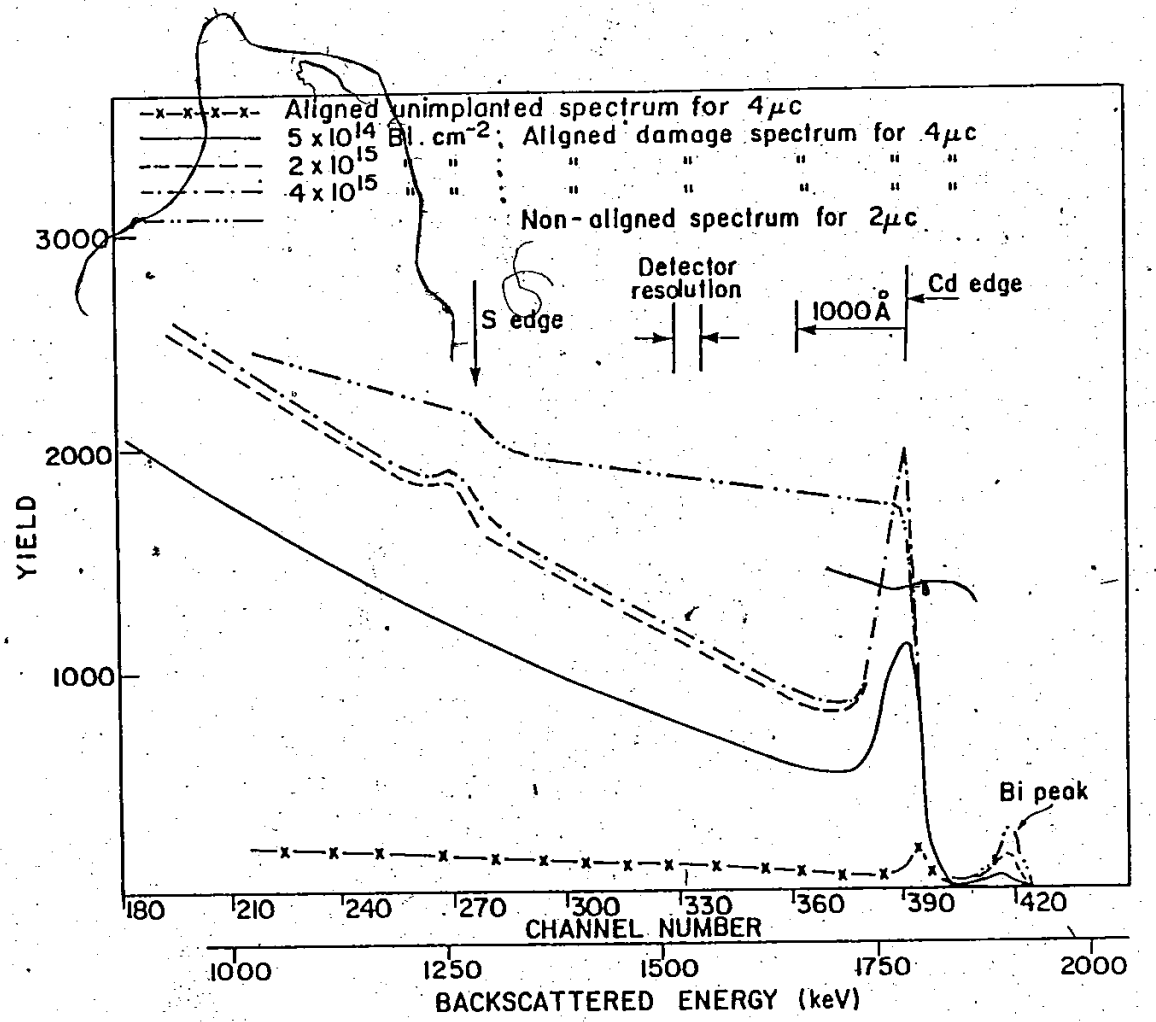

Fig. 6.18 RBS spectra for 2 MeV He^+, channeled along the c-axis, and scattered through 160^o from a CdS crystal implanted with 0.5 - $4x10^{15}$ $Bi^+.cm^{-2}$ at 50 K.

increase the depth resolution, a 100^{o} scattering geometry was used, i.e. with the beam exiting at 10^{o} to the sample surface. Spectra for such a scattering geometry are given in Fig. 6.19 for 2.0 MeV He^{+} channeled along the c-axis after 0.5 to $4x10^{15}$ $Bi.cm^{-2}$ implanted at 50 K. This geometry results in an improved depth resolution of ≈ 6 nm and the Cd peak is resolved into two peaks, one corresponding to the surface Cd atoms and the lower energy peak arising from the displaced Cd atoms due to the Bi implantation. THe surface peak height is seen to decrease from the non-aligned level as the Bi dose is increased, indicating taht the cadmium concentration at the surface is decreasing. This decrease in the cadmium concentration at the surface can be explained by the preferential sputtering of cadmium. Preferential sputtering of cadmium in CdS by Bi bombardment has been observed previously by Baxter [1977] and Parikh [1981]. The damage peak showed saturation in the peak height after ≈ $2x10^{15}$ $Bi.cm^{-2}$ which is only about half the non-aligned level. This observation confirmed the results of the TEM (Sec.6.1.1) that bismuth implantation in CdS does not amorphize the CdS crystal structure. This observation contrasts with that for other semiconductors such as Si, Ge and GaAs [Thompson and Walker 1976a, 1978, 1976b] which amorphize at 50 K for doses an order of magnitude lower than the ion dose at which damage saturation is observed in CdS. On the other hand, metals generally do not exhibit any amorphous damage layer when implanted with heavy ions, but they do exibit increased dechanneling [Picraux et al. 1978, Pronko et al. 1974]. This behaviour has been shown [Picraux et al. 1978, Pronko et al. 1974, Quéré 1974] to

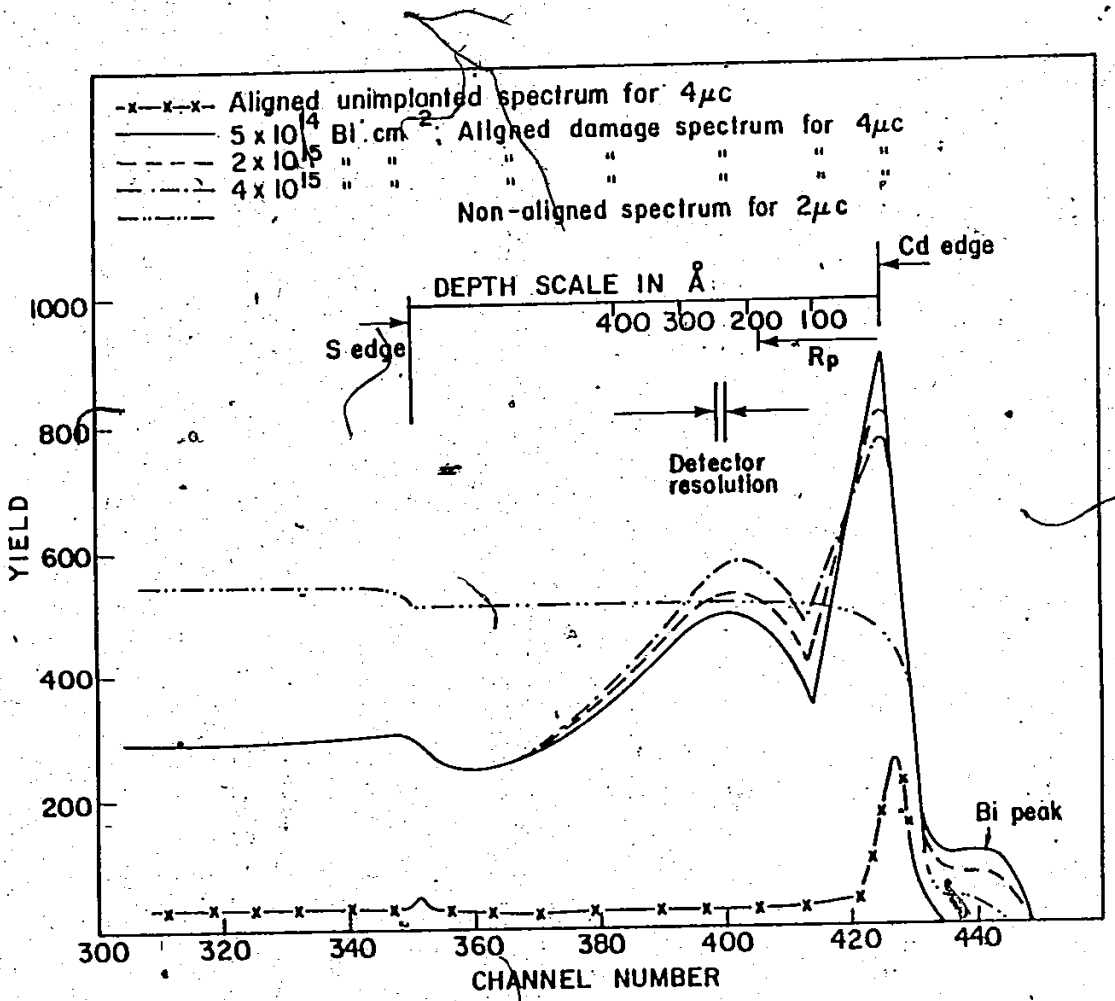

Fig. 6.19 RBS spectra for 2 MeV He^+, channeled along the c-axis, and scattered through 100^o from a CdS crystal implanted with 0.5 - 4x10^{15} $Bi^+.cm^{-2}$ at 50 K.

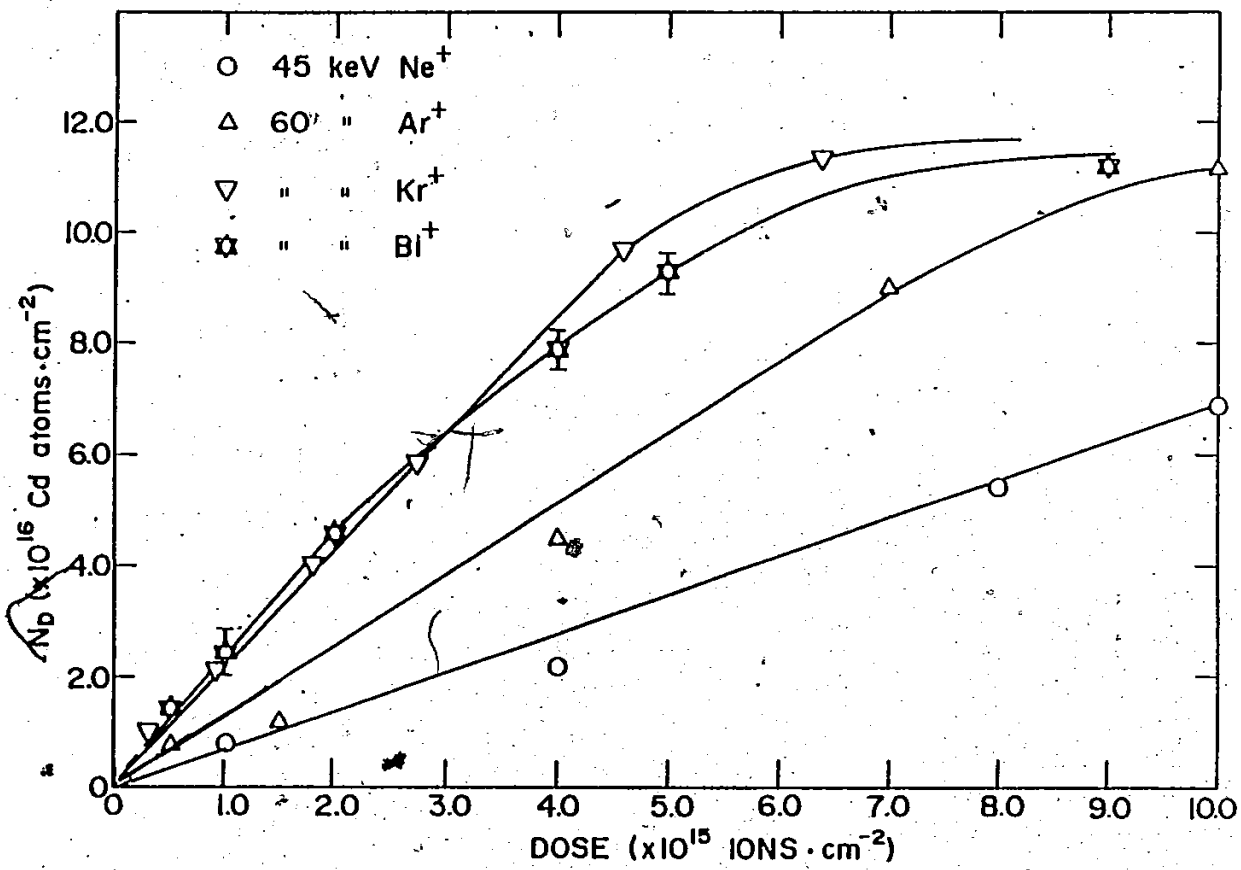

Fig. 6.20 N_D vs. dose for Ne^+, Ar^+, Kr^+ and Bi^+ implanted CdS crystals at 50 K and analysed in-situ at 50 K using 2 MeV He^+ channeled along the c-axis.

be the result of He^+ scattering from extended defects which are the principal form of damage produced by ion implantation in metals.

Fig. 6.20 is a plot of N_D versus ion dose, Φ, for 45 keV Ne^+ and 60 keV Ar^+, Kr^+, and Bi^+ implanted crystals analysed in-situ, at 50 K with 2.0 MeV He^+ channeled along the c-axis. The dose dependence of the number of scattering centers N_D reported here is for the 160^o scattering geometry. However, in some cases N_D was calculated using the 100^o scattering geometry. It was found that both sets of results agreed. For all of the ion species, N_D increases initially linearly with ion dose and for the heavier ions shows a tendency to saturate at a dose which decreases with increasing ion mass. For the Bi^+ and Kr^+ implanted samples the damage appeared to saturate after $\simeq 5x10^{15}$ ions.cm^{-2} while for Ar^+ saturation occurs at $\simeq 9x10^{15}$ ions.cm^{-2}. For 45 keV Ne^+ no such saturation of damage was observed up to the highest dose studied ($1x10^{16}$ ion.cm^{-2}). The values of N_D reported in this study were calculated from the damage peak which extended to a depth of $\simeq$ 100 nm. The damage peak position is approximately at R_p^D; but the tail extends deeper into the crystal. The total depth over which the damage was measured is 1.5 to 2 times greater than the $R_p^D + 3\Delta R_p^D$ as calculated from W.S.S. theory (Sec. 3.1.4). The measured and calculated values of R_p^D and ΔR_p^D are reported in Table 6.4. In the case of Bi implantation the depth of Bi peak was calculated to be $\simeq$ 28 nm which is approximately equal to the R_p^D measured (31nm). THis observation strongly suggest that inspite of tilting 20^o away from channeling direction during the implantation, some Bi ions must have channeled and created the deeper damage.

An estimate of the amount of disorder (number of scattering centers) produced by the different ions is obtained from the slope of the plot N_D vs. dose in the linear region; i.e. as $\Phi \to 0$. These values of $dN_D/d\Phi$ as $\Phi \to 0$, along with the calculated elastic energy deposited [Winterbon 1975] $\nu(E)$, for each ion species are given in Table 6.4. The experimental results of $dN_D/d\Phi$ as $\Phi \to 0$ are also compared in Table 6.4 to the calculated values obtained using Eq. 3.18. The calculated values are approximately 2-3 orders of magnitude larger than the measured values. This large difference in the $dN_D/d\Phi$ values suggests that either there is strong annealing of point defects produced during the implantation, even at a temperature of 50 K, and/or the point defects agglomerate in such a way that the direct scattering probability is drastically reduced.

Table 6.4

Atomic collision parameters for various ions implanated into CdS

Ion Species	Energy (keV)	Elastic Energy Deposited (keV)	Measured R_p^D (nm)	Calculated R_p^D (nm)	Calculated ΔR_p^D (nm)	$dN_D/d\Phi$ as $\Phi \to o$ Exp.	Cal.
Bi	60	43.7	31	I3	8	22	2500
Kr	60	41	65	20.6	18	22	2360
Ar	60	37.3	85	34.0	21	13	2150
Ne	45	23.6	70	46.0	26	7	1360

For the Bi^+ and Ne^+ implanted samples, the change in the dechanneling behind the damage peak, $\Delta\chi_{min} = \{\chi_{min}(\text{damaged}) - \chi_{min}(\text{undamaged})\}$, is plotted as a function of implant dose as shown in Figs. 6.21 and 6.22 respectively. Both the figures show similar functional behaviour to that of their respective N_D vs. dose plot (Fig. 6.20). The Bi^+ implanted sample (Fig. 6.21) shows a linear increase in $\Delta\chi_{min}$ up to a dose of $\simeq 2.5\times10^{15}$ $Bi.cm^{-2}$ with a slope of 7×10^{-17} cm^2. For doses larger than 2.5×10^{15} $Bi.cm^{-2}$, $\Delta\chi_{min}$ still increases, but less rapidly with increasing dose and saturates at $\simeq 5\times10^{15}$ $Bi.cm^{-2}$. The Ne^+ implanted sample shows a linear increase in $\Delta\chi_{min}$ over the entire dose range studied: i.e. up to a dose of $\simeq 1\times10^{16}$ $Ne^+.cm^{-2}$; however, the slope is only $1\times10^{-17}cm^2$.

For comparison, $\Delta\chi_{min}$ was calculated from the measured N_D values using Bøgh's single scattering model [1968] and is also given in Figs. 6.21 & 6.22. In such a calculation it is assumed that N_D represents the number of displaced atoms randomly distributed across the channel.

Comparing the measured and calculated values of $\Delta\chi_{min}$, it is noted that the measured $\Delta\chi_{min}$ is much larger than the theoretically calculated $\Delta\chi_{min}$. This again indicates that the displaced atoms are not randomly distributed, but must be agglomerating into extended defects which is contrary to the annealing argument since annealing would also be expected to result in values of $\Delta\chi_{min}$ closer to the calculated values. The formation of extended defects explains the enhancement in

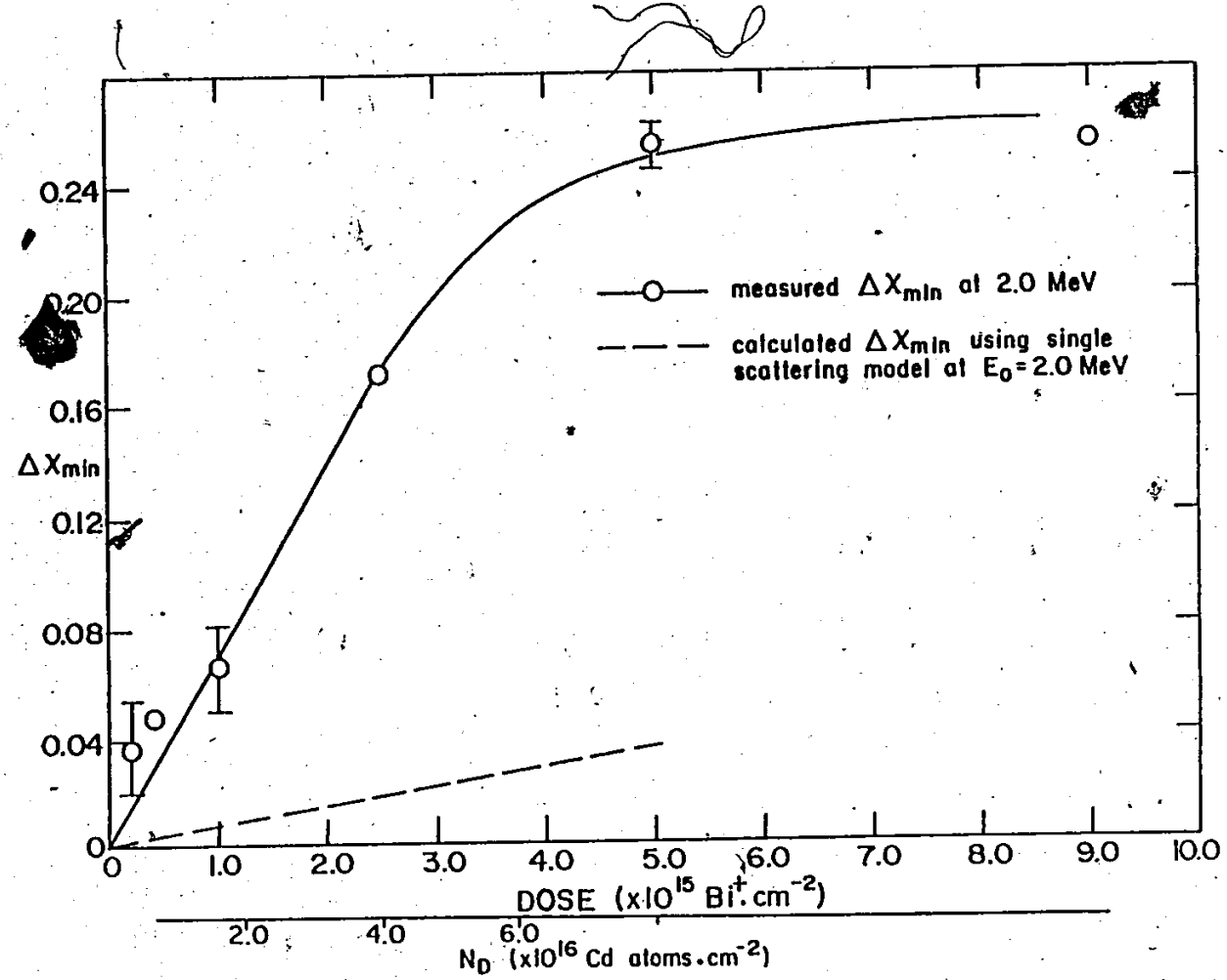

Fig. 6.21: $\Delta\chi_{min}$ vs. dose for a CdS crystal implanted with 60 keV Bi^+ at 50 K and analysed in-situ at 50 K using 2 MeV He^+ channeled along the c-axis. Calculated values of $\Delta\chi_{min}$ are also shown for comparison.

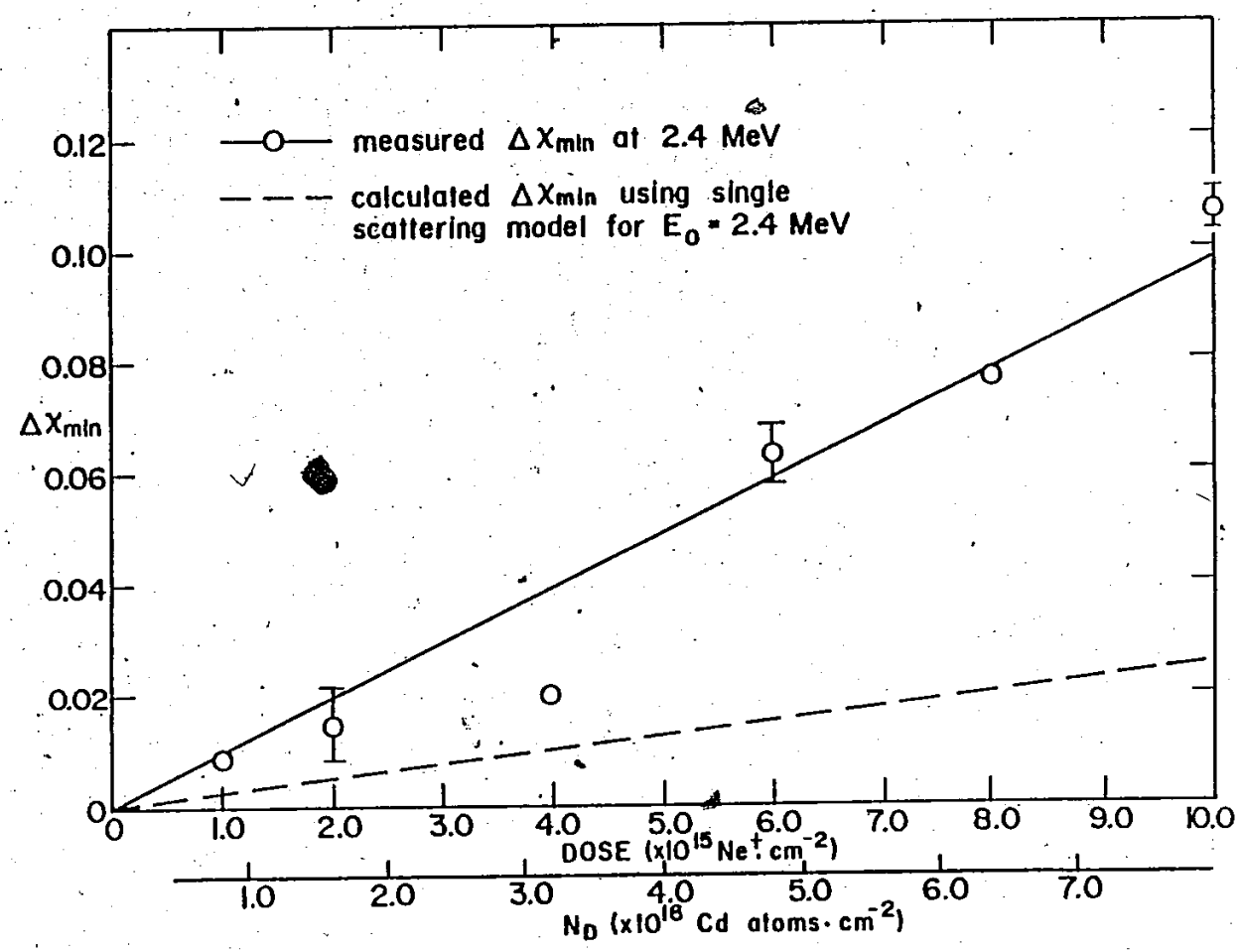

Fig. 6.22 $\Delta\chi_{min}$ vs. dose for a CdS crystal implanted with 45 keV Ne^+ at 50 K and analysed in-situ at 50 K using 2 MeV He^+ channeled along the c-axis. Calculated values of $\Delta\chi_{min}$ are also shown for comparison.

dechanneling and reduction in Rutherford backscattering since the atoms surrounding such defects are only slightly displaced from their lattice sites and would not contribute efficiently to the backscattering yield as is observed. This conclusion is supported by the TEM results in which the visible defects are primarily dislocation loops (Sec. 6.1.1.).

6.2.2. Crystal Orientation Effects on Measured Disorder

TEM results showed that ion implantation produced dislocation loops in CdS, the majority of which had a Burgers vector perpendicular to the c-axis i.e. the strain in the lattice is perpendicular to the c-axis. If the damage is analysed by He^+ beam channeling along the c- and the a-axes, dechanneling should be stronger along the c-axis than along the a-axis. To investigate the dependence of N_D and the dechanneling behaviour on the channeling direction, the samples implanted with Bi^+ or Ne^+ were analysed along both the c-axis and a-axis.

Figs. 6.23 and 6.24 are plots of N_D and Δx_{min} vs. dose respectively for crystals implanted with 60 keV Bi^+ and 45 keV Ne^+ and analysed at 50 K with 2.0 MeV He^+ channeled along along the c- and a-axes. The striking feature of both the figures is that both N_D and Δx_{min}, measured along the c-axis, are much larger than that measured along the a-axis. For Bi^+ implanted crystals, N_D and Δx_{min} observed along the c- and a-axes increase with ion dose and exhibit a tendency to saturation at doses of $\approx 4 \times 10^{15}$ $Bi.cm^{-2}$ for c-axis channeling, and at $\approx 1 \times 10^{15}$ $Bi.cm^{-2}$ for a-axis channeling. The damage observed along the

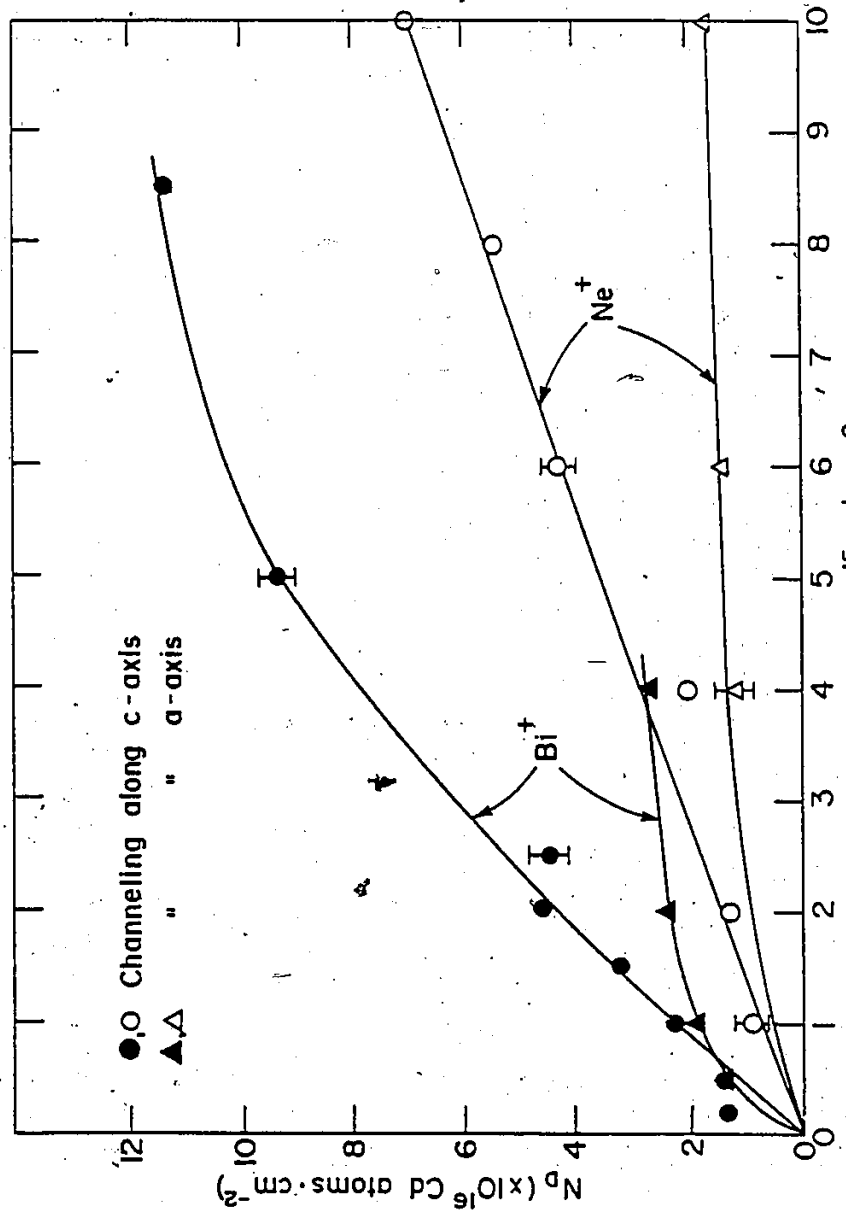

Fig. 6.23 N_D vs. dose for Bi^+ and Ne^+ implanted CdS at 50 K; analysed using 2 MeV He^+ channeled along the c-axis and along the a-axis.

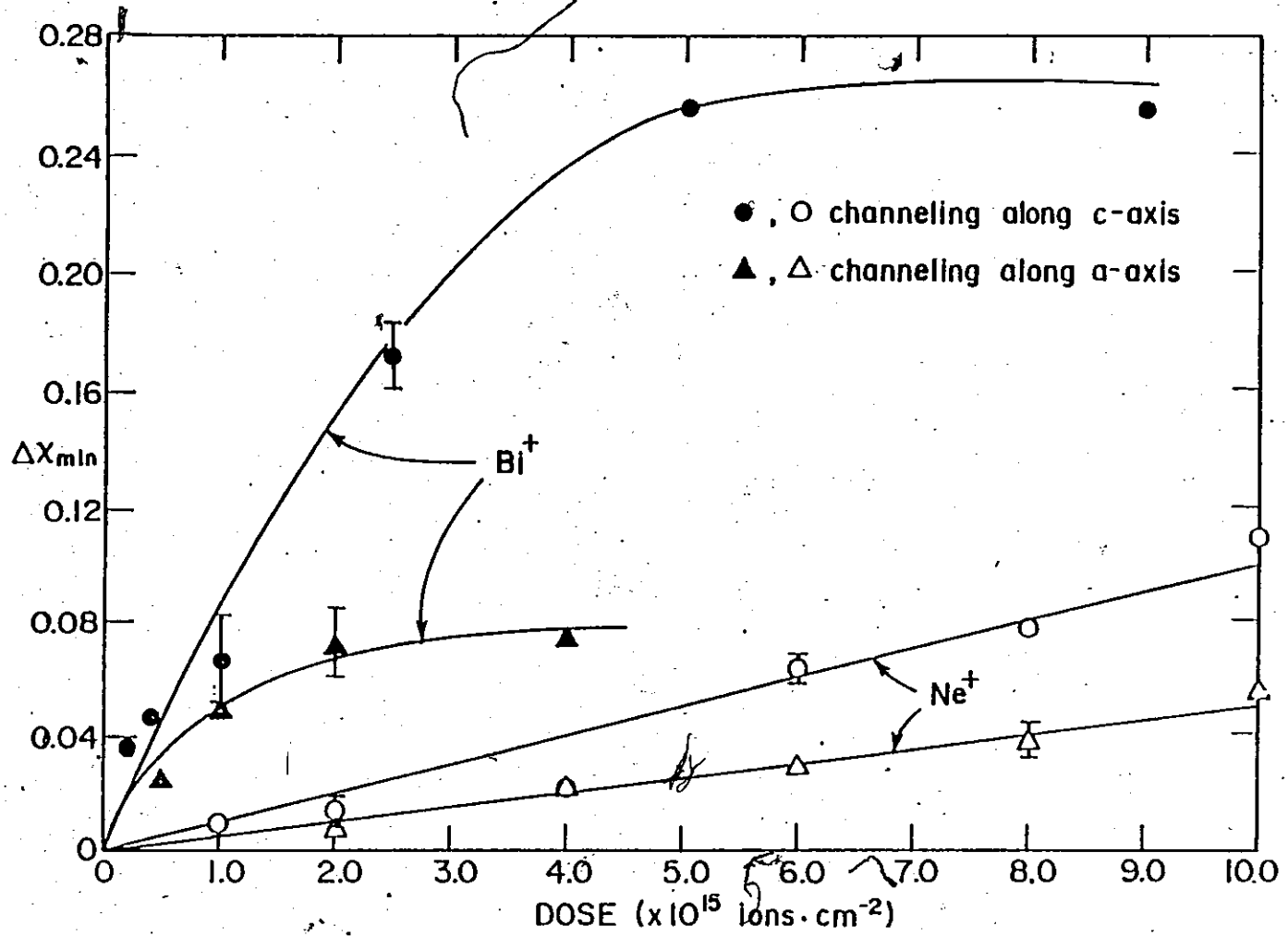

Fig. 6.24 Δx_{min} vs. dose for Bi^+ and Ne^+ implanted CdS at 50 K ; analysed using 2 MeV He^+ channeled along the c-axis and along the a-axis.

c-axis saturates at a level approximately 4 times that observed along the a-axis. However, for Ne^+ implants over the dose range investigated, saturation for N_D was observed only in the case of a-axis channeling. The slope of Δx_{min} vs. neon dose for c-axis channeling is $1x10^{-17}$ cm^2 and for a-axis channeling is $5x10^{-18}$ cm^2. No saturation of Δx_{min} was observed along either axis.

The larger N_D for channeling analysis along the c-axis indicates that the scattering centers are positioned such that a higher backscattering probability occurs for the c-axis channeling than for a-axis channeling. The possible sources of enhanced backscattering for axial channeling along the c-axis are: i) preferential occupancy of interstitial sites in the wurtzite structure; and ii) strain associated with the dislocation loop structure observed in the TEM studies.

(i) In the wurtzite structure two types of stable interstitial sites are possible, namely octahedral sites (O) and tetrahedral sites (X). There are six such sites of each type in each unit cell. The projection of these sites is shown in Fig. 6.25.

If the X sites are preferentially occupied then a basal plane projection indicates that the interstitial site is shadowed by rows of atoms when the analysing beam is along the c-axis. Hence there should not be any increase in the backscattering yield due to occupancy of such sites. On the other hand, if O sites are preferentially occupied, they would be in the center of the channel when the analysing beam is along

the c-axis, and would give rise to strong backscattering. For the case of the incident beam being parallel to the a-axis, a similar argument leads to the fact that both O and X sites will give rise to weaker backscattering because both the sites are now away from the center of channel as can be seen in Fig. 6.25 (b). From the observed results, it is reasonable to conclude that, if the defects giving rise to the damage peak (and hence N_D) are interstitials, then the O site occupancy should be dominant for implantation produced interstitials in the CdS structure [Parikh et al. (1983)].

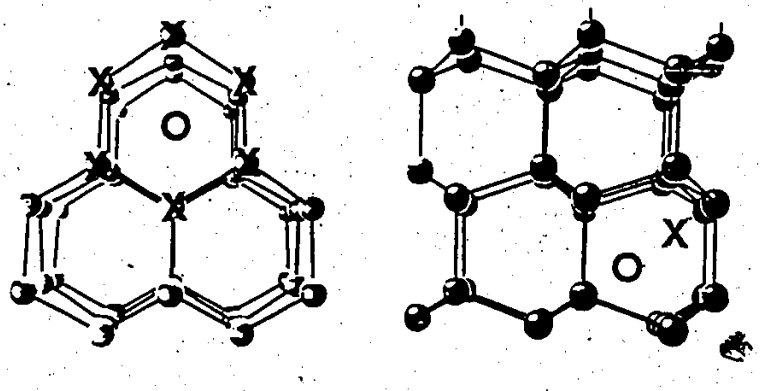

(a) (b)

Fig. 6.25 Projection of octahedral and tetrahedral sites along the c-axis (a), and a-axes (b), of the wurtzite structure.

(ii) TEM observations showed that dislocation loops are produced following Bi^+, Ar^+ and Ne^+ implantation in CdS crystals. The larger loops of type II were determined to be of the vacancy type. The Burgers vector of the majority of the loops is perpendicular to the c-axis i.e. the lattice strain perpendicular to the c-axis is larger. Those atoms which are displaced significantly from their lattice sites will enhance the backscattering and dechanneling probability for c-axis channeling as compared to a-axis channeling. This is consistent with the measurements as given in Figs. 6.23 and 6.24.

6.2.3. Effects of Temperature on Damage Production and Damage Analyses: 50 K vs. 300 K

The RBS/channeling results presented so far are for implantation and analysis performed at 50 K while the TEM observations reported in Sec. 6.1.1 and 6.1.2 are for samples implanted at 300 K. To compare the damage observed by the two independent techniques, RBS/channeling and TEM, and also to see the effects of temperature on damage production and damage analysis, several samples were implanted and analysed at both 50 K and 300 K. In addition, samples implanted at 300 K were analysed at both 300 K and 50 K.

Fig. 6.26 is a plot of N_D vs. dose for bismuth implants at 50 K and 300 K, analysed with 2.0 MeV He^+ channeled along the c-axis and the a-axis. It is interesting to note that the observed damage is greater at 300 K than at 50 K for analyses along both the axes, except for doses

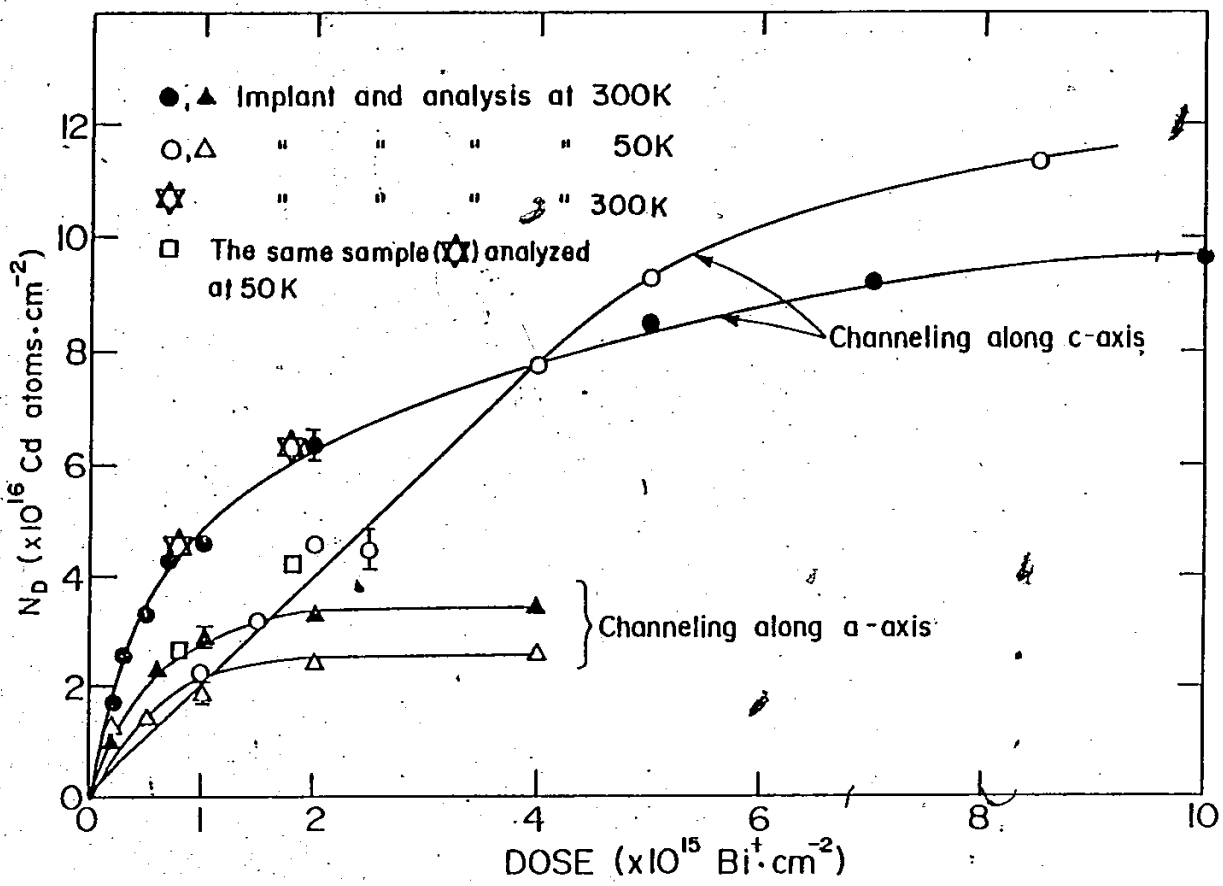

Fig. 6.26 N_D vs. dose for a Bi^+ implanted CdS crystal analysed at 50 K and 300 K with 2 MeV He^+ channeled along the c-axis.

beyond $4x10^{15}$ $Bi^{+}.cm^{-2}$ when analysed along the c-axis. This again contradicts the annealing of point defects hypothesis, since generally at higher temperatures one expects higher mobility of point defects and therefore damage annealing. Fig. 6.27 shows the variation of $\Delta\chi_{min}$ vs. dose, for crystals implanted with Bi^{+} and Ne^{+} at 300 K and 50 K, and subsequently analysed at the implant temperatures for channeling along the a- and the c-axes. The variation of $\Delta\chi_{min}$ with dose is similar to the variation of N_D with dose for both the axes, as seen earlier in Fig. 6.26. For the damage analyses along the c-axis, $\Delta\chi_{min}$ is higher for 300 K implants up to a dose of $4x10^{15}$ $Bi.cm^{-2}$, where it saturates at $\approx$ 0.23 while for 50 K implants and analysis, $\Delta\chi_{min}$ is initially lower, but saturates at a higher level $\approx$ 0.26. When the damage is analysed along the a-axis, $\Delta\chi_{min}$ was always higher for 300 K implantation than for 50 K implantation and the cross-over observed in N_D and $\Delta\chi_{min}$ plots for the c-axis analysis was not observed. The cross-over observed in N_D and $\Delta\chi_{min}$ plots beyond $4x10^{15}$ $Bi.cm^{-2}$ may be due to some annealing of defects at 300 K (Sec. 6.1.3).

To determine if the greater damage observed at higher temperature is an annealing effect, a sample was implanted with Bi^{+} to doses of $8x10^{14}$ and $1.6x10^{15}$ $ions.cm^{-2}$ at 300 K and analysed along the c-axis at the same temperature. After the sample was analysed at 300 K, for each implant dose it was then cooled down to 50 K for re-analysis, and the N_D and $\Delta\chi_{min}$ values were determined. The results showed that within experimental accuracy, the values of N_D and $\Delta\chi_{min}$ obtained were solely a function of the analysis temperature and that no measureable annealing

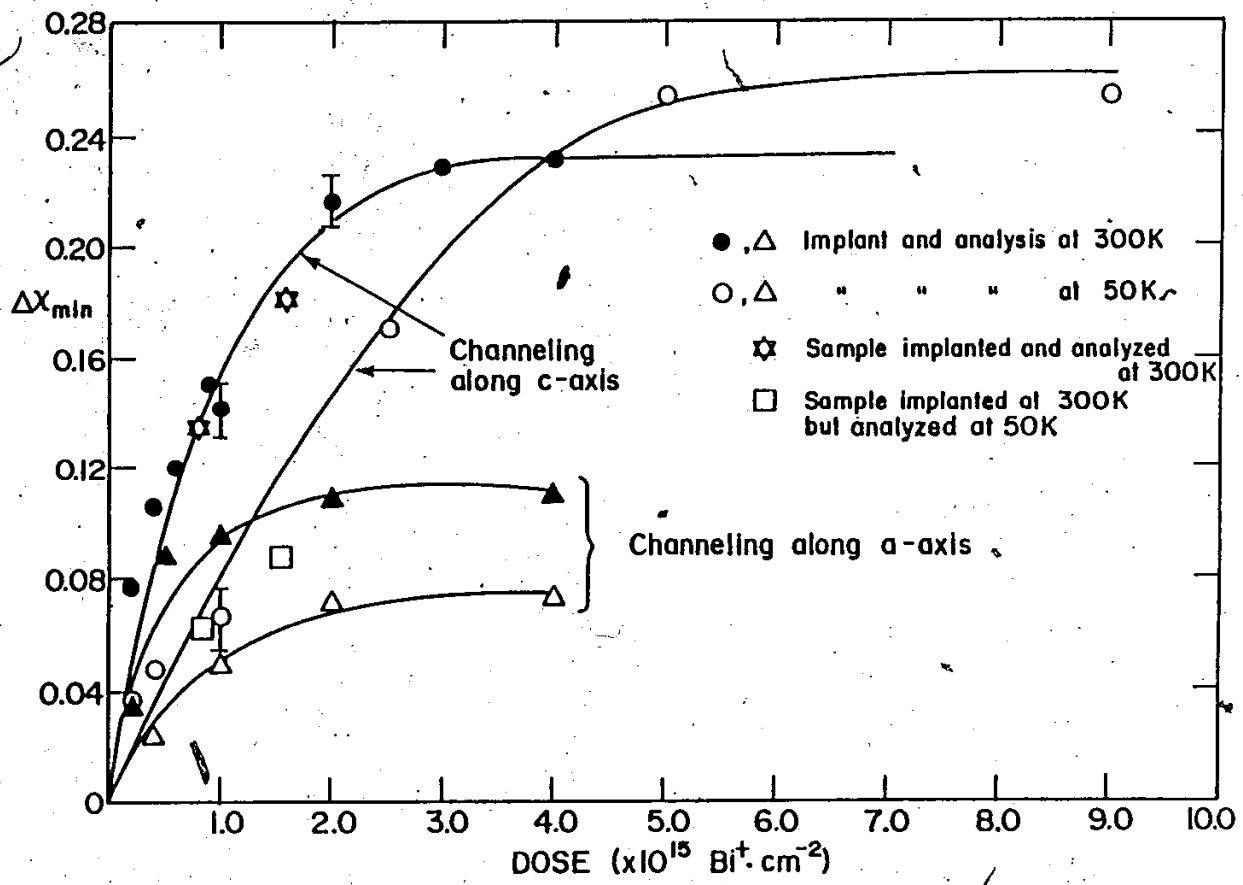

Fig. 6.27 $\Delta\chi_{min}$ vs. dose for a Bi^{+} implanted CdS crystal analysed at 50 K and 300 K with 2 MeV He^{+} channeled along the c-axis.

was observed. These results are shown in Figs. 6.26 and 6.27. Now if N_D were to be a measure of the areal density of randomly distributed displaced atoms, a decrease in the sample temperature for analysis should not change N_D. However, damage which was N_D produced at 300 K and measured at 50 K showed the same value as that obtained for implantation and analysis at 50 K. This suggests that the scattering centers are not randomly distributed but are positioned near the atomic rows. It also suggests that the damage produced at 50 K and 300 K is the same. Following this observation the temperature dependence of the N_D values is explained qualitatively as follows.

When implantation damage is analysed at 50 K some of the atoms may not be displaced enough from their lattice sites to backscatter the channeled He^+ ions; but at 300 K these atoms may now significantly backscatter the channeled ions since they have a larger thermal vibrational amplitude which displaces these atoms further out into the channel.

In another experiment, a CdS sample was implanted with 2×10^{15} $Bi.cm^{-2}$ at 50 K and subsequently analysed at the same temperature, then the sample was warmed to 300 K and was kept at this temperature for 20 hr. in the target chamber. When this sample was recooled to 50 K and analysed again, N_D and Δx_{min} were found to be unchanged from the analysis done immediately after the implantation. This result indicates that by warming the sample to 300 K, implantation damage does not anneal out. This result contradicts the TEM observations which showed a large

amount of annealing of the defects for a sample implanted under similar conditions and kept at 300 K for the same period of time [Sec. 6.1.3.]. It should be noted here that dislocation loops are not expected to anneal out at 300 K [Yoshiie et al. (1981)]. However, it may be possible that at higher damage levels a large amount of strain energy is stored, which provides a driving force for annealing at 300 K. Since the TEM samples thickness is comparable to the damage depth, the samples provide two surfaces for defect annealing to occur compared to one surface in the case of the thick (1-2 mm) RBS samples.

The neon implanted sample again showed higher N_D and $\Delta\chi_{min}$ for crystals implanted and analysed at 300 K than that analysed at 50 K. However, the cross-over which was observed for Bi implanted crystals was not seen (Fig. 6.28 and 6.29).

Lattice disorder in ion implanted CdS crystals has been studied by Baxter [1977], Huchby [1972] and Armitage [1970, 1975] using the RBS/channeling technique. Their investigations concentrated on the amount of lattice disorder as a function of ion dose for different ion species. They concluded that the implantation damage does not produce an amorphous layer in CdS crystals. Baxter investigated implantation damage in CdS at 300 K produced by 40 keV Bi^+, Ar^+ and Ne^+. This analyses were performed with 2.0 MeV He^+ ions, channeled along the c-axis. This author observed the saturation of N_D and $\Delta\chi_{min}$ for the Bi^+, and Ar^+ implanted crystals for a dose of $\simeq 2\times10^{16}$ ions.cm^{-2}, while the Ne^+ implanted crystals did not show a damage peak, in the spectrum.

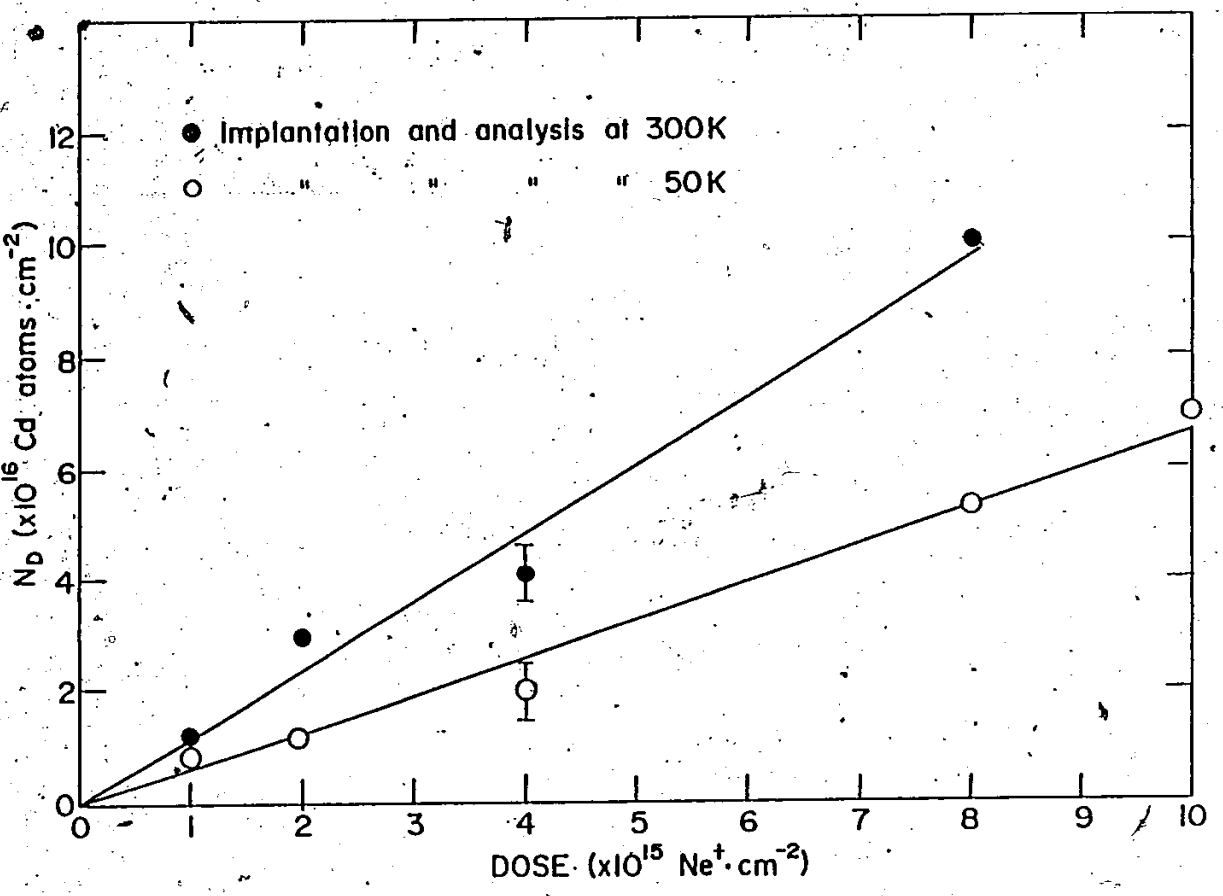

Fig. 6.28 N_D vs. dose for a Ne^+ implanted CdS crystal analysed at 50 K and at 300 K with 2 MeV He^+ channeled along the c-axis.

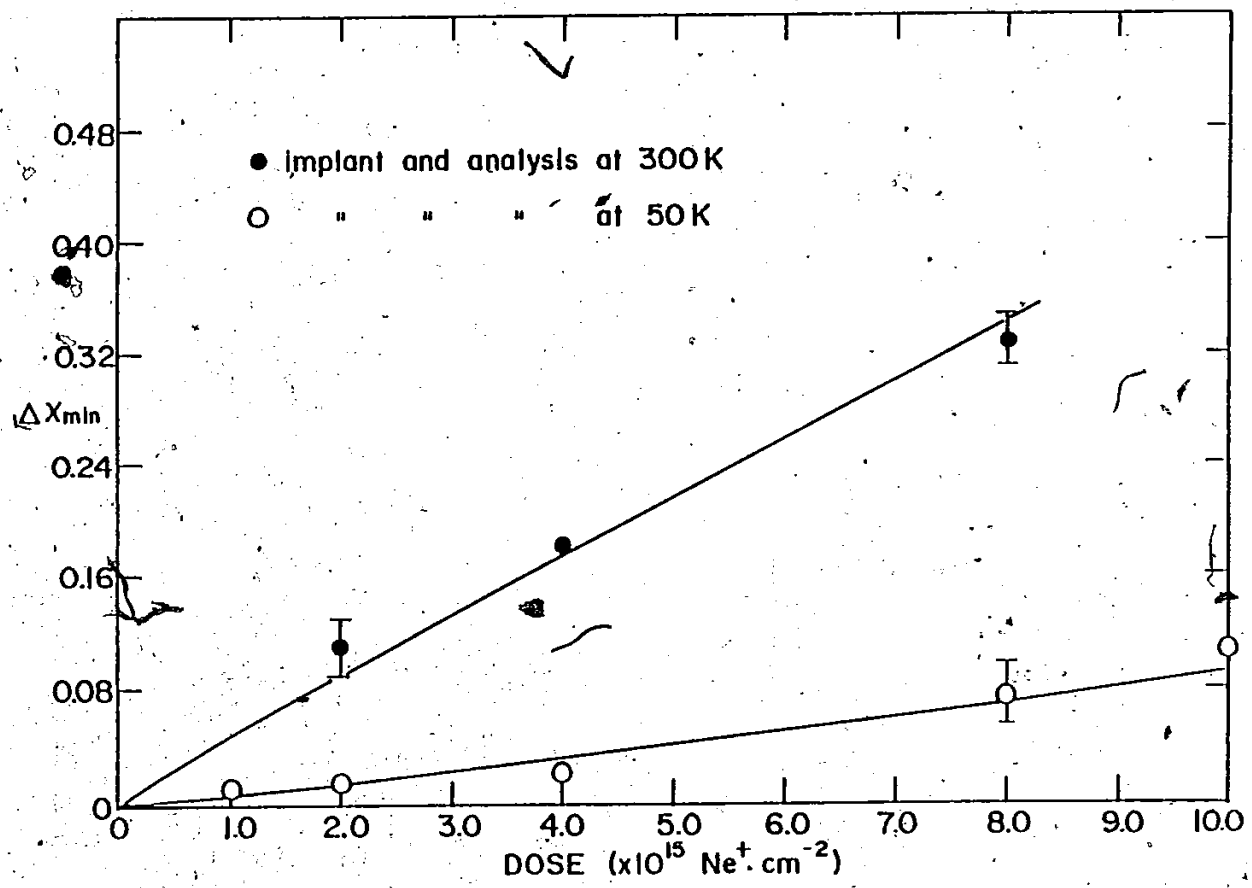

Fig. 6.29 $\Delta\chi_{min}$ vs. dose for a Ne^+ implanted GaS crystal analysed at 50 K and at 300 K with 2 MeV He^+ channeled along the c-axis.

The values of $dN_D/d\Phi$ as $\Phi \rightarrow 0$, measured for Bi^+ and Ar^+ implanted crystals were only ≈ 0.7 and 0.8 respectively. These values are about 2-30 times smaller than the results for 50 K implants of 60 keV Bi^+ and Ar^+ as given in Table 6.4 for the present investigation. This difference in the measured values of $dN_D/d\Phi$ may not be accounted for by the difference in the incident energies of the implanted ions. The Bi^+ implantation damaged analysed at 300 K gave even larger $dN_D/d\Phi$ as $\Phi \rightarrow 0$ than that for implantation and analysis at 50 K. The greater damage observed in the present study may be due to the fact that all our investigations were carried out in-situ whereas Baxter's anlysis were not. Leaving implanted samples at room temperature for an extended period of time may have caused some annealing of the defects. The absence of a damage peak in the neon implanated sample in Baxter's analysis could also be explained by the same argument.

6.2.4. Dependence of Analysing Beam Energy on Damage

The nature of lattice defects in a single crystal can often be inferred by studying the dechanneling (Δx_{min}) behaviour as a function of the analysing beam energy, E_o, as discussed in Sec. 4.2.3.

In this section results are presented about the dependence of N_D and Δx_{min} on the analysing beam energy E_o, for samples implanted with Bi^+ and Ne^+ at 50 K and 300 K, and analysed at the implant temperatures along both the c- and a-axes. Fig. 6.30 shows the variation of N_D vs. E_o for a sample implanted with 0.5 - 2×10^{15} $Bi^+.cm^{-2}$ at 50 K, and ana-

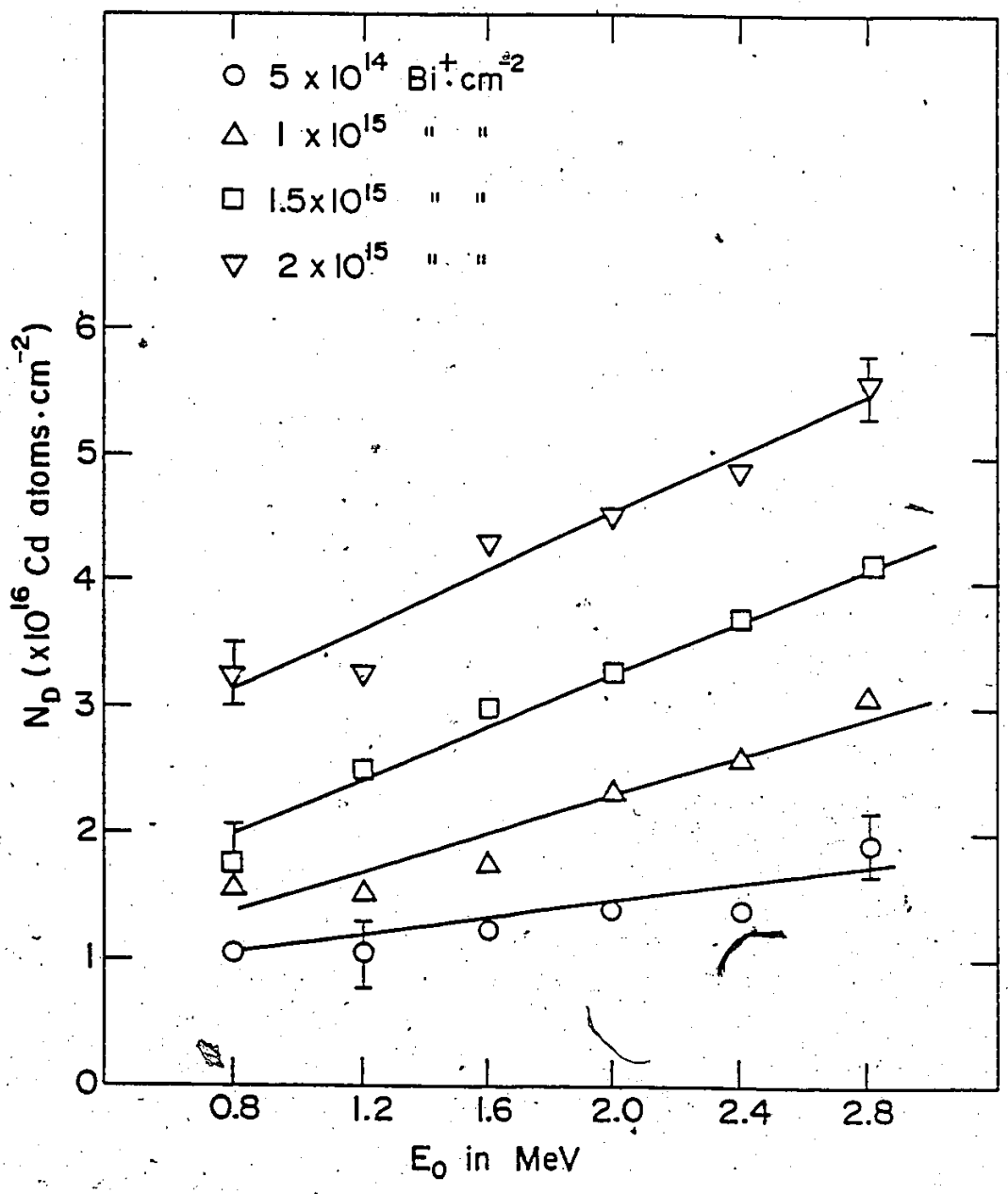

Fig. 6.30 N_D vs. E_o for a CdS crystal implanted with 0.5 - 2x10^{15} $Bi.cm^{-2}$ at 50 K and analysed along the c-axis.

lysed along the c-axis. The figure shows that N_D increases linearly with E_o. The slope of the curves increases with implant dose. The dependence of $\Delta\chi_{min}$ on E_o is plotted in Fig. 6.31 which shows that $\Delta\chi_{min}$ is almost independent of E_o, decreasing slightly as E_o increases.

Similar behaviour of the energy dependence of N_D and $\Delta\chi_{min}$ was observed at 50 K when the Bi^+ and Ne^+ implanted crystals were analysed along the a-axis, as shown in Figs. 6.32, 6.33, 6.34 and 6.35. The dependences of N_D and $\Delta\chi_{min}$ on the analysing beam energy, E_o, for a crystal implanted with Bi^+ at 300 K and analysed along the a-axis at same temperature is given in Figs. 6.36 and 6.37. The results again showed that N_D increases with increasing E_o, however in this case $\Delta\chi_{min}$ decreases quite strongly with increasing E_o.

To show the effects of the channeling directions and the analysis temperature on N_D and $\Delta\chi_{min}$, results presented earlier for an implant dose of 2×10^{15} ions.cm^{-2} are replotted. Figs. 6.38 and 6.39 are plots of N_D and $\Delta\chi_{min}$ vs. E_o for Bi^+ implanted crystals analysed at 50 K, with the He^+ beam channeled along the c- and the a-axes. The above figures clearly show that for all the analysing beam energies, the damage measured along the c-axis is greater than that measured along the a-axis, as seen in Sec. 6.2.2. The effects of temperature on damage analyses are shown in Figs. 6.40 and 6.41, for Bi^+ implanted crystals analysed along the a-axis. The plots show that N_D and $\Delta\chi_{min}$ are higher for damage analysed at 300 K than when for analysed at 50 K.

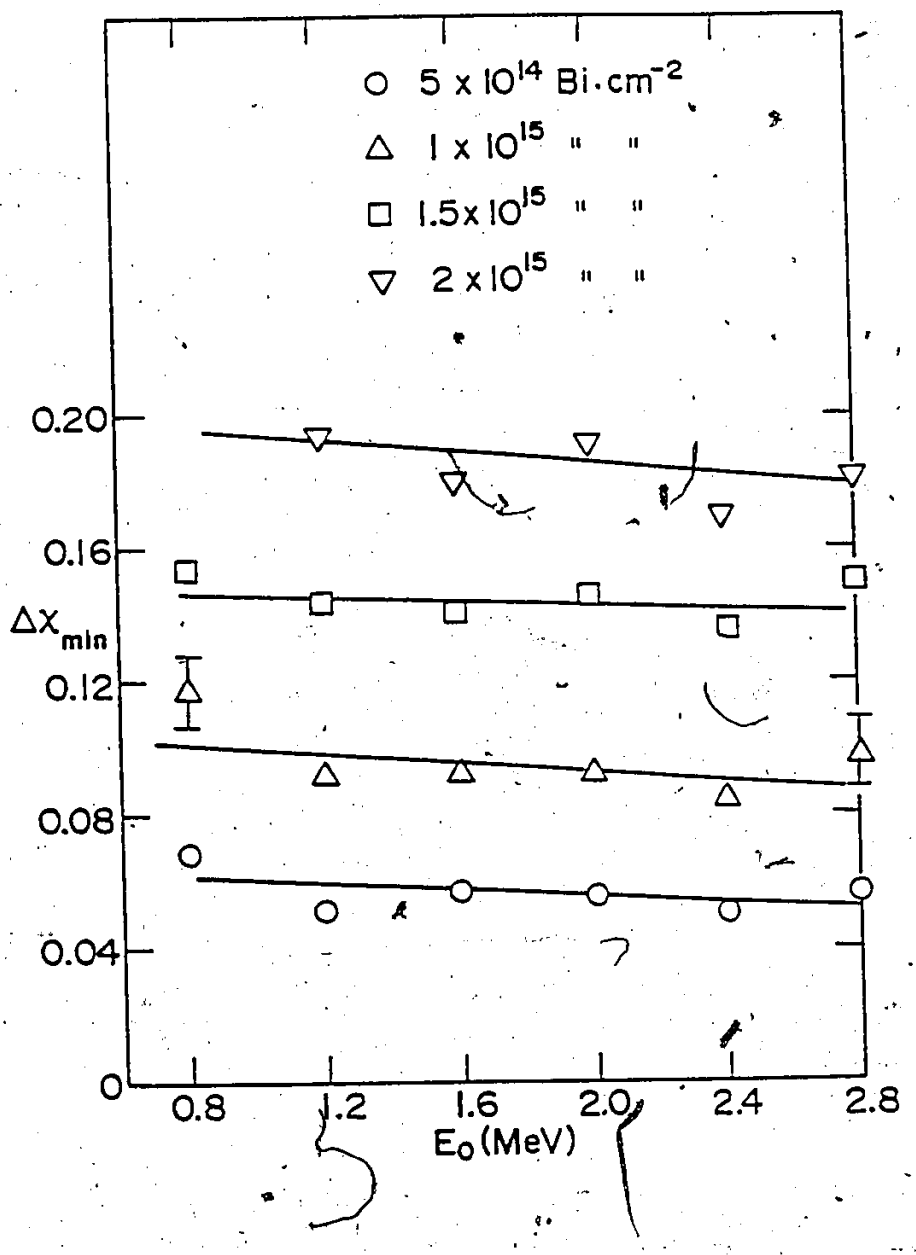

Fig. 6.31 Δx_{min} vs. E_0 for a CdS crystal implanted with 0.5 - 2×10^{15} $Bi.cm^{-2}$ at 50 K and analysed along the c-axis.

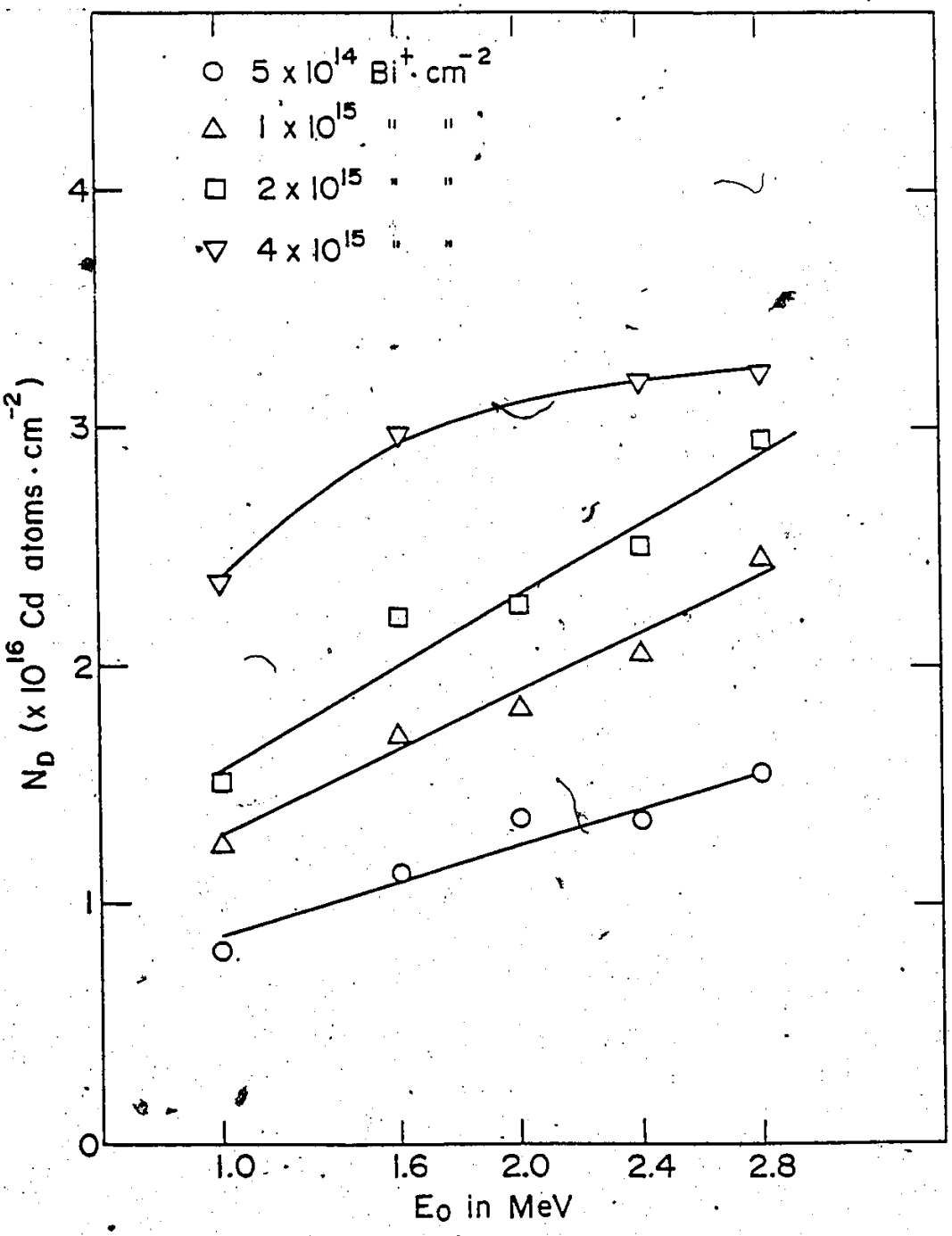

Fig. 6.32 N_D vs. E_o for a CdS crystal implanted with 0.5 - 4×10^{15} $Bi.cm^{-2}$ at 50 K and analysed along the a-axis.

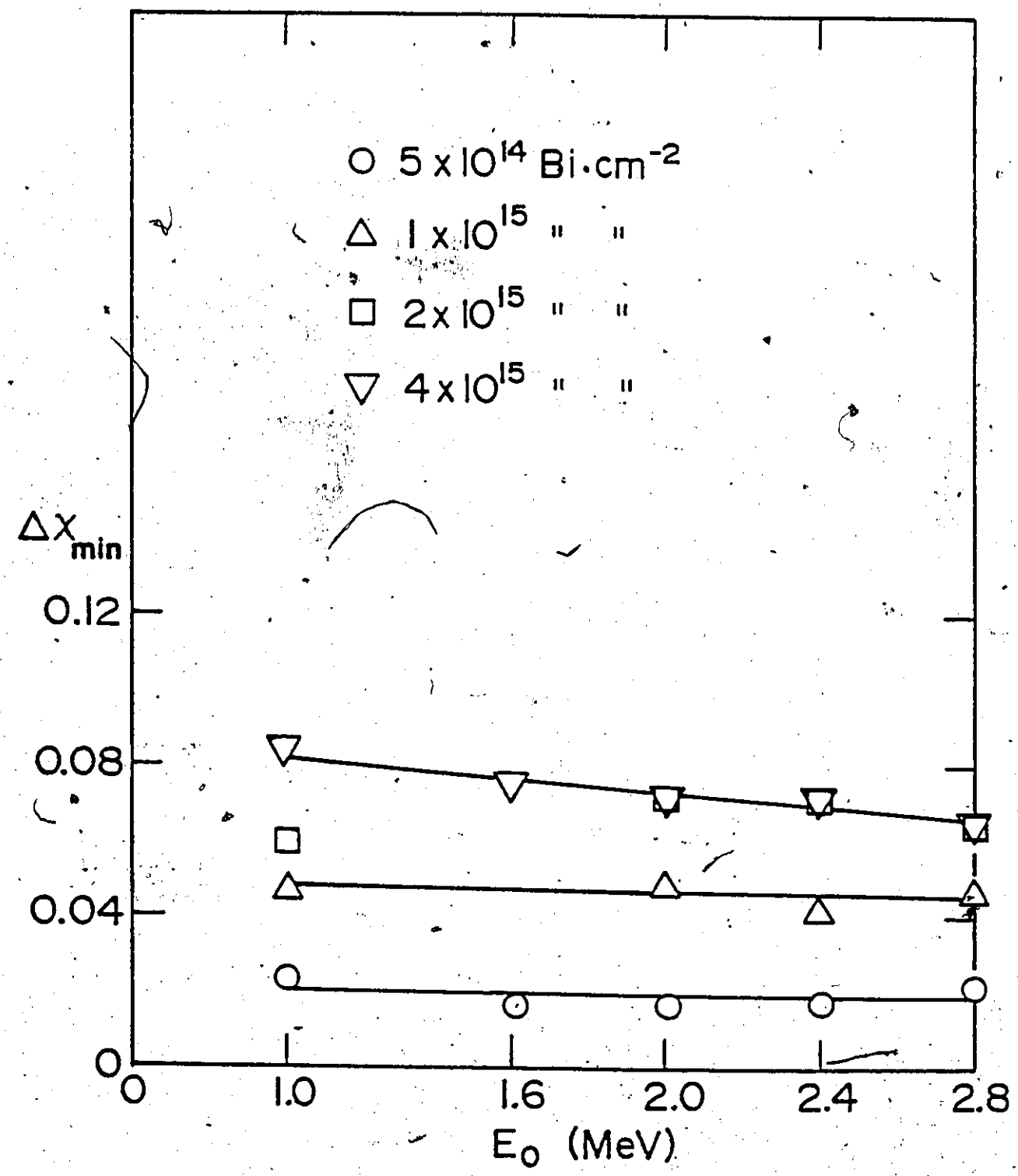

Fig. 6.33 Δx_{min} vs. E_o for a CdS crystal implanted with 0.5 - 4x10^{15} Bi.cm^{-2} at 50 K and analysed along the a-axis.

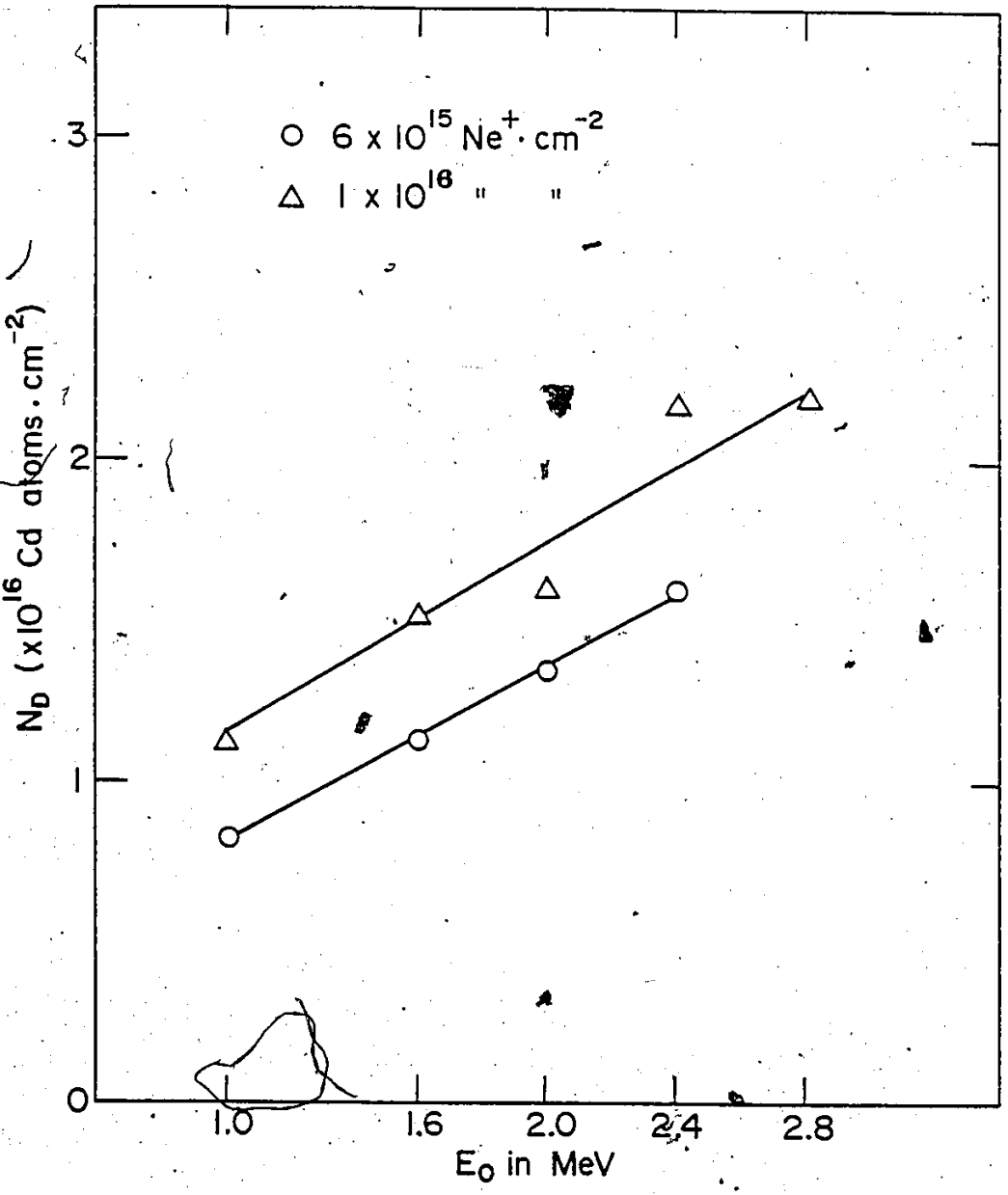

Fig. 6.34 N_D vs. E_o for a CdS crystal implanted with 6×10^{15} and 1×10^{16} $Ne.cm^{-2}$ at 50 K and analysed along the a-axis.

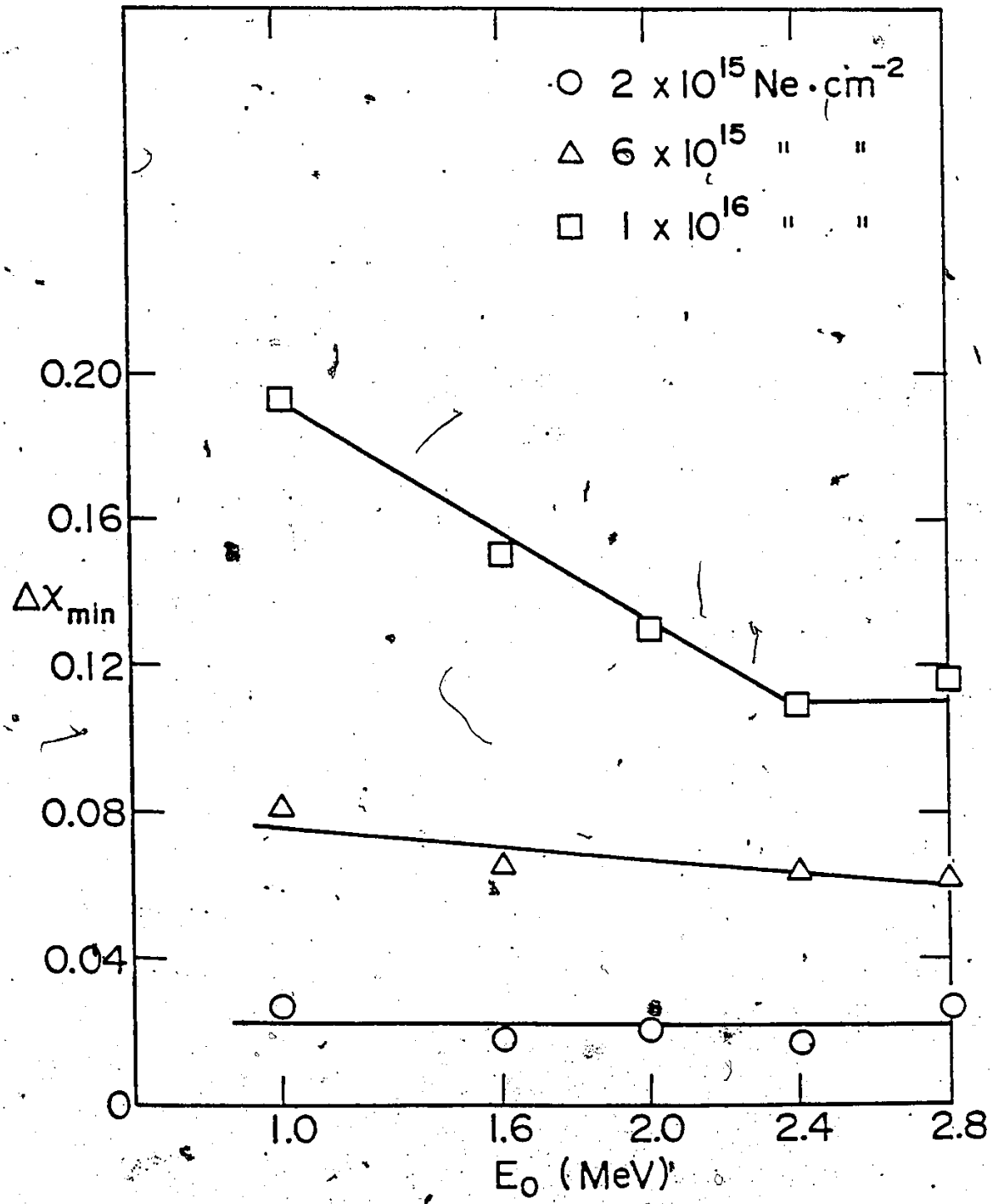

Fig. 6.35 Δx_{min} vs. E_o for a CdS crystal implanted with $2x10^{15}$ - $1x10^{16}$ $Ne.cm^{-2}$ at 50 K and analysed along the a-axis.

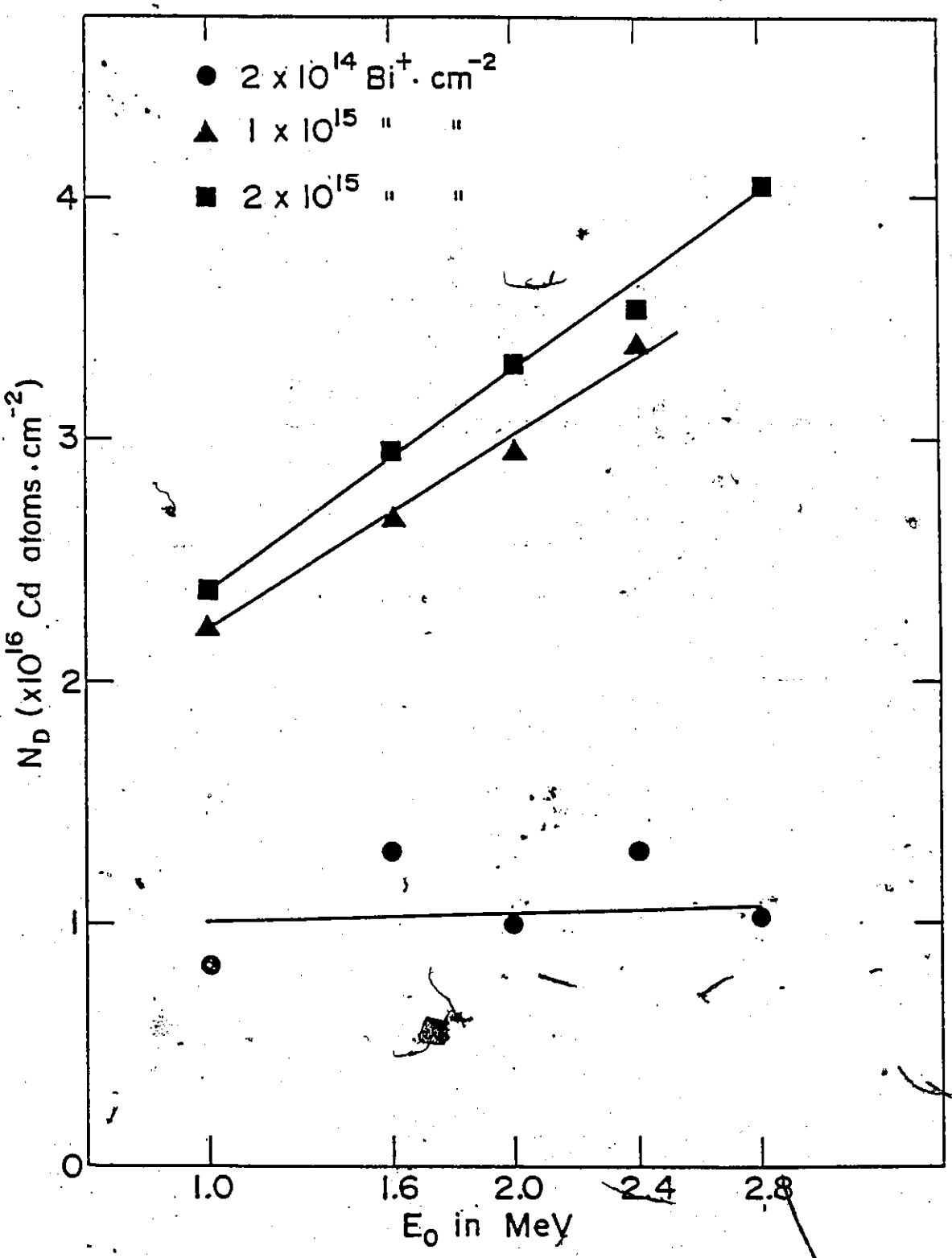

Fig. 6.36. N_D vs. E_0 for a CdS crystal implanted with 0.[illegible] - 2×10^{15} Bi cm^{-2} at 300 K and analysed along the a-axis.

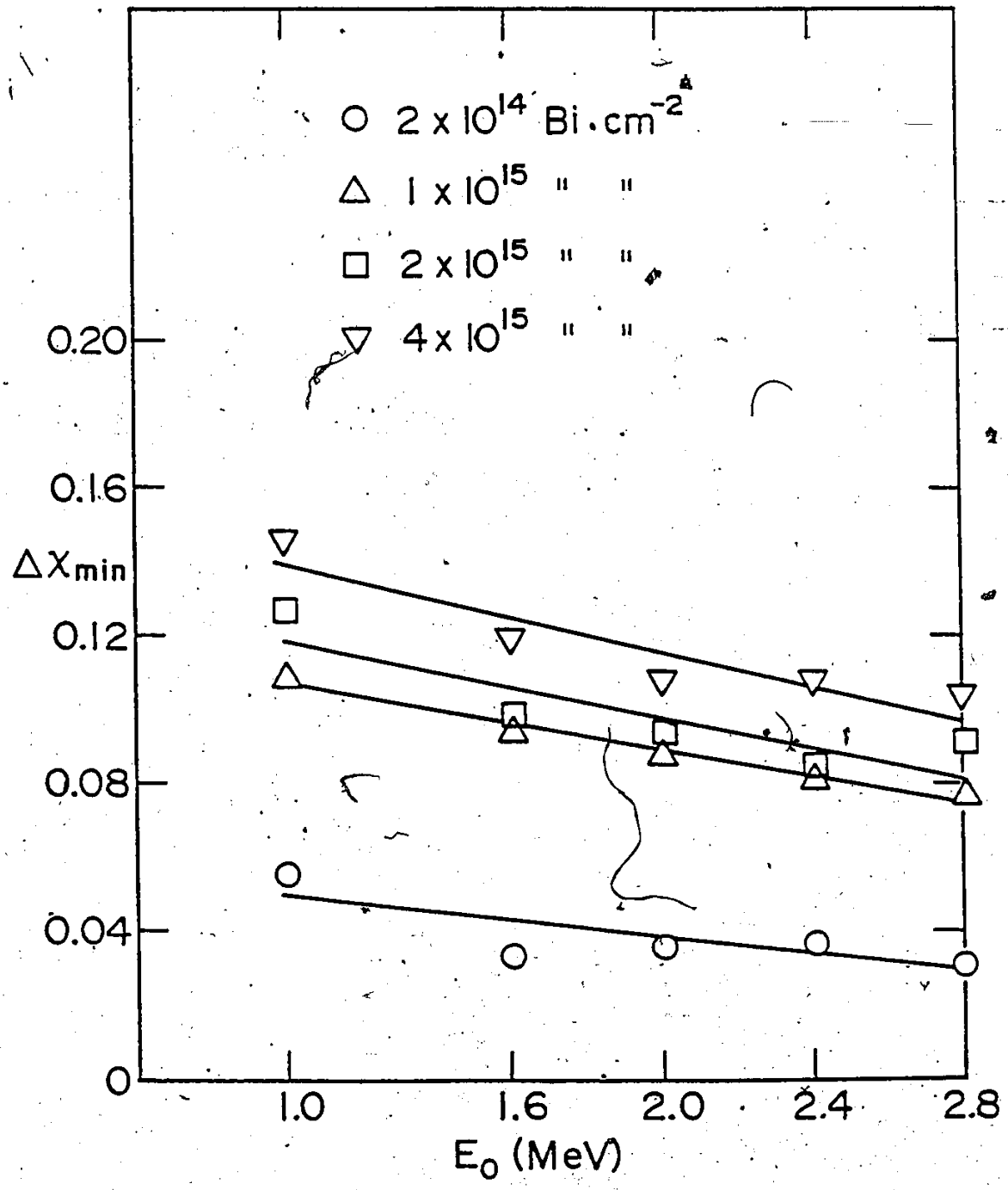

Fig. 6.37 Δx_{min} vs. E_o for a CdS crystal implanted with 0.2 - 4x10^{15} Bi.cm^{-2} at 300 K and analysed along the a-axis.

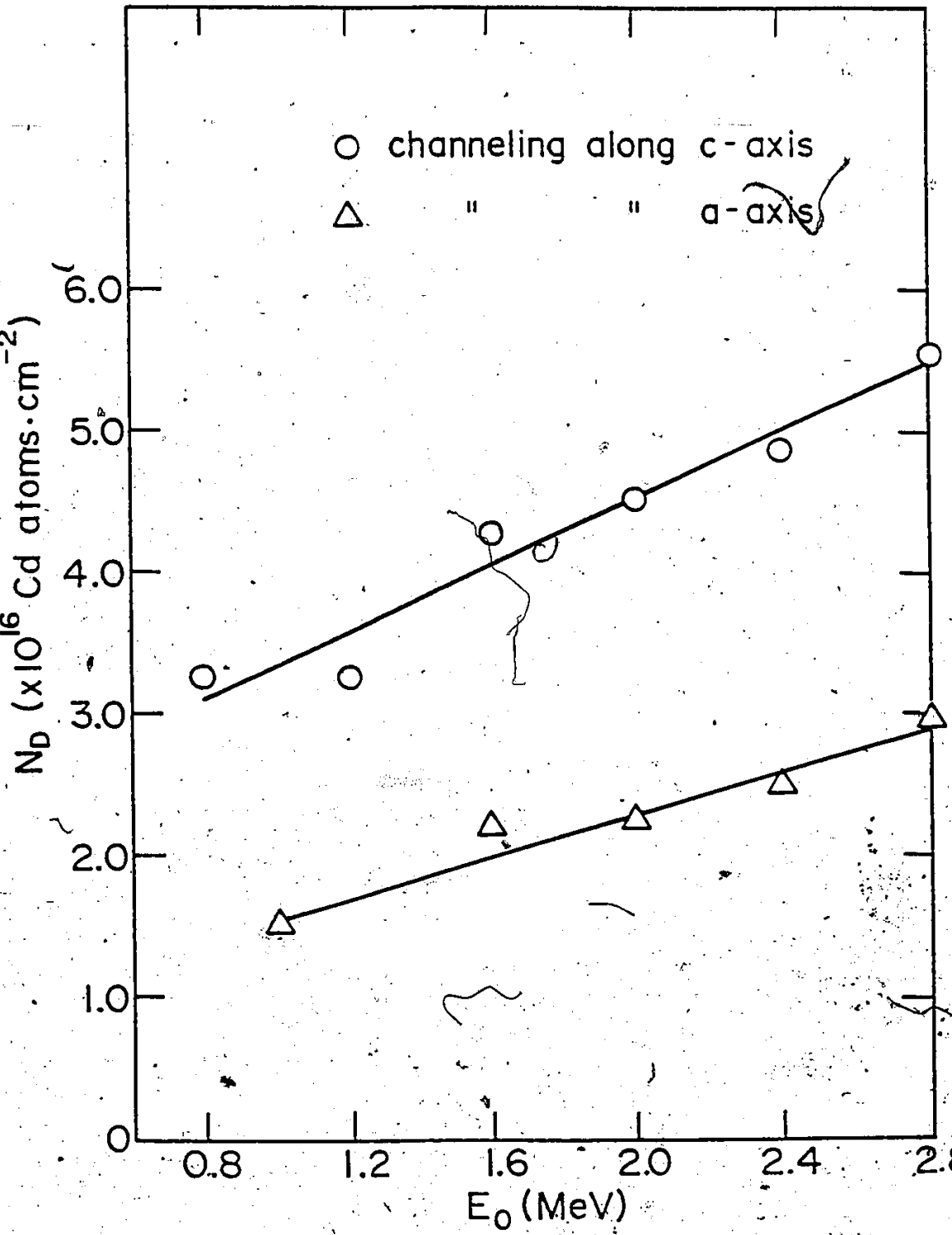

Fig. 6.38 N_D vs. E_0 for a CdS crystal implanted with 2×10^{15} Bi.cm^{-2} at 50 K and analysed along the c and a-axes.

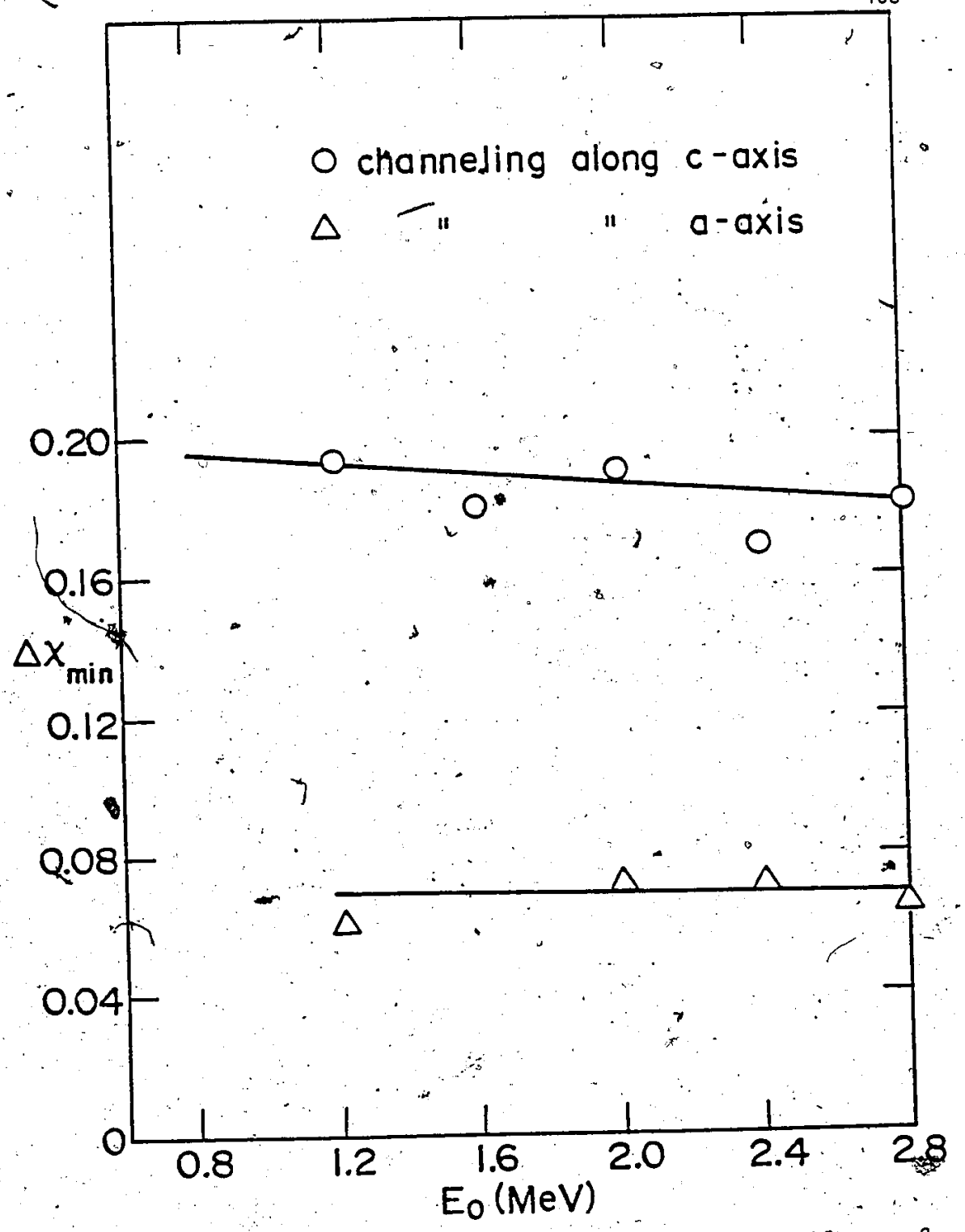

Fig. 6.39 Δx_{min} vs. E_0 for a CdS crystal implanted with 2×10^{15} Bi.cm^{-2} at 50 K and analysed along the c and a-axes.

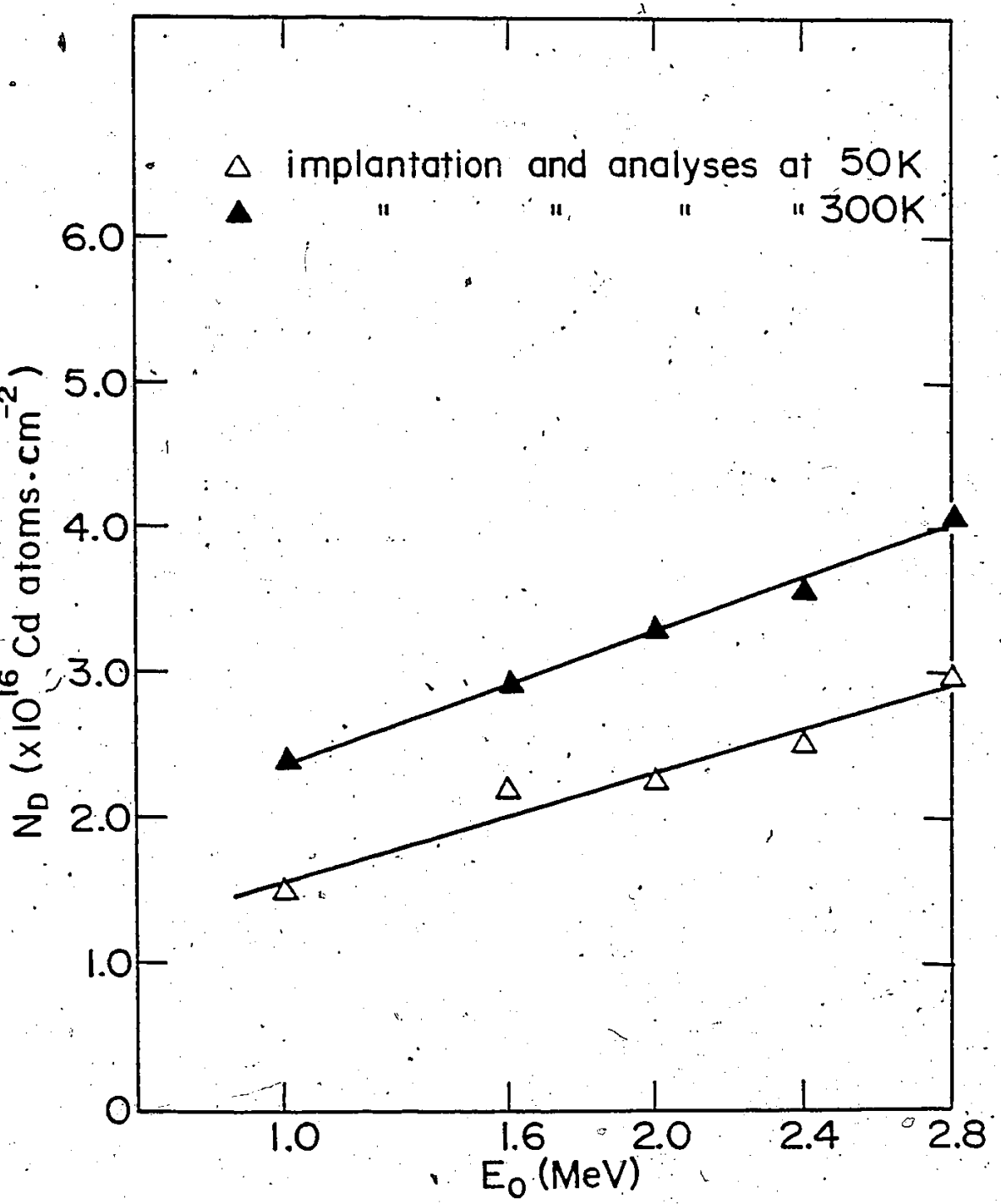

Fig. 6.40 N_D vs. E_0 for a CdS crystal implanted with 2×10^{15} Bi·cm^{-2} at 50 K and 300 K.

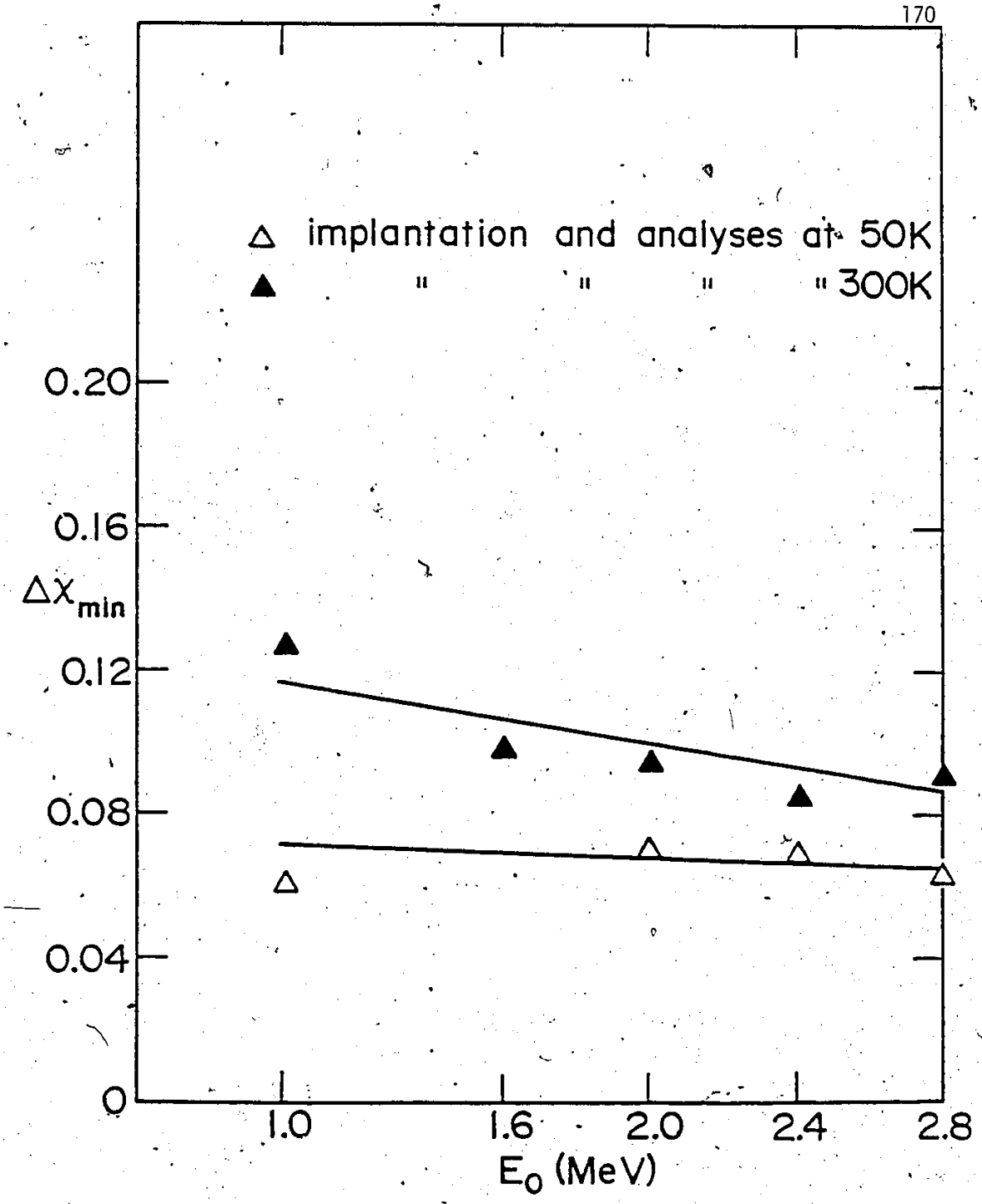

Fig. 6.41 $\Delta\chi_{min}$ vs. E_o for a CdS crystal implanted with 2×10^{15} Bi.cm^{-2} at 50 K and 300 K.

In summary, Bi^+ and Ne^+ implanted crystals analysed either along the a- or the c-axis showed that N_D increases with analyzing beam energy, while Δx_{min} is either constant or decreases with increasing E_o.

Similar studies have been carried out by Turos et al. [1978] for Ne^+ implanted silicon crystals. The authors reported that after annealing the implanted crystals at 650 - 800°C, N_D increased with increasing E_o, while x_{min} was energy independent. TEM studies of the annealed ion implanted silicon crystals revealed the formation of dislocation loops [Truche et al. (1974)].

For a particular divergence angle (δ), the transverse energy ($E_T = E_o \sin^2\delta$) of the channeled ions will increase with increasing E_o. Ions with an increased transverse energy can approach closer to the rows of the atoms, thereby accessing a larger area of the channel, as can be seen in the equipotential contour plots of Figs. 6.11 (a) and (b).

If the scattering centers are randomly distributed, then increasing the accessible area of the channel, i.e. increasing the energy of the analysing beam will not result in a change in the observed N_D. But if the scattering centers are preferentially located near the rows of atoms, N_D will increase with increasing E_o as was observed. The preferential location of the scattering centers near the rows of atoms is consistent with the existence of dislocation loops. When a dislocation loop is formed in a crystal the atoms around the core of the loop either relax inward (for vacancy type loops) or are pushed outward

(for interstitial type loops). The extent to which an atom is displaced from its normal lattice position depends upon the strain field at that position. If the displacement is large enough, as in the case for atoms positioned near the core of a dislocation, then the atom may be detected by backscattering. For atoms away from the core of a dislocation the displacement is small, hence only those channeled ions with a large transverse energy can interact strongly with these atoms. A stronger interaction results as the transverse energy increases. This would explain the increase in N_D with E_o.

The Δx_{min} values reported above are a summation of the contributions from dechanneling due to point defects and extended defects. As explained earlier (Sec. 4.2.3) dechanneling due to extended defects $\chi_R^L(b)$, can be separated approximately from the total dechanneling yield (Δx_{min}), by subtracting the calculated values of $\chi_R^P(b)$. Fig. 6.42 shows a plot of $\chi_R^L(b)$ vs. E_o for 60 keV Bi^+ implanted and analysed at 50 K which indicates the χ_R^P is independent of the analysing beam energy. Since the values of χ_R^P are only a small fraction of the Δx_{min} values (approximately 10%), the nature of the energy dependence of Δx_{min} can be essentially represented by $\chi_R^L(b)$ vs. E_o. The result that Δx_{min} is almost energy independent is in agreement with the calculated energy dependence for dislocation loops in the energy range studied (Sec. 4.2.3.).

Thus N_D and Δx_{min} measurements indicate the formation of dislocation loops by Ne^+ and Bi^+ implantation in CdS crystals, which is

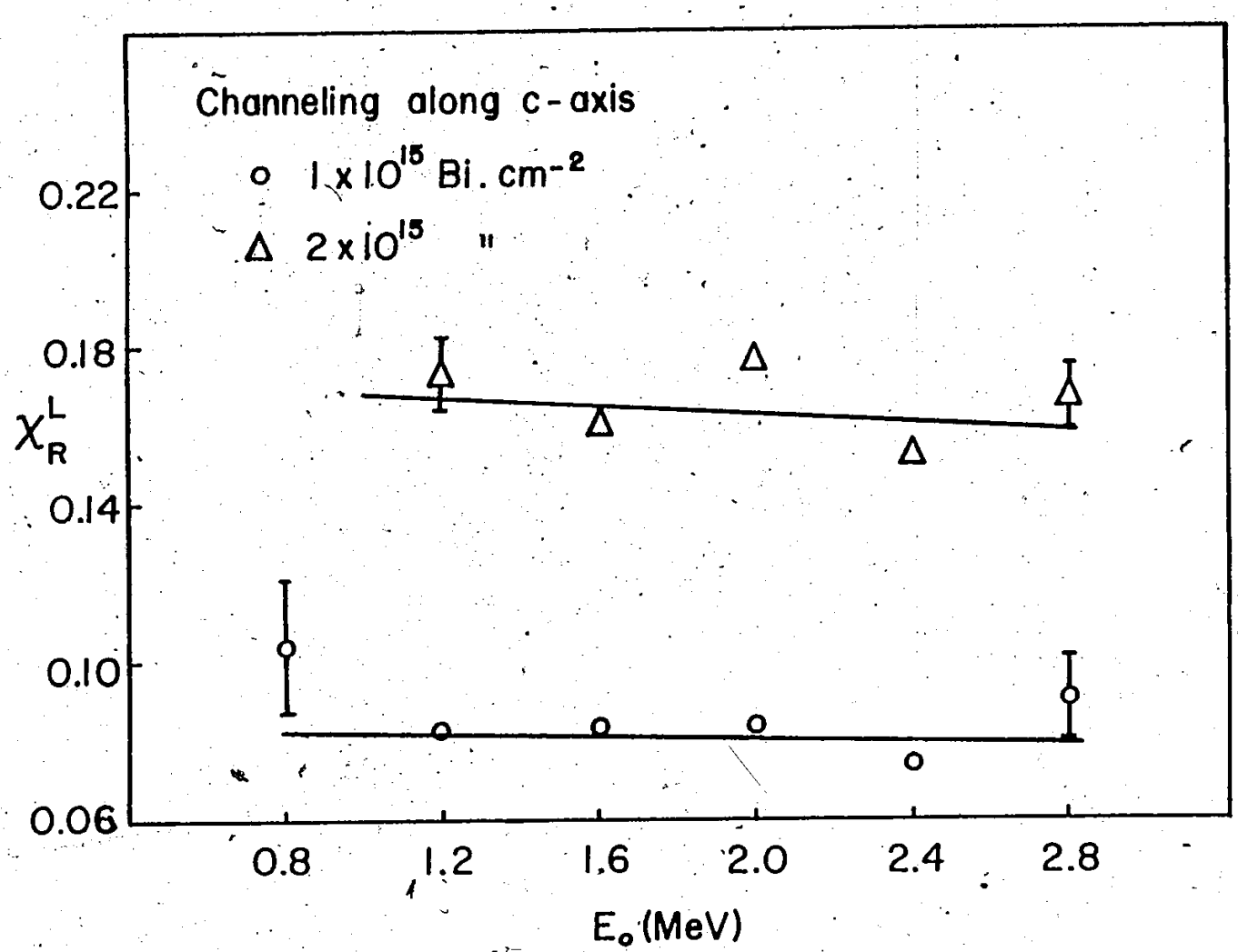

Fig. 6.42 $\chi_R^L(b)$ vs. E_o for a CdS crystal implanted with 1 and 2×10^{15} $Bi.cm^{-2}$ at 50K.

consistent with the TEM results (Sec. 6.1.1).

For samples analysed at 300 K, N_D and Δx_{min} were observed to be higher than when analysed at 50 K (Figs. 6.26 and 6.27). This behaviour at the higher temperature is attributed to the additional increase in the thermal vibrational amplitude of the atoms displaced slightly from their lattice sites and the consequent increased backscattering probability for the channeled beam.

6.2.5. Off Axis Results

In this section the method of obtaining information on the radial distribution of the displaced atoms is elaborated. In Sec. 4.2.3. it was mentioned that the radial distribution of the displaced atoms can be obtained by measuring $N_D(t)$ for different values of the channel accessed by the beam, provided the flux distribution across the channel is uniform.

By changing the tilt angle ψ, and/or E_o, the total transverse energy of the channeled ions can be changed (equation 4.28). In the present study E_o was varied from 1.0 MeV to 2.8 MeV while ψ was varied from 0.25 ψ_c to 0.65 ψ_c. The total number of scattering centres (N_D) was calculated for each angle, as explained previously (Sec.4.2.2.). The radial distribution of the atoms G(r,t), can now be determined from this N_D value, using the method explained by Foti et al. [1976] and Thompson et al. [1976]. This method assumes cylindrical symmetry for

the equipotential contours across the channel and calculates the increase in N_D with increasing accessed area of the channel for each tilt angle. In the present calculation actual areas of the channel for different tilt angles were measured from the equipotential plots of Figs. 4.11 (a) and (b).

The values of r along the direction from the atomic rows towards the channel center are determined from the equipotential plots using the total transverse energy imparted to the channeled ions for different tilt angles and He beam energies. The average radial distribution of scattering centers over a given radial interval can be written as

$$G\left(\frac{(r_i+r_{i-1})}{2}, t\right) = \frac{N_D(t,\psi)}{N}$$

For discrete values of ψ, this can be modified to give

$$G\left(\frac{r_0+r_1}{2}, t\right) = \frac{N_D(t,0)}{N}$$

$$G\left(\frac{r_1+r_2}{2}, t\right) = \frac{\frac{N_D(t,\psi_1)}{N}(A_T^2-A_{\psi_1}^2) - \frac{N_D(t,0)}{N}(A_T^2-A_0^2)}{A_0^2-A_{\psi_1}^2}$$

$$G\left(\frac{r_2+r_3}{2}, t\right) = \frac{\frac{N_D(t,\psi_2)}{N}(A_T^2-A_{\psi_2}^2) - \frac{N_D(t,\psi_1)}{N}(A_T^2-A_{\psi_1}^2)}{A_{\psi_1}^2-A_{\psi_2}^2}$$

-------- and so on

where A_T^2 is the total area of the channel and A_0^2, A_ψ^2 is the area under the equipotential contours for different tilt angles, determined from the transverse energy E_T.

Figs. 4.43 and 4.44 show plots of G(r,t) vs. (r/r_0) for 60 keV Bi^+ implanted into CdS and analysed at 50 K and 300 K respectively for c-axis channeling. The Thomas-Fermi screening radius, a = 0.1313 A (average of Cd and S), is also shown in the figures. Since G(r,t) is N_D/N (fraction of total atoms), its value should not exceed unity. However the figures show that near the rows of atoms G(r,t) exceeds unity, which is an indication of the limitation of this technique.

Both the figures show an increase in G(r,t) as ψ increases i.e. as the beam approaches closer to the rows of atoms. This is consistent with the presence of lattice strain near the core of dislocation loops. The results for the 300 K implants indicate a higher G(r,t) than at 50 K for all values of r/r_0. However, the technique is not accurate enough to definitively demonstrate the larger magnitude of the lattice vibrational amplitudes.

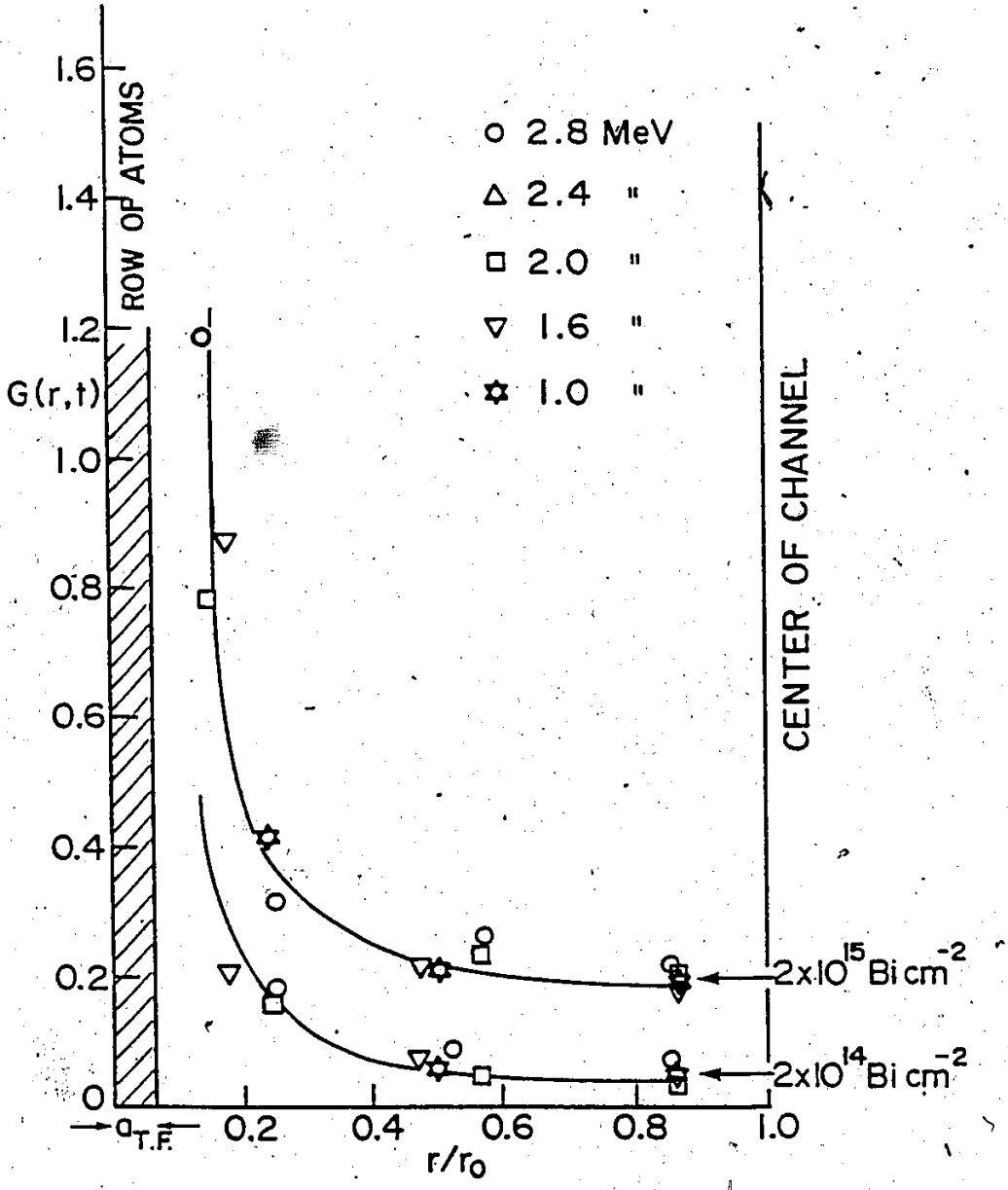

Fig. 6.43 G(r, t) vs. r/r_o for a CdS crystal implanted and analysed at 50 K.

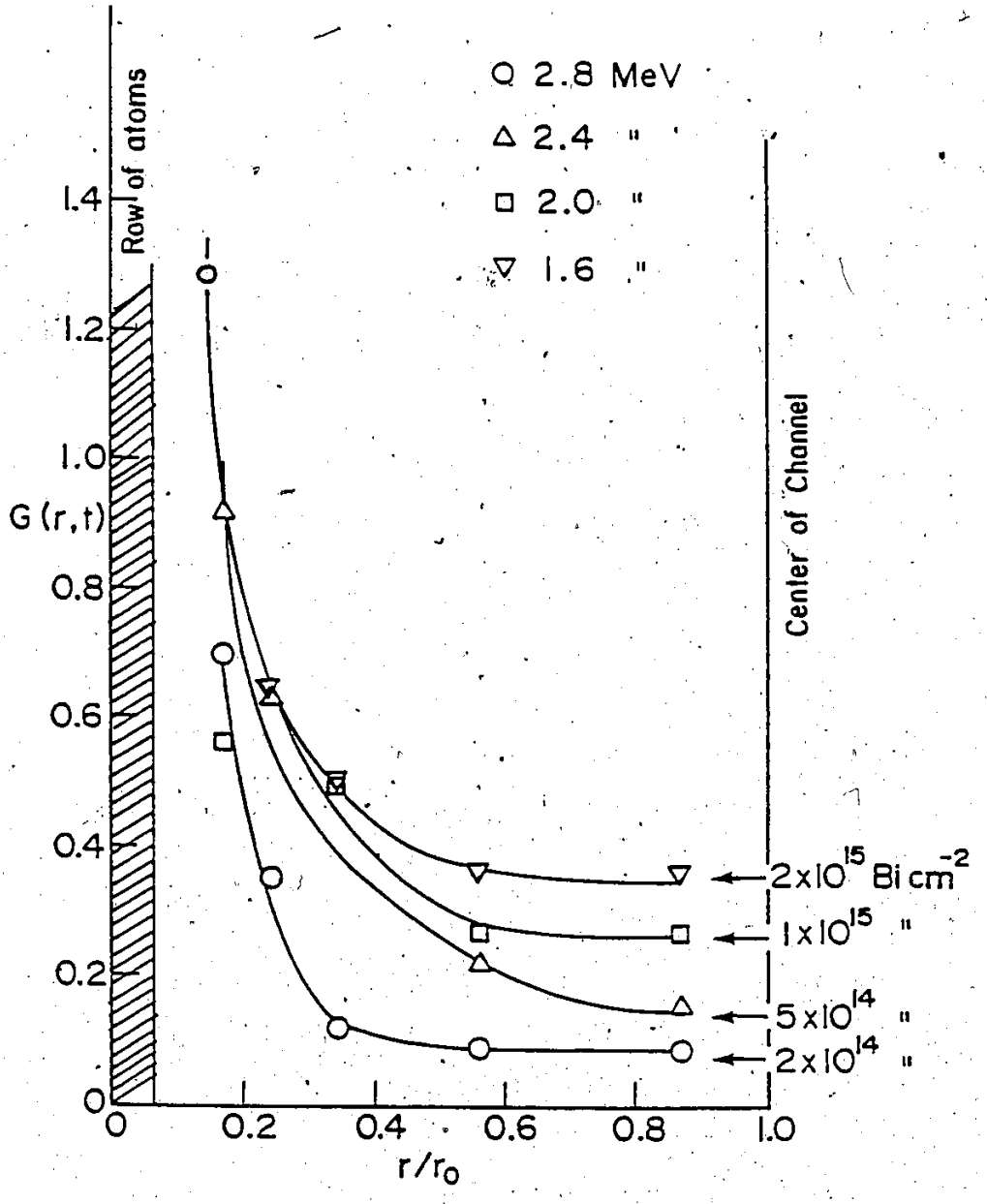

Fig. 6.44 G(r, t) vs. r/r_o for a CdS crystal implanted and analysed at 300 K.

6.3. Correlation Between RBS/channeling and TEM Results.

The RBS/channeling results of implanted samples showed that the saturated disorder peak height does not reach the non-aligned level, implying that the crystal structure is not amorphizing. This was confirmed by the electron diffraction measurements which always gave a single crystal pattern.

The energy dependence of N_D and Δx_{min} for Bi^+ and Ne^+ implanted samples is explained by the presence of dislocation loops. The rapid increase in the measured N_D values when the channeled beam was directed toward the rows of atoms by slightly tilting the crystal away from the channeling direction ('Off-Axis' measurements) indicated that there is a large strain in the lattice rows. Such a large strain in the lattice rows can be explained if extended defects are produced. These results are in agreement with the TEM observations which showed that implantation produces dislocation loops in CdS crystals.

TEM observations showed that heavy ion implantation produces two types of dislocation loops in CdS crystals: type I loops are smaller in size and in number density, and have a Burgers vector parallel to the c-axis; the larger and more numerous type II loops have a Burgers vector perpendicular to the c-axis. Hence, the dominant lattice distortion produced is perpendicular to the c-axis and parallel to the a-axis. The observed dechanneling is greater for c-axis channeling as expected. Results of the TEM and RBS/channeling tech-

niques for $1x10^{15}$ $Bi.cm^{-2}$ implanted samples are compared. The TEM sample showed that loops of type II were ≈ 1.5 times larger in size and ≈ 2.4 times greater in number density than type I loops. The RBS/channeling measurements showed that Δx_{min} along the c-axis, is ≈ 1.6 times greater than that measured along the a-axis.

The dechanneling probability vs. depth for dislocation loops observed in ion implanted CdS crystals cannot be calculated accurately by the method used by Picraux et al. [1978] (Sec. 4.2.3). This is because in the present case direct backscattering from the defects is also significant and hence the dechanneling contribution due to dislocation loops cannot be extracted from the total dechanneling.

The annealing of the damage produced in CdS has not been studied in detail in this work. However, different results were obtained for the two analysis techniques (RBS and TEM) for a sample implanted with $2x10^{15}$ $Bi.cm^{-2}$ at 50 K and annealed at 300 K for 20 hr. The TEM results showed a large amount (approximately 90 %) of annealing of dislocation loops while channeling analysis for another sample subjected to similar treatment did not show any measureable annealing. It should be noted that Yoshiie et al. (1981) observed annealing of interstitial loops at ≈ 600 K; they attributed to the absorption of vacancies. Hence a further investigation is necessary to confirm our observed TEM results. This discrepancy in the results may be due to the difference in the sample thickness for these two analysis techniques.

The TEM samples were < 80 nm thick which is comparable to the thickness of the implant damage region (≈ 60 nm), while the RBS samples were 2 mm thick, which is 10^4 times thicker than the thickness of the implanted region. Hence if there is any annealing of defects near the surface the TEM samples provide two free surfaces for annealing while RBS samples provide only one.

CHAPTER 7

CONCLUSIONS

The following conclusions are drawn from the results of present investigation.

(i) Heavy ion implantation (Bi^+, Ar^+, and Ne^+) produces dislocation loops with a Burgers vector $\vec{b}$ = 1/2 <0001> =<c> (type I) and $\vec{b}$ = 1/3 <11$\bar{2}$0> = <a> (type II) in CdS crystals.

(ii) The size of the type II loops is nearly twice that of type I loops while the number density is two to three times greater.

(iii) The loop size and number density increased with increasing nuclear energy deposited by the implanted ions while the loop size increased but the number density decreased with increasing implant dose.

(iv) The large type II loops were determined to be predominantly of vacancy character.

(v) The RBS/channeling results for 60 keV Bi^+, Kr^+ and Ar^+ implanted at 50 K and analysed at the same temperature showed that the damage peak increases with increasing implant dose and eventually

saturates at an implant dose dependent on the ion species.

(vi) The saturated damage peak height did not reach the non-aligned level indicating that the implanted layer is not amorphizing.

(vii) The measured N_D values were found to be two orders of magnitude lower than that theoretically calculated. This difference in N_D values is consistent with the TEM observation of the formation of dislocation loops. The theoretical calculation assumes no channeling.

(viii) The amount of dechannneling measured is an order of magnitude higher than that calculated, assuming the measured values of N_D correspond to randomly displaced atoms. The large dechanneling contribution for channeled ions is consistent with the correlated scattering from the atom relaxations due to the lattice strain that accompanies the dislocation loops.

(ix) The implantion damage when analysed for c-axis channeling showed a higher N_D than that analysed for a-axis channeling. This directional dependence of N_D values are attributed to the larger strain in lattice rows produced by dislocation loops.

(x) The Δx_{min} values were also higher for the c-axis analyses of the implanted samples than those obtained for the damage analysed along the a-axis. This is explained by the larger numbers of the crystal planes parallel to the c-axis (produced by dislocation loops of type II)

than that for the planes perpendicular to the c-axis (produced by dislocation loops of type I).

(ix) For both a and c- axis channeling the measured N_D and Δx_{min} values were large for samples implanted and analysed at lower temperature (50 K compared to 300 K). However, when samples implanted at 50 K were warmed to 300 K, the values obtained for N_D and Δx_{min} were similar to those obtained for samples implanted and analysed at 300 K. The results showed that the values of N_D and Δx_{min} obtained were solely a function of the analysis temperature and that no measurable annealing was observed. The larger damage measured at 300 K is attributed to an additional increase in the atomic vibrational amplitude compared to 50K.

(xii) Bismuth and neon implanted crystals showed a nearly linear increase in the N_D values with increasing analysing beam energy, while Δx_{min} was either independent of E_o or decreased with increasing E_o. These results for the energy dependence of N_D and Δx_{min} are attributed to the presence of dislocation loops formed by Bi^+ and Ne^+ implantation.

(xiii) The formation of dislocation loops by heavy ion implantation is further supported by results of the 'Off-Axis measurements' which showed a rapid increase in N_D as the crystals were slightly tilted away from the channeling direction.

REFERENCES

Abrikosov, N. Kh., Bankin, V.F., Poretskaya, L.V., Shetimoval, L.E. [1969]. Semiconducting II-Vi, IV-V, and V-VI compounds, Plenum Press, N.Y., 24.

Amelinckx, S. (1964). Disc. Faraday Soc. 38.

Anderson, W.W. and Mitchell, J.T. (1968). Appl. Phys. Letts. 12, 334.

Andersen, J.U., Andreasen, O., Davies, J.A. and Uggerhoj, E. (1971). Rad. Effects 7, 25.

Armitage S.A. (1970). Proc. European Conf. Ion Implantation, Reading, England, Pub. Peter Peregrinus, England, p.138.

Azaroff, L.Y. and Brophy, J.J. (1963). Electronic Processes in Materials, 352

Baxter D. (1977). Ph.D. Thesis, Dept. of Electrical Engineering, Univ. of Salford, England.

Blank, H., Delavignett, P. Gevers, R. and Amelinckx, S. (1964). Stat. Sol. 7, 747.

Blank, H., Delavignett, P. and Amelinkx (1962). Phys. Stat. Sol. 2, 1660.

Bøgh, E. (1968). Can. J. Phys. 46, 653.

Bohr, N. (1948). Kgl. Dan. Vid. Selsk. Mat. Fys. Medd. 18, no. 8.

Böttiger, T. and Eisèn, F.H. (1973). Thin Solid Films 19, 969.

Born, M. and Mayer, J.E. (1932). Physik 75, 96.

Bragg, W.H. and Kleeman, R. (1905) Phil. Mag. 10, S 318.

Brinkman, J.A. (1955). Amer. J. Phys. 24, 246.

Bryant, F.J. and Fewster, R.H., (1973). Rad. Effects, 20, 239.

Bryant, F.J. (1982). Rad. Effects. 65, 81.

Carpenter, G.J.C. (1974). Atomic Energy of Canada, Chalk River, Ont. Report No. AECL 5023.

Carpenter, G.J.C. (1981). J. Nucl. Mater., 96, 213.

Carter, G., Colligan, J.S. (1968). Ion Bombardment of Solids, Pub. Heineman, London, England.

Chadderton, L.T., Fitzgerald, A.G. and Yoffi, A.D., (1963). Nature, 198, 573.

Chernow, F., Ruse, G. and Wahlin, L. (1968). Appl. Phys. Letts, 12, 339.

Condon, B.J. (1976). Ph.D Thesis, Physics Department, Stanford, Cali. USA.

Chu, W.K., Mayer, J.W. and Nicolet, M.A. (1978). Backscattering Spectrometry, Academic press, New York.

Davies, J.A. (1978). Material Characterization using Ion Beams, Ed. by J.P. Thomas and A. Cachard, Plenum Publishing Corporation.

Davies, J.A., Howe, L.M., Marsden, D.A and Whitton, J.L. (1972). Rad. Effects. 12, 247.

Devlin, S.S., Jost, J.M., Shiozawa, L.R. (1960). U.S.Dept. Comm. Office Tech. Serv. P.B. Rept. 161, 938.

Edington, J.W. (1975). Practical Electron Microscopy in Materials Science, Philips Technical Library, 14.

Eisen, F.H. (1966). Phys. Lett., 23, 401.

Elsby, C.N. (1971). Ph.D. thesis, Air Force Institute of Technology, WPAFB, USA

Feldman, L.C., Mayer. J.W. and Picraux, S.T. (1982). Materials Analysis

By Ion Channeling; Submicron Crystallohraphy, Publ. by Academic Press, New york, U.S.A.

Feldman, L.C and Rogers, J.W. (1970). J Appl. Phys., 41, 3776.

Firsov, O.B., (1958). Phys. JETP 6 (33), 534.

Foti, G., Baeri, P., Rimini E. and Campisano S.U. (1976). J. Appl. Phys. 47, 12, 5206.

Foti, G., Grasso F., Quattrocchi, R. and Rimini E. (1970). Phys. Rev. B 3, 2169.

Foti, G., Picraux, S.T., Campisano, S.U., Rimini, E. and Kant, R.A. (1977). Implantation in Semiconductors, F. Chernow, J.A. Borders and D.K. Brice, Plenum. Press, New york, 247.

Gemmel, D.S. (1974). Rev. Modern Phys. 46, 129.

Gibbon, J.f., Moll, J.L. and Meyer, N.I. (1965). Nucl. Instru. and Meths., 38, 165.

Gibson, J.B., Goland, A.N., Milgram, M. and Vineyard, G.H. (1960). Phy. Rev. 120, 1229.

Govind, P.K. and Fraikor, F.J. (1971). J. Appl. Phys., 42, 2476.

Goldstein, H. (1958). Classical Mechanics, Addision-Wesley, Cambridge, Mass. England.

Gombas, P. (1956). Handbuch der Physik Ed. XXXVI.

Grigor'ev, A.N. and Dikii, N.P. (1974). Sov. Phys. Semicond. (U.S.A.) 9, 757.

Grigor'ev, A.N., Nikolajchuk, L.I. and Khizhnyak, N.A. (1985). Rad. Effects 84, 291.

Hirsch, P.B., Howie, A., Nicholson, R.B., Pashley, D.W. and Whelan, M.J. (1970). Electron Microcsopy of Thin Crystals, Butterworths.

Howie, A. and Goringe, M.J. (1971). Electron Microscopy in Materials Science Ed. by Valdre, U., Academic Press, New york, U.S.A., 462.

Hou, S.L. and Marley(Jnr.), J.A., (1970). Appl. Phys. Lett., 16, 467.

Howe, L.M., Swanson, M.L., Quenneville, A.F. (1976). Nucl. Instr. and Meth. 132, 241.

Hull, D. (1965). Introduction to Dislocations, Pergamon Press, New York.

Hussain, T. and Linker G. (1980). Rad Effects. 51, 103.

Hutchby, J.A. (1972). Rad. Effects, 16, 189.

Hutchby, J.A. and Miller, W.E. (1975). J. Appl. Phys. 46 (10), 4479.

Keil, F., Zietler, E. and Zinn, Z. (1960). Fur Naturfoysch 159, 1031.

Kelly, P.M. and Black, R.G. (1973). Phil. Mag. 28, 415.

Kinchin, G.H. and Pease, R.S. (1955). Rep. Prog. Phys. 18, (1), 143.

Kroger, F.A., (1965). J. Phys. Chem. Sol. 26, 1717.

Kudo, H. (1978). Phys. Rev. B, 18, 5995.

Kudo, H. (1976). J. Phys. Soc. Jap. 40, 1645.

Lindhard, J. (1954). Kgl. Dan. Vid. Selsk. Mat. Fys. Medd. 28, no. 8.

Lindhard, J. (1965). Kgl. Dan. Vid. Selsk. Mat. Fys. Medd. 34, no. 14.

Lindhard, J., Scharff, M. and Schiott, H.E. (1968). Kgl. Dan. Vid. Selsk. Mat. Fys. Medd. 36, no. 10.

Lindhard, J., Nielson, V., Scharff M. (1968). Kgl. Dan. Vid. Selsk. Mat. Fys. Medd. 36, no. 10.

Look, D.C. and Meese, J.M. (1974). Rad. Effects. 22, 229.

Lugujjo, E. and Mayer J.W. (1973). Phys. Rev. B7, 1782.

Loretto, M.H. and Smallman R.E. (1978). Defect Analysis in Electron Microscopy, Chapman and Hall Ltd., London.

Mandel, G. (1964). Phys. Rev. 134A, 1073.

Miller, W.E., Hutchby, J.A. and Webster, R.C., (1972). Proc. Third Int. Conf. on Ion Implantation in Semicond. and other Materials (Yorktown Heights, N.Y., (1973) Ed. B.L.Crowder. Pub. Plenum Press, N.Y. 373.

Moliere, G. (1947). Z. Naturforsch, 20, 133.

Morgan, D.V., (1973). Channeling-Theory, Observation and Application, J. Wiley and Sons, London, England.

Mory, J., and Quéré Y. (1972). Rad. Effects. 13, 57.

Mott, N.F. and Massey, H.S.W. (1965). Theory of Atomic Collision, Oxford University Press, England.

Neale, E.C., (1971). Ph.D. thesis, School of Engineering of the Air Force Institute of Technology, USA.

Neuberger, M., (1969). Electronic Properties Information Center, Hughes Aircraft Company, Culver City, Calif. 90230. Contract F 33615/68/c/1225. E PIC S II.

Norris, C.B., Barnes, C.E. and Beezhold, W.J. (1973). Appl. Phys. 44, 7, 3325

Olley, J.A., Williams, P.M. and Yoffe, A.D. (1970). Proc. European Conf. Ion Implantation, Pub. Peter Peregrinus, Reading, England. 148.

Pathak, A.P., (1982). Rad. Effects. 61, 1.

Parikh, N.R., Thompson, D.A., Burkova, R. and Raghunathan, V.S., (1984). Mat. Res. Soc. Symp. Proc. 27, 323.

Parikh, N.R. (1981). M.Eng. (on campus report) Dept. of Eng. Physics, McMaster University, Ont. Canada.

Picraux, S.T., Davies, J.A., Erikson, L., Johansson, N.G.E. and Mayer,

J.W. (1969). Phys. Rev. 180, 873.

Picraux, S.T., Rimini, E., Foti, G. and Campisano, S.U. (1978). Phys. Rev. B 18, 2078.

Picraux S.T., Follstaedt, D.M., Baeri, P., Campisano, S.U., Foti, G. and Rimini E. (1980). Rad. Effects 49, 75.

Picraux, S.T. (1982). Materials Analysis by Ion Channeling; Submicron Crystallography, Pub. Academic press, 101.

Pollard, E.R. and Hartke, J.L. (1969). Bull. Amer. Phys. Soc. 14, 115.

Pronko, P.P., Bottiger, J., Davies, J.A. and Mitchell, J.B., (1974). Rad. Effects 21, 25.

Quéré Y. (1968). Phys. Status. Solidi. 30 ,713

Quéré Y. (1974). Nucl. Instr. and Meth. 53 (1) 262.

Remeir, L. (1984). Transmission Electron Microscopy, Pub. Springer - Verlag, New York, USA.

Seitz, F. and Koehler, J.S. (1956). Sol. State Phys. 2, 307.

Shiraki, Y., Shimada, T. and Komatsubara, K.F. (1972). J. Appl. Phys. 43, 710.

Shiraki, Y., Shimada, T. and Komatsubara, K.F. (1973). Proc. Third Int. Conf. on Ion Implantation in Semicond. and other Materials, Yorktown Height, N.Y. Ed. Croder, B.L., Pub. Plenum Press, N.Y., 395.

Sigmund, P., (1969). Appl. Phys. Letts. 14, 114

Sigmund, P., (1974). Appl. Phys. Letts. 25, no. 3, 169.

Sigmund, P. and Winterbon, K.B. (1974). Nucl. Instr. and Meth. 119. 541.

Swanson, M.L., Quenneville, A.F. (1976). Nucl. Instrum. and Meth. 132, 241.

Swanson, M.L. (1982). Prog. Phys., 45, 47.

Tell, B., Gibson, W.M. and Rogers, J.W. (1970). Appl. Phys. Lett. 17, 315.

Thomson, M.W., Defects and Radiation Damage in Metals, Pub. by Syndics. of the Cambridge University Press, London, England.

Thompson, D.A. and Walker R.S. (1976 a). Rad. Effects 30, 37.

Thompson, D.A. and Walker, R.S. (1976 b). Nucl. Instum. and Meth. 132, 281.

Thompson, D.A. and Walker R.S. (1978). Rad. Effects 36, 91.

Thompson, D.A. (1981). Rad. Effects 56, 105.

Torrens, I.M. (1972). Interatomic Potentials, Academic press, New Yoyk.

Truche, R., Dupuy, M., Lafeuille, D. and Monfert, A. (1974). Rapport LeTI/ME 74-380 RT/CT, CENG Grenoble, France.

Tseng, M.F., Gyulai, J., Koji, T., Lau, S.S., Roth, T. and Mayer, J.W. (1978). Nucl. Instrum. and Meth. 149, 615.

Turos, A., Wielunski, L., and Weilunski, M. (1978). Nucl. Instrum. and Meth. 149, 421.

Vook, F.L. (1971). Phys. Rev. B3, 2022.

Walker, R.G. (1977). Thesis, Dept. of Electrical Engineering, McMaster University.

Walsh, D. (1977). Solid State Electr. 20, 813.

Westmoreland, J.E., Mayer, J.W., Eisen, F.H. and Welch, B.(1970). Rad. Effects 6, 161.

Winterbon, K.B., Sigmund, P., Sanders, J.B. (1970). Kgl. Dan. Vid. Selsk. Mat. Fys. Medd., 37, no.14.

Winterbon, K.B. (1975). Ion Implantation Range and Energy Deposition

Distributions, vol.2, Plenum press, London, England.

Williams, J.S. (1975). Nucl. Instrum. and Meth. 126, 205.

Williams, J.S. (1978). Nucl. Instrum. and Meth. 149, 207.

Wilkens, M. and Ruhle M. (1972). Phys. Stat. Sol. 49, 749.

Williams, P.M. and Yoffe, A.D. (1971). Rad. Effects 9, 139.

Woo, O.T., Carpenter G.J.C. and Cann. C.D. (1982). J. Nucl. Mater., 105, 326.

Yoshiie, T., Iwanga, H., Shibata, N., Suzuki, K. and Takeuchi S. (1980). Phil. Mag. A 41, 935.

Yoshiie, T., Iwanga, H., Shibata, N., Ichihara, M., Suzuki, K., and Takeuchi, S. (1981). Defects and Radiation Effects in Semiconductors, (1980). Ed. by Hasiguti, R.R. Inst. Phys. Conf. Ser.No. 59, 443.

Yoshiie, T., Iwanga, H., Shibata, N., Suzuki, K., Ichihara, M. and Takeuchi S. (1983). Phil. Mag. A 47, 315.

Ziegler, J.F. and Chu. W.K. (1974). Atomic and Nucl. Data Tables 13, 463.